

**MANUFACTURING AND HEAT TRANSFER ANALYSIS OF
NANO-MICRO FIBER COMPOSITES**

Except where reference is made to the work of others, the work described in this dissertation is my own or was done in collaboration with my advisory committee. This dissertation does not include proprietary or classified information.

Birgül Aşcıoğlu

Certificate of Approval:

Peter Schwartz
Professor
Textile Engineering

Sabit Adanur, Chair
Professor
Textile Engineering

Lewis Slafen
Associate Professor
Consumer Affairs

Roy W. Knight
Assistant Professor
Mechanical Engineering

Stephen L. McFarland
Acting Dean
Graduate School

MANUFACTURING AND HEAT TRANSFER ANALYSIS OF
NANO-MICRO FIBER COMPOSITES

Birgöl Aşcıođlu

A Dissertation

Submitted to

the Graduate Faculty of

Auburn University

in Partial Fulfillment of the

Requirements for the Degree of

Doctor of Philosophy

Auburn, Alabama

August 8, 2005

**MANUFACTURING AND HEAT TRANSFER ANALYSIS OF
NANO-MICRO FIBER COMPOSITES**

Birgül Aşcıoğlu

Permission is granted to Auburn University to make copies of this dissertation at its discretion, upon request of individuals or institutions and at their expense. The author reserves all the publication rights.

Signature of Author

Date

06/22/2005

VITA

Birgöl Aşciođlu, daughter of Sevginar Aşciođlu (Aksoy) and Fikret Aşciođlu was born in Trabzon, Turkey on September 16, 1978. She graduated from Trabzon Anatolia Trade High School in May 1995 and received a Bachelor of Science degree in Mechanical Engineering from Karadeniz Technical University in June 1999.

She received a Master of Science degree in Mechanical Engineering from Karadeniz Technical University in August 2002. She joined the Ph.D. program in Textile and Apparel Science in the Department of Textile Engineering, Auburn University in August 2002.

DISSERTATION ABSTRACT

MANUFACTURING AND HEAT TRANSFER ANALYSIS OF
NANO-MICRO FIBER COMPOSITES

Birgöl Aşcıođlu

Doctor of Philosophy, August 8, 2005

(M.Sc., Karadeniz Technical University, Turkey, 2002)

(B.Sc., Karadeniz Technical University, Turkey, 1999)

171 Typed Pages

Directed by Dr. Sabit Adanur

Nano-micro composites are widely used in many areas, such as sensors, flame retardant materials, batteries, and filtration. In this work, thermal properties of the filler fiber composites are studied experimentally, analytically, and numerically. For the thermal studies, the transverse thermal conductivity is discussed and calculated both analytically and numerically. In the analytical study, a hexagonal cell model is developed

which includes an interfacial area. The volume fraction of the filler fibers is kept between 10-30%. From the results, it is seen that the numerical and analytical results showed much similarity.

A novel device is designed to manufacture yarns continuously. Nano-micro fibers are manufactured and collected to form web and yarn. To collect the fibers, nonwoven fabrics are used, which allow easy release of fibers from the surface. Scanning electron microscope, thermal gravimetric analysis, and digital imaging are used to analyze the structures. Tensile strength, surface tension, and air permeability measurements are done.

To transition from micro to nano is discussed in terms of modeling. It was shown that for the electrospun fibers whose diameters are above 200 nm, the conventional heat transfer modeling methods are still valid.

Style manual or journal used

Textile Research Journal

Computer software used

Microsoft Word, Excel, MATLAB, ANSYS 7.0, AUTO-CAD, TTS Data
Analysis

ACKNOWLEDGEMENTS

In this study, I had a chance to be between nano and micro areas and this was the help of my adviser Dr. Sabit Adanur. He guided me, advised me, helped me to see my potential. I am grateful to him for giving me the encouragement to take the steps inside the research.

I would like to give my appreciation and sincere thanks to Dr. P. Schwartz, Dr. L. Slaten and Dr. R. Knight for serving on my committee and for their kind help.

I would like to thank also Dr. M. Miller, Dr. R. Broughton, Dr. Y. Gowayed, Dr. H. Aglan, Dr. H. Bas, Dr. L. Gumusel, Dr. R. Farag, and Dr. M. Traore for their suggestions and sincere help.

I want to thank all the members of the Textile Engineering Department for their help and National Textile Center for financial support of this research.

My closest friends in Auburn...I could not have imagined living here without you. You are the family to me.

And the reason for most of my tears, happiness, sadness... my dear family... I can not tell you how much you made me to think how lucky I am to have you. My mother; Sevginar, my father; Fikret, my sister; Elif Burcu, my brother; Arman, my closest friends Sabire, Esenc and Yucel...so much applause for you.

TABLE OF CONTENTS

LIST OF TABLES.....	xi
LIST OF FIGURES.....	xii
CHAPTER 1	1
INTRODUCTION	1
1.1. References.....	3
CHAPTER 2	4
LITERATURE REVIEW	4
2.1. Nano-micro (NM) Composites	4
2.2. Interface Effect.....	6
2.3. Electrospinning	12
2.4. Thermal Properties of Nano-Micro Composites.....	12
2.4.1. Thermal Conductivity in Macro Level	13
2.4.2. Thermal Conductivity in Nano Level	15
2.4.3. Flame Resistance	18
2.5. Modeling.....	21
2.6. References.....	24
CHAPTER 3	32
NANO-MICRO FIBER BASED FILM, WEB AND YARN MANUFACTURING	32
3.1. Materials	32
3.1.1. Polyvinyl Alcohol (PVA) Properties	32
3.1.2. Laponite® Properties	35
3.2. Continuous Nano-Micro Fiber Based Yarn Manufacturing	36

3.2.1. Defining the Maximum Collected Nanofiber Web Area.....	39
3.2.2. The Voltage Effect in Electrospinning	41
3.2.3. Scanning Electron Microscope (SEM) Imaging.....	50
3.2.4. Continuous Manufacturing Device.....	51
3.2.5. Coating.....	54
3.2.6. Twisting of Manufactured Nano-micro Fibers.....	55
3.2.7. Differential Scanning Calorimetry (DSC) Studies	56
3.2.8. Air Permeability Measurements	57
3.2.9. Dynamic Contact Analyzer.....	57
3.2.10. Thermal Conductivity Measurement	58
3.3. References.....	61
CHAPTER 4	63
ANALYTICAL MODELING OF FILLER FIBER REINFORCED COMPOSITES	63
4.1. Description of the Problem	65
4.2. Modeling for Analytical Thermal Resistance.....	67
4.2.1. Thermal Resistance of the First Region, R_{1a}	68
4.2.2. Thermal Resistance of the Second Region, R_2	69
4.2.3. Thermal Resistance of the Third Region, R_3	69
4.2.4. Thermal Resistance of the Forth Region, R_4	74
4.3. Dimensionless Total Thermal Resistance of the Model, R_t	77
4.4. Calculation of the Volume Fractions of the Model	79
4.5. Dimensionless Total Thermal Resistance of the Model without a Barrier.....	81
4.6. Computer Implementation of the Analytical Model.....	85
4.7. References.....	88
CHAPTER 5	89
HEAT TRANSFER ANALYSIS OF NANO-MICRO FIBER COMPOSITES BY FINITE ELEMENT METHOD	89
5.1. Introduction.....	89
5.2. A simple FEM Model	90

5.3. Modeling with ANSYS.....	94
5.4. Modeling Configurations.....	100
5.4.1. The Effect of Material Properties of the Filler Fiber.....	100
5.4.2. Polymer’s Heat Deflection Temperature (HDT).....	103
5.4.3. Defining the Unit Cells.....	105
5. 5. References.....	109
 CHAPTER 6	 110
RESULTS AND DISCUSSION.....	110
6.1. MATLAB Results.....	112
6.2. ANSYS Results.....	117
6.3. SEM Results	137
6.4. Tensile Testing.....	146
6.5. Air Permeability.....	148
6.6. Surface Tension	149
6.7. Differential Scanning Calorimetry (DSC).....	149
6.8. Thermogravimetric Analysis (TGA).....	157
6.9. Continuous Yarn Manufacturing	160
6.10. References.....	164
 CHAPTER 7	 165
CONCLUSIONS AND RECOMMENDATIONS	165
APPENDIX.....	168

LIST OF TABLES

3.1. Densities of PVA [3].	33
3.2. Nanofiber manufacturing methods [9].	38
3.3. Optimization of the experimental parameters (10% PVA water solution)	39
3.4. Effects on DSC graph areas.	59
4.1. Dimensionless length (b) values.	81
5.1. Thermal conductivity of some materials.....	102
5.2. Some of the polymers' heat deflection temperature and melting points [4].....	103
5.3. Material properties and dimensionless effective thermal conductivities of the hexagonal and rectangular unit cells.....	106
6.1. Dimensionless Effective thermal conductivity by Rule of Mixtures.	125
6.2. Fiber dimensions under SEM.	140
6.3. Air permeability of the samples.....	148
6.4. Surface tension of the solutions.	149
6.5. PVA properties [4]	150
6.6 Comparison of glass transition temperatures.....	154

LIST OF FIGURES

2.1	Typical structure of a composite.....	6
2.2	The variance of the microcopies according to the structure size [19].....	11
3.1	Repeating unit of PVA.....	33
3.2	The structure of Laponite® [4].....	35
3.3	Steps for continuous nano-micro fiber based web yarn manufacturing.....	36
3.4	Parts of the electrospinning setup.....	37
3.5	Nano-micro fiber spread area.....	40
3.6	Schematic shape of nano-micro fiber spread area.....	40
3.7	Direction of electrospinning a) The set-up of Hofman [13], b) The experimental set-up used in the present work.....	43
3.8	Electrospinning with 15kV.....	44
3.9	Electrospinning with 17.5 kV.	45
3.10	Electrospinning with 20 kV.	46
3.11	Forces acting on polymer solution [14].....	47
3.12	Applied voltage effect on the spinning angle.....	48
3.13	Electrospinning direction for 15, 17.5 and 20 kV applied voltage values...	49
3.14	Image of the PVA fiber samples.....	50
3.15	Schematic of the continuous yarn spinning made by SQNT-filled composite [15].....	51
3.16	Schematic of yarn manufacturing.....	53
3.17	Coated fabrics.	54
3.18	Twisting of nano fiber based web.	55
3.19	Heat flow and temperature relationship in DSC [16].	56

4.1	Composite structures for the model a) Cylindrical shape, b) Rectangular shape.....	64
4.2	Hexagonal model for transverse heat conduction. A) 3-D model b) 2-D model (Q: heat flux.)	65
4.3	Symmetric part of the hexagonal model and the region divisions.....	66
4.4	The first region.....	68
4.5	Schematic of the third region.....	69
4.6	Schematic of the fourth region	75
4.7	Schematic of the model without barrier.	82
5.1	Heat conduction in a thin rod [1].....	90
5.2	Number of the nodes on the element [1].....	91
5.3	The finite element division....	93
5.4	Composite structures.....	95
5.5	Radial, axial and 3-D nano-micro composite models (d: the length of the unit cells).....	96
5.6	Necessary computer memory in modeling.....	97
5.7	PLANE35 2-D 6 node triangular thermal solid [3].....	98
5.8	SOLID90 3-D 20 node triangular thermal solid [3].....	98
5.9	Mesh types of 2-D and 3-D nano-micro composite models.....	99
5.10	Problem description.....	101
5.11	Mesh model of the problem.....	101
5.12	Application of two different materials.	102
5.13	Temperature distribution for different materials.....	103
5.14	Maximum heat flux values for composite thermal stability.....	104
5.15	Unit cells a) Rectangle unit cell, b) Hexagonal unit cell.....	105
5.16	Temperature distribution in the X direction for rectangular shape.....	107
5.17	Heat flux variation in the X direction for hexagonal shape.....	108
5.18	Temperature distribution in the X direction for hexagonal shape.....	108
5.19	Heat flux distribution in the X direction for hexagonal shape.....	109
6.1.	Change of dimensionless effective thermal conductivity with β for	

different V_d values, ($t=0$).....	113
6.2. Change of dimensionless effective thermal conductivity with β for different V_d values, ($t=0.1 \times r_d$).....	113
6.3. Change of dimensionless effective thermal conductivity with β for different V_d values, ($t=0.2 \times r_d$).....	114
6.4. Change of dimensionless effective thermal conductivity with β for different V_d values, ($t=0.3 \times r_d$).....	115
6.5. Effect of the barrier thickness on the dimensionless effective thermal conductivity, ($V_d=0.1$).	116
6.6. Effect of the barrier thickness on the dimensionless effective thermal conductivity, ($V_d=0.2$).....	116
6.7. Effect of the barrier thickness on the dimensionless effective thermal conductivity, ($V_d=0.3$).....	117
6.8. k_e^+ calculations for the hexagonal unit cell in ANSYS.....	120
6.9. Dimensionless effective thermal conductivity ($t=0$).	121
6.10 Dimensionless effective thermal conductivity ($t=0.1 \times r_d$).....	121
6.11 Dimensionless effective thermal conductivity ($t =0.2 \times r_d$).	122
6.12 Dimensionless effective thermal conductivity ($t =0.3 \times r_d$).....	122
6.13 Dimensionless effective thermal conductivity ($V_d=0.1$).....	123
6.14 Dimensionless effective thermal conductivity ($V_d= 0.2$).....	123
6.15 Dimensionless effective thermal conductivity ($V_d= 0.3$).....	124
6.16 Dimensionless effective thermal conductivity by the Rule of Mixtures.....	125
6.17 Dimensionless effective thermal conductivity comparison between the ANSYS and Rule of Mixtures ($V_d=0.2$).....	126
6.18 Dimensionless effective thermal conductivity comparison between the ANSYS and Rule of Mixtures ($V_d=0.3$).....	126
6.19 Comparison of the dimensionless effective thermal conductivity among the ANSYS, MATLAB and Rule of Mixtures ($t=0$ and $V_d=0.1$).....	127
6.20 Meshing for the hexagonal model.....	128
6.21 Temperature distribution of the hexagonal unit cell ($t=0$ and $V_d =0.1$).....	129

6.22	Heat flux distribution in the X direction of the hexagonal unit cell ($t=0$ and $V_d=0.1$).....	129
6.23	Heat flux vector in the X direction of the hexagonal unit cell ($t=0$ and $V_d=0.1$).....	130
6.24	Thermal gradient in the X direction of the hexagonal unit cell ($t=0$ and ($V_d=0.1$, $k_d=1000$, $k_f=10$)).....	131
6.25	Heat flux in the X direction of the hexagonal unit cell ($t=0$, $V_d=0.1$, $k_d=0.01$, $k_f=10$).....	132
6.26	Thermal gradient in the X direction of the hexagonal unit cell ($t=0$, $V_d=0.1$, $k_d=0.01$, $k_f=10$).....	132
6.27	Thermal gradient in the X direction of the hexagonal unit cell ($t=0.1 \times r_d$ and $V_d=0.1$).....	134
6.28	Thermal gradient vector in the X direction of the hexagonal unit cell ($t=0.1 \times r_d$ and $V_d=0.1$).....	134
6.29	Thermal gradient in the X direction of the hexagonal unit cell ($t=0.2 \times r_d$ and $V_d=0.1$).....	135
6.30	Thermal gradient in the X direction of the hexagonal unit cell ($t=0.1 \times r_d$ and $V_d=0.1$).....	135
6.31	Heat flux in the X direction of the hexagonal unit cell ($t=0.2 \times r_d$ and $V_d=0.2$).....	136
6.32	Temperature gradient in the X direction of the hexagonal unit cell ($t=0.2 \times r_d$ and $V_d=0.2$).....	136
6.33	Temperature distribution in the X direction of the hexagonal unit cell ($t=0.2 \times r_d$ and $V_d=0.2$).....	137
6.34	Web formation after 1 second of spinning.....	138
6.35	Web formation after 24 seconds of spinning.....	138
6.36	SEM pan.....	139
6.37	SEM image of nanofiber based web (10 wt % PVA, 3000x).....	141
6.38	SEM image of nanofiber bundle (12 wt.% PVA, 10000x).....	141
6.39	SEM image of nanofibers (12 wt. % PVA, 10000x).....	142

6.40	Variety of fiber size (15 wt. % PVA, 3000x).....	142
6.41	Single fiber (12wt. % PVA, 10000x).....	143
6.42	PVA and Laponite® under SEM (12 wt PVA + 5 wt % Laponite®, 10000x).....	144
6.43	Bead problem in electrospinning (15 wt% PVA, 1000x).....	145
6.44	Bead formation [2].....	145
6.45	Load-elongation curve for nano-micro fiber based yarn.....	147
6.46	Comparison of load-elongation curves for nano-micro fiber based yarns...	147
6.47	DSC results of 12 wt % PVA.....	151
6.48	DSC results of 12 wt % PVA+ 1 wt % Laponite®.....	151
6.49	DSC results of 12 wt %PVA+ 2 wt % Laponite®.....	152
6.50	DSC results of 12 wt %PVA+ 3 wt % Laponite®.....	152
6.51	Schematic representation of unfolding of polymer chains a) Original polymer crystal, b) Crystal with a solvent [5].....	153
6.52	Glass transition temperature region for 12 wt % PVA + 1 wt % Laponite®.....	155
6.53	Glass transition temperature region for 12 wt % PVA and 2 wt % Laponite®.....	155
6.54	Glass transition temperature region for 12 wt % PVA and 3 wt % Laponite®.....	156
6.55	Melting point comparison among three samples: 12 wt % PVA + 1wt % Laponite®, 12 wt % PVA + 2wt % Laponite®, and 12 wt % PVA + 3wt % Laponite®.....	157
6.56	Weight loss comparison by TGA up to 300 °C among three samples: Pure 12 wt % PVA, 12 wt % PVA+ 1 wt % Laponite®, and 12 wt % PVA + 3 wt % Laponite®.....	158
6.57	Weight loss comparison by TGA up to 800 °C among three samples: Pure 12 wt % PVA, 12 wt % PVA+ 1 wt % Laponite®, and 12 wt % PVA + 3 wt % Laponite®.....	159
6.58	Picture and schematic of the collecting mechanism.....	161

6.59	Aluminum pool.....	163
6.60	Coated yarns.....	163

CHAPTER 1

INTRODUCTION

Although the term of nano is not a new word in our lives, the usage of nano sized materials is pretty new as well as the attempts to model them. After discovery of carbon nanotubes by Iijima [1], so many new questions have arisen in the field of mechanical, thermal or electrical modeling.

In terms of heat transfer modeling, it brought up a really good question: if the conventional way of thinking to define the heat transfer behavior is still adequate or not. The answer came with the definition of nano scale heat transfer and interface effect. It was shown that, when the free path between the molecules is small enough, the Fourier Law and the Boltzmann equation become inapplicable. This fact moved the researchers to consider and to focus on the molecular level of modeling. Beside, there is the importance of the interface effect. The interface is the result of a large surface area of the nano sized particles when these particles are dispersed inside the composite.

When the single nano sized fiber or nanotube is considered alone, the molecular or atomistic modeling is a good way to solve the problem. If one of the filler of the composite is nano sized, the composite is considered to be a nanocomposite and it becomes hard to have a common feature between nano and micro/macro size particles.

Recently, so many successful application examples are seen in terms of structural, optical, electronics, chemical, flame retardancy properties and the like. Especially carbon nanotubes have been used and taken much attention during the recent years because of their advantage in mechanical, electrical, thermal and chemical properties in the field of supercapacitors, and batteries. In opto-electronic area, oxygen manipulation is done by using nanotubes. To understand the nitrogen dioxide sensing mechanism of tin dioxide nanoribbons, Accelrys uses carbon nanotubes [2]. In pharmaceutical industry, especially in drug delivery, block-copolymers help to increase the circulation time in nanoscopic carrier systems. In semiconductors by Motorola Inc., and Accelrys, thin films are developed by deposition of NO on a Si (100) surface. In automobile, electronics and furnishing industries, clay-polymer reinforced composites are used because of their neat properties. These increasing application areas highlight the nano particles embedded structures, which lead us to consider not only the micro size particle but also nano size particles.

The thermal behavior of nano-micro composites is studied experimentally, analytically, and numerically. For thermal studies, thermal conductivity is chosen because of its direct effect on both thermal and flame resistance behavior. Interfacial effects are important in nano-micro composites and can affect the composite performance. It is known that the interface can decrease the effective conductivity. Therefore, the interface area is also considered in the modeling. For analytical modeling, thermal resistance approach is used by considering a hexagonal unit cell to obtain the transverse effective thermal conductivity ratios. When nano sized fillers is considered, 4-5% of the volume fraction can be enough to give certain properties to the composite. In

micro sized materials, the volume fraction of filler fibers is usually more than 40%. In the hexagonal model, for analytical and numerical analysis, the volume fraction is considered to be between 10-30%.

A novel device was designed to manufacture yarns continuously. Nano-micro fibers were manufactured and collected to form web and yarn. To collect the fibers, nonwoven fabrics were used, which allow easy release of fibers from the surface. Scanning electron microscope, thermal gravimetric analysis, and digital imaging are used to analyze the structures. Tensile strength, surface tension, and air permeability measurements are done.

One of the important objectives of this study is to define the relation between micro and nano sized particles in terms of modeling and manufacturing. For nano scale structure modeling, the current studies include the molecular and atomistic modeling; for the micro or macro level, the conventional methods are considered. What if a nano-micro combination structure is used? This necessitates the discussion of the linkage between nano and micro levels in this study.

1.1. References

1. Iijima, S., "*Helical Mictotubules of Graphitic Carbon*", *Nature*, **1991**, 354, p56.
2. <http://www.accelrys.com/chemicals> (accessed in Jan 2005)

CHAPTER 2

LITERATURE REVIEW

2.1. Nano-micro (NM) Composites

Wool, cotton, chocolate chip cookies, sea, ceramics, clouds, fogs, rain are all composites. When one looks around, it is hard to find a material which is not composite. Composite as a term is described by Milton as: “Composites are materials that have inhomogeneous on length scales that are much larger than the atomic scale but which are essentially homogenous at macroscopic length scales or at least some intermediate length scales [1].

Why do we study composites? This has so many answers. For Poisson it was a tool to describe the magnetism by assuming the body composed of conducting spheres; for Maxwell, it was a tool to solve the conductivity equation in a conducting matrix; for Einstein it was a tool to calculate the effective shear viscosity of a suspension of rigid spheres in a fluid.

A new area recently appeared in our lives is “Nanocomposites”. The reason why the composites are considered nanocomposites is due to the fact that one or more of the components is in a dimension of nano (10^{-9} m). Generally, nanocomposites could be classified into three groups: one dimensional, two dimensional, and isodimensional. The

group of the nanocomposite is contingent on the number of dimensions that the dispersed particles of the composite possess. For example, spherical silica nanocomposite is isodimensional; whereas nanotube, nanocarbon or nanofiber embedded structures are two dimensional. In addition, the filler in the sheet form that has a nanoscale thickness could be given as an example for one dimensional group [2].

Nanocomposites captured a lot of attention recently because of their unique properties. Gilman et al., investigated polymer-clay composites and found that if the mechanical properties are considered, by just adding 5% of silicate mass into the nylon-6, the mechanical properties make significant progress like 40% higher tensile strength, 68% greater tensile modulus, 60% higher flexural strength, etc. On the other hand, heat distortion temperature (HDT) increases from 65 °C to 126 °C. Gas permeability decreases because of the barrier properties [3].

The first report related to polymer-clay composites goes back to Blumstein's research in 1961 [4]. He demonstrated polymerization of vinyl monomers intercalated into montmorillonite (NMT) clay. There are different methods that one could use to prepare nanoclay based composites such as the polymerization (in situ method), solvent-swollen polymer (solution blending), or polymer melt (melt blending).

Polymer-clay composites have two forms: intercalated and delaminated. Intercalated structures were named because of their self-assembled, well-ordered, and multi-layered attitude. The individual silicate layers could be 2 nm or 3 nm. In the laminated structure, the individual silicate layers are no longer close enough to interact with the adjacent layers.

Because of their unique properties, the application areas of nanocomposites are expanding day by day. Solar absorbers can be given as an example, in which silica-carbon nanocomposites are used. The reason to use carbon nanocomposites inside solar energy absorbers is that they absorb more radiation in the solar region [5].

Nanocomposites are also used in automotives as barrier packaging, polyethylene pipe and wire/cable coatings and more [6].

2.2. Interface Effect

Interfaces are found in almost everything. There is an interface even between an ocean and the air. One-dimensional, two dimensional (much common) and three dimensional interfaces could occur in the nature. Between the air and the ocean, one can see also different dimensions. The interface could occur among three material phases such as solid, liquid, and gas. Therefore it is apparent that it is hard to imagine a problem without interface effect including nanostructures (Figure 2.1) [7].

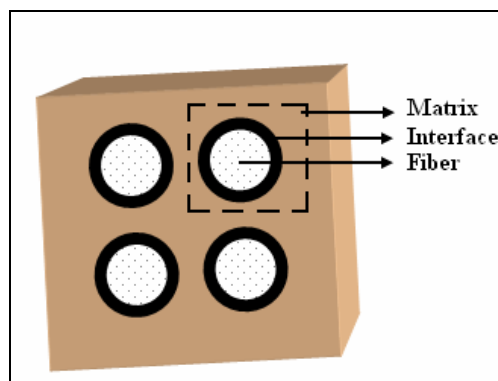


Figure 2.1. Typical structure of a composite

In nano structures, interface bears even more importance since what makes nanostructures unique can be mostly explained by the effect of interface among nanofillers such as fiber, tube, clay, matrix, and the like.

To understand the behavior of interfaces, it is necessary to obtain either experimental or simulation results. Studies indicate that considerable amount of information could be gathered from the simulations because analytical explanations do not suffice. Despite the research studies conducted, there is still room for a clear definition of interface in nanoscale. What do we see at the interface? What kind of bonding could appear? What kind of topology, transport across it, deformation, chemical activities, and forces could appear? These are some of the questions to be addressed. Even if we find answers to these questions, we still may not be able to explain the effect of the interface sufficiently [8].

Van Assche and Van Mele, discussed the effect of interphase. They emphasized that macroscopic properties of composite materials, including fiber-reinforced polymers, blends, and multilayer systems, were often strongly affected by the development of interphase regions with properties differing from the properties of the constituent materials. Interphases could arise due to preferential adsorption, catalytic influences of a surface, inter-diffusion, phase separation, etc. The resulting gradients in composition (polymer blends) or crosslink density (thermosets) lead to gradients in the microscopic properties [9].

The load transfer from the polymer to nanotubes depends on three factors: the interaction between the nanotubes and polymer, micro-mechanical interlocking between nanotubes and polymer, and the chemical bonding between nanotubes and polymer. If the

nanotubes have chemical stability, the effect of the chemical bonding could be negligible. Studies regarding the effect of interface in nanosize structures started in the last 10 years [10].

Lopattananon et al., emphasized the importance of micromechanical test to characterize the mechanical properties of the interface. They used single-fiber fragmentation method because of its simplicity. This method applies a tensile force to a specimen with a single embedded fiber in a thin resin test piece. They also claim that the term of good interface is one which transfers the highest fraction of the applied load in the form of a stress to the fiber [11].

In another study, Van Assche and Van Mele used micro-thermal analysis to study the interphases in a particle-filled composite based on an epoxy resin matrix. In their analysis, they combined the advantage of thermal analysis (characterization) and microscopy (visualization). They also studied spatial variations in glass transition and melting behavior by performing local thermal analysis. To detect the interface by micro-TA, the first step to be taken is to map the surface to find topography and thermal properties. Then for characterizing the interface close to particles, local thermal analysis is used. Thermal probe is embedded in the composites and moved. Thus the change in the properties is presented [12].

Naslain explained the importance of the interfacial part [13]. It controls the crack deflection, load transfer, diffusion barrier, and residual stress relation. Naslain mentioned one of the classical approaches to design fiber-matrix (FM) interfacial zone in ceramic matrix composites (CMCs) from a processing standpoint which is through the in situ

formation of a weak interphase resulting from some chemical reaction at the FM interface during the high temperature step of composite processing.

In some models, it was assumed that interface has no thickness. Some researchers indicated that the interface could not be homogenous and has a thickness less than 1 μm . Also it is emphasized that there is a discrepancy in the interphase, and sometimes estimation could be used for its properties.

In micro level, the length of the interface could be in nanoscale. In nanoparticle embedded composites, it may be even smaller, which makes it difficult to measure.

There are two main functions of interfaces for ceramic matrix composites: the first one is to act as a mechanical fuse and to maintain a good load transfer between the fibers and the fabric. In addition, in very reactive systems, the interphase could act as a diffusion barrier [13].

In modeling, Theocharis and Panagiotopoulos presented a novel concentric cylindrical model for growing phase of the interphases. They also showed the properties as a function of radial distance from the fiber. It is suggested that some test methods could be used to measure the mechanical properties; however, for thermal analysis, there were no direct methods until 2001. After the development of the atomic force microscopy, new concepts appeared in the interfacial area and measuring the nanoscale thermal properties of the materials at nanoscale became possible. They used thermal atomic force microscopy to evaluate the interface. It was also shown that, epoxy resin, curing agent and fiber systems are important factors for interphase properties [14].

Interfaces are important because, during the manufacturing of composites, large number of cracks could appear especially at the interfaces which could cause weak

bonding. For stress distribution of these cracks, the interfaces were considered as an extension of the matrix. There are some studies in which these effects are investigated by finite element method or boundary element method [15].

Interphase may not be as important in some situations as was shown by Ash et al. In this study, the effect of the interface was compared to the effect of the separation of the blade or other wise angle in microband test, and it was proposed that the interface is not as important as the wise angle [16].

The shape of the interface is not often regular. Lipscomb and Xomeritakism analyzed the mass transfer in composite materials that have irregular interfaces. In some considerations, this irregularity is assumed linear. The irregularity gives much permeability to the composites [17].

Pegoretti et al., studied the toughness of the fiber matrix interface in nylon-6/glass composites experimentally. They also used finite element modeling to measure the interfacial bonding [18].

Until the 1980s, information on the sub-micrometer scale length was accessible only using the indirect techniques such as electron or X-ray diffraction or with electron microcopies which required vacuum environment and conductive materials. The inventing of Scanning Tunneling Microscope (STM) in 1982 was changed this. It was aimed to generate real-space images of surfaces with a resolution on the nanometer scale. The Atomic Force Microscope (AFM), known also as Scanning Force Microscope (SFM) came after this invention. Thus, it became possible to investigate the insulating materials such as polymers and biomolecules [19]. The variance of the microcopies can be seen in Figure 2.2.

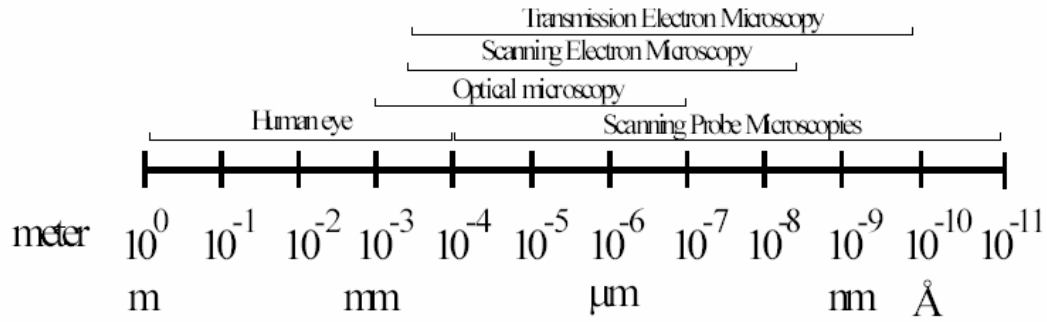


Figure 2.2. The variance of the microcopies according to the structure size [19].

In nanosized structures, it is known that interface improves the material properties including structural, thermal, and mechanical resistance. Wu et al., determined that, by adding nanosized clays into the polymer, because of the interaction between the matrix and clay interface, the mechanical properties increase [20].

Chemical characteristic of the surface and the interface of TiO_2 -muscovite nanocomposites were studied by Song et al. They used scanning electron microscopy (SEM), transmission electron microscopy (TEM) and X-ray photoelectron spectroscopy (XPS). In this study, it is emphasized that the crystallization of the structure started at the interface [21].

To enhance the understanding of solid-solid interface thermal conductance, thermal transport through highly perfect interfaces between epitaxial TiN and single crystal oxides were measured. Thermal conductance plays an important role in the thermal transport area in nano scale structures. Thermal modeling is done to find the thermal conductance. The thermal conductance was modeled by dividing the lock-in-phase component of the lock-in-signal by lock-out phase component of the lock-in-signal. It can be seen from the calculations that lateral heat flow could be negligible but radial

heat flow can not be. The interface disorder in samples produces strong phonon scattering at the interface. The interface disorder in all samples is weak and transmission coefficient is always close to unity. Diffuse mismatch model and lateral dynamic calculations can be used to compare with the model [22].

2.3. Electrospinning

Electrospinning, as described by Shin as “a garden hose, whipping around the water squirts out one end” is not a new method [23]. It has been known since 1934 by the approval of several patents [24-27].

A high voltage is used to spin an electrically charged jet of polymer solution or melt, which dries or solidifies to leave a polymer fiber [28-29]. One of the electrodes is placed into the spinning solution and the other one is attached to the collector. Capillary tube which contains the polymer fluid is subjected to the electrical field by its surface tension. This makes a charge on the surface of the liquid and the surface of the fluid is seen in the form of a conical shape known as Taylor cone. When the electricity in the field is increased, a critical value is attained, the repulsive electrostatic force overcomes the surface tension and a charged jet of fluid is ejected from the tip of the Taylor cone.

2.4. Thermal Properties of Nano-Micro Composites

In conventional heat transfer and fluid flow concepts, fluid phase is considered continuous by including properties such as thermal conductivity, pressure or domain temperature. In the nano-scale, the continuum treatment does not hold because the domain is not enormously bigger than molecular scale and therefore the Fourier's law is

not applicable. Thus explanation of the domain has to contain the collection of the molecules.

2.4.1. Thermal Conductivity in Macro Level

Polymers can have an interaction with different kind of fillers and these fillers can be in the form of fibers. One of the important properties necessary to define the behavior of the composites is thermal conductivity. It is known that the thermal conductivity of a material has a direct relationship with the flammability of the material.

There are theoretical studies to explain effective thermal conductivity such as using the two phase mixtures concept, etc.

As a simple approach for unidirectionally aligned model, the components are thought to be arranged in layers and placed in serial or parallel to heat flow. Thus the thermal conductivity is calculated as follows:

For the series model:

$$k_c = \frac{k_m k_f}{k_m (1 - \nu) + k_f \nu} \quad (2.1)$$

For the parallel model:

$$k_c = \nu k_f + (1 - \nu) k_m \quad (2.2)$$

where, k_c , k_f and k_m are respectively the thermal conductivities of the composite, filler materials and polymer matrix, and ν is the volume fraction of fiber.

Maxwell obtained a relationship for the conductivity of randomly distributed fibers as follows [30];

$$k_c = k_m \frac{k_f + 2.k_m + 2.\phi.(k_f - k_m)}{k_f + 2.k_m - \phi.(k_f - k_m)} \quad (2.3)$$

where ϕ is the volume fraction of the fiber.

Lewis and Nielsen [31] derived a model by modification of Halpin-Tsai equation and including the effect of particle structure.

There are some analytical and numerical models in macro-size composites, but these models mostly focus on either random short fibers or aligned short fibers.

$$k_c = k_m \frac{1 + A.\beta.\phi}{1 - \beta.\phi.\psi} \quad (2.4)$$

Where;

$$\beta = \frac{k_f/k_m - 1}{k_f/k_m + A} \quad \text{and} \quad \psi = 1 + \frac{1 - \phi_m}{\phi_m^2} \phi \quad (2.5)$$

Where ϕ_m is the packing factor, A is a factor that depends on the shape and orientation of the particles.

Hatta and Taya, by using equivalent inclusion method for steady state heat conduction, discussed the effective thermal conductivity, showing the importance of the interaction between the fiber orientation and composite. To do this, some numerical methods were used which considered the volume fraction, fiber aspect ratio and distribution as factors [32].

When the fibers are arbitrarily placed, Nan and Birringer introduced a method to determine the effective thermal conductivity (k_e) of the composite by combining the interfacial contact resistance with Kapitza thermal contact resistance [33].

Esparragozaa et al., gave a simple analytical approach to define temperature distribution in a cylindrical domain which consists of a single fiber inside. The principle of conservation of energy was used for the boundary layer [34].

Hasselmann and Donaldson worked on the inclusion size and discussed the effect of thermal conductivity; the thermal barrier effect was demonstrated experimentally [35].

To measure the thermal conductivity of fiber reinforced composites, Sweeting and Liu had developed a model by applying a thermal gradient to the composite and measuring the heat flow [36].

Islam and Pramitam presented a model to predict the transverse thermal conductivity of composites including the effect of interface by using FEM [37].

2.4.2. Thermal Conductivity in Nano Level

In contrast to mechanical studies, there is not much study in the field of heat transfer at the nano level. The existent studies focus on thin films, carbon nanotubes and their derivatives.

It is clear that the nano scale heat transfer differs from the Fourier law because of the boundary and interface scattering and the finite relaxation time of heat carriers. It is shown by Cahill et al., that there is a linear connection between interface density and thermal conductivity in Si and Ge superlattices [38].

In single walled carbon nanotubes (SWCNs), thermal transport is explained by the phonons. SWCNs has a thermal management in high performance. Phonons dominate thermal transport at all temperatures in carbon materials.

The phonon thermal conductivity could be demonstrated as

$$\kappa=C_p*\nu_s* l. \quad (2.6)$$

In this equation C_p is the specific heat, ν_s is the speed of the sound and l is the mean free path. This equation is applicable for both one-dimensional phonon systems and SWNTs [39].

To study the size effect in nano level, Boltzmann equation could be used with some limitations. These limitations are because of the geometries such as thin films and superlattices. The transient ballistic diffusive equation is applied to study two dimensional non local, phonon transport phenomena [40]. Beside this, Chen used the ballistic diffusive heat conduction equations under the relaxation time. The ballistic-diffusive equations are used because of the suitability for fast heat conduction process and also small structures. It can be used to measure transient heat conduction [41].

The measurement methods become more important for nanoscale metrology such as the 3ω method, time domain thermoreflectance, sources of coherent phonons, micro-fabricated test structures and scanning electron microscope.

Cahill et al., summarized the thermal studies in nanostructures in a critical review about the thermal transport [42]. Although this work focused on electronic devices, it gives a brief understanding about thermal transport. Mirmira and Fletcher summarized most of the studies related to thermal transport in nano scale. Several studies related to thermal conductivity of thin films were given [43]. Several studies exist regarding the effective thermal conductivity modeling for thin films. When the experimental and theoretical models are analyzed, it becomes clear that, there are many assumptions in the models and they are only for some kind of specific structures or materials, and only in the steady state situation, neglecting other cases. There is not an available model which could

be used for different kind of structure types. Some of the leading studies in nano thermal areas is summarized below.

The first indication of thermal stability improvement in nanocomposites appears in the work by Blumstein [4] who studied the thermal stability of poly(methyl methacrylate) (PMMA) intercalated within montmorillonite. Che and Cagin studied the thermal conductivity of nanotubes and they found that the carbon nanotubes had very high thermal conductivity comparable to diamond crystal and in-plane graphite sheet. They also showed that nanotube bundles had similar properties to graphite crystal in which dramatic difference in thermal conductivities along different crystal axis was observed [44]. Heat capacity of carbon nanotubes was studied by Benedict and his co-workers to find out how the heat capacity of small nanotubes could be measurably different than that of bulk graphite. They predicted that all single-walled tubes should have sufficient heat capacity [45]. The heat conduction in finite length single-walled carbon nanotubes (SWNTs) was simulated by the molecular dynamics method with the Tersoff–Brenner bond order potential; the thermal conductivity was calculated from the measured temperature gradient and the energy budgets in phantom molecules by Shigeo Maruyama [46,47]. On the other side, for finding thermal expansion and diffusion coefficients of carbon nanotube-polymer composites, classical molecular dynamics simulations are used.

Ando studied electronic and transport properties by using experimental methods. He demonstrated that carbon nanotubes (CNs) are important in terms of transport properties and this is the result of their extraordinary structures [48].

2.4.3. Flame Resistance

To protect from fire and to survive in a place which shows huge temperature difference is of vital importance for life. The factors related to fire hazards can be explained by ignitibility, ease of extinction, flammability of the generated volatiles, amount and rate of heat released on burning, flame spread, smoke obscuration and smoke toxicity [49].

Although the leading nano studies begin with the study of Iijima in carbon nanotubes [50], the flammability studies of nano scale clay embedded composites start with Gilman et al., after 1995 [51] and focus on experimental work and simulations.

There are some important factors in flame resistance behaviors. Heat release (HR) is important because it causes a fast ignition and a flame spread. HR helps to control the fire intensity and is therefore much more important than the ignitability. Also it is underlined by the National Institute for Standards and Technology (NIST) as a single important factor.

The importance of the new developments is emphasized by Gilman et al. on organic treatments of montmorillonite. The flammability of thermoplastic and thermoset polymer layered silicate nanocomposites were investigated. It was found out that peak and average heat release rates (HRR) were significantly improved. The main difference between the pure vinyl esters and the nanocomposites is the mass loss rates. They also reported that heat combustion, and carbon monoxide yields do not change [51].

Thermogravimetric analysis (TGA) characterizes the thermal stability of a polymer. The mass loss because of the decomposition can also be determined as a function of temperature.

Cone Calorimeter (CC) is used to measure HR. It uses the relationship between the oxygen consumed from the air and the amount of heat released during the polymer degradation. Using CC allows to measure heat release rate (HRR) and carbon monoxide ratio. HRR is important to evaluate fire safety [52]. Five properties could be measured by CC:

- Peak Heat Release (PHR)
- Mass loss rate (MLR)
- Specific extension area (SEA)
- Ignition Time (T_{ign})
- Carbon monoxide and carbon dioxide yield.

One important advancement in the flammability studies is clay treatment. It affects the thermal stability also. Nyden and Gilman, discussed the importance of clay treatment in their study.

An important factor aspect in nanocomposites is the relation between flammability and physical properties. It was underlined that, nano-dispersed montmorillonite causes non-char forming polymers. The dispersed clay helps with insulating and therefore the flame resistance increases. Nyden and Gilman used molecular dynamic methods to understand the flammability reduction. They used experimental measurements for comparison. The comparison was done according to mass loss which was calculated as a function of the distance of separation between the graphite sheets. As a molecular dynamic method they used MD_REACT method which is based on Hamilton's equations [53].

In another study, experimental results showed that the rate of mass loss from polymer-clay nanocomposites exposed to fire-like heat fluxes is significantly reduced from the values observed from the immiscible composites containing the same amounts of polymer and clay [54].

Morgan et al., prepared nanocomposites of polypropylene -graft- maleic anhydride with organically modified clays. They studied the combustion behavior and observed synergy between the nanocomposite and conventional phase fire retardants [55].

Zhu et al., prepared three organically modified clays and used them to produce nanocomposites. They investigated the behavior using X-ray diffraction and transmission electron microscopy. For characterization, thermogravimetric analysis and cone calorimeters were used [56].

The flame resistance of carbon nanotubes was investigated by Vander Wall and Hall. They used a configuration to demonstrate the flame resistance. They prepared intercalated, exfoliated and mixture of both forms [57].

Carbon nanotubes have unique properties; however it is difficult to functionalize them because of their basal plane sites. Also this plane is not accessible by interstitial lattice sites for intercalation. However this is not seen as a disadvantage in nanofibers because they are composites of short carbon segments [58].

The flammability studies mostly focus on polymer clay nanocomposites. Morgan et al., used polystyrene clay composites to define the flammability properties in nanoscale. They obtained intercalated polymer-clay nanocomposites. They obtained a lower ratio of HRR and found that the total burn time was increased [59].

Gilman and his co-workers used both polystyrene and polypropylene nanocomposites [54].

Nyden and Gilman, established a new processing capability for variable composition samples which are extruded, analyzed and burned on the same device. This allows for easy measurements from one sample to define the flammability properties [53].

2.5. Modeling

In macroscopic problems, for heat conduction in a very thin film of solid atoms, the thermal energy is in the form of potential energy. Therefore the heat conduction is an interaction between atoms and molecules. In a very thin film, thermal conduction depends on the dimension of the space domain. If the domain is large enough, one can see kinetic and potential interactions. The linear relationship between heat flux and temperature gradient is linear [60].

According to molecular dynamics approach, which is assumed to be the best approach for understanding the nano phenomena, there are three different techniques for measuring thermal conductivity in nano scale structures. The first one is equilibrium molecular dynamics which is based on Green-Kubo's formula; the second one is non-equilibrium formula and the last one is non-equilibrium molecular dynamics with direct temperature difference.

Osman and Srivastava calculated the thermal conductivity of single-walled carbon nanotubes over a temperature range of 100-500 K using molecular dynamic calculations.

They used Tersoff-Brenner potential for carbon-carbon (C-C) interactions [61]. Berber et al., combined the equilibrium and non-equilibrium molecular dynamic simulations to find the unusually high thermal conductivity: 6600 W/mK [62].

When the correctness of the Fourier's law is discussed, the usage of this law in nano scale is also questioned. In molecular dynamics calculations, this law could be applicable only for non-equilibrium calculations. Because of the relation between the heat diffusion length and the time for diffusion, Fourier's law could leave its place totally to the molecular dynamics calculations and to the ultra short time scale studies.

In an another study, it was shown that for the heat conduction of thin films, the temperature gradient increases with respect to the heat flux and the average temperature. The thickness and the initial temperature do not play a role [63]. By using two parameters such as the positional order parameter and the kinetic H-function, the equilibration of heat conduction simulations for thin films was investigated. This method also could be applied for macroscopic molecular dynamic simulations to investigate the heat transfer behavior.

Nanostructures such as superlattices and quantum wires give the researchers a chance to develop alternative methods for electron and phonon transport processes. Some of the structures want lower thermal conductivity and higher electrical conductivity such as thermionic refrigeration and power generation operations. Also nano-clay embedded structures can be given as an example in which lower thermal conductivity is wanted. In a study by Chen et al., these structures for solid-state energy conversions were discussed [64]. Thermal conductivity was explained by Ren and Dow in the area of superlattices [65].

It is pointed out by Cahill et al., that, when the interface density increases, the heat conduction decreases. This is an important point to define the difference between nano and macro scale structures [38].

Much of the early work studying the mechanical properties of nanotubes utilized computational methods such as molecular dynamics. These models focused primarily on Single Walled Carbon Nanotubes (SWNTs) because of the increase in computational resources necessary to model larger systems.

Nyden and Gilman performed molecular dynamics simulations for the thermal degradation of polymer nanocomposites in an attempt to explain the reduction in the flammability of nano-confined polypropylene as compared to the pure polymer [53]. Laplaze et al., studied the carbon nanotubes to understand the dynamics of synthesis processes. He obtained heat and mass transport in a solar reactor using ‘in situ’ measurements linked to numerical simulation [58]. 3-D finite element modeling was used to study the influence of nonlinear response of organic components. In another work, nonlinear elasto-plastic models for the organic component are applied to model the mechanical response of nacre (mother of pearl). Nanoscale material parameters (elastic modulus and hardness) were obtained using nanoindentation experiments. Fisher et al. predicted the modulus using effective nanotube properties. In their study they used ANSYS program as a finite element method. They used the micromechanical techniques to study the effective elastic moduli of nanotube-reinforced polymers [66].

To deal with nanosize, one should resort to modeling in both atomistic and molecular level. Moreover, in heat transfer and fluid flow treatments, as the size of the flow domain approaches to nano level, the continuum treatment breaks down since the

fluid consists of molecules and, when the flow domain size is no longer enormously greater than molecular scale, the fluid must be considered in terms of collections of molecules.

As an atomistic model, Brenner developed an empirical model for nanotubes that depends on Tersoff's covalent bonding [67]. Hannson et al., used the molecular dynamic simulations to get the electronic behavior of the carbon nanotubes [68].

2.6. References

1. Milton, G. W., "The Theory of Composites"; Cambridge Univ. Press, **2002**.
2. Dubois, A. M., "Polymer-layered Silicate Nanocomposites: Preparation, Properties and Uses of a New Class of Materials", Materials Science and Engineering **2000**, 28, 1-63.
3. Gilman, J. W., Margon, A. B., Harris, R. Jr., "Polymer Layered-Silicate Nanocomposites: Polyamide-6, Polypropylene and Polystyrene", New Advances in Flame Retardant Chemicals Association Proceedings, **1999**, 22.
4. Blumstein, A., "Polymerization in Adsorbed Layers I.", Bull. Chim. Soc., **1961**, 889-905.
5. Mastai, Y. S., and Antonietti, S. P., "Silica-Carbon Nanocomposites – A new Concept for the Design of Solar Absorbers", Adv. Func. Mater., **2002**, 12.
6. <http://www.plasticstechnology.com/articles/200110fa3.html> (accessed in Jan. 2005).
7. MacRitchie, F., "Chemistry at Interfaces", Academic Press, Inc., **1990**.

8. Glotzer, S. C., “*Computer Simulations of Spinodal Decomposition in Polymer Blends*”, Annual Reviews of Computational Physics, **1995**, 2, 1-46.
9. Van Assche, G., and Van Mele, B., “*Interface Formation in Model Composites Studied by Micro-Thermal Analysis*”, Polymer, **2002**, 43, 4605-4610.
10. Gou J., Liang, Y., Zhang, C., and Wang, B., “*Molecular Dynamics Simulations of Interfacial Bonding of Single-walled Nanotubes Reinforced Epoxy Composites*”, ICCE-10 conference, New Orleans, July **2003**.
11. Lapottananon, N., Hayes, S. A., and Jones, F. R., “*Evaluation of Fibre-matrix Interfacial Adhesion for Carbon Fibre/epoxy Composites*”, in the 28th Congress on Science and Technology of Thailand, **2002**, Bangkok, 772.
12. Van Assche, G., and Van Mele, B., “*Interphase Formation in Model Composites Studied by Micro-thermal Analysis*”, Polymer, **2002**, 43, 4605-4610.
13. Naslain, R. R., “*The design of the Fibre-matrix Interfacial Zone in Ceramic Matrix Composites*”, Composites Part A **1998**, 29A, 1145-1155.
14. Theocharis, S. G. E., and Panagiotopoulos, P. D, “*Calculation of Effective Transverse Elastic Moduli of Fiber-reinforced Composites by Numerical Homogenization*”, Compos. Sci. Technol., **1997**, 57, 573-586.
15. Liu, Y. J., and Xu N. ,”*Modeling of Interface Cracks in Fiber-reinforced Composites with the Presence of Interphases Using the Boundary Element Method*”, Mechanics of Materials, **2000**, 32, 769-783.
16. Ash J. T., Cross, W. M., Svalstad, D., Kellar, J. J., and Kjerengtroen L., “*Finite Element Evaluation of the Microbond Test; Meniscus Effect, Interphase Region, and Vise Angle*”, Composites Science and Technology **2003**, 63, 641-651.

17. Lipscomb, G., and Xomeritakism, G., "*Analysis of Mass Transfer in Composite Materials with Irregular Interfaces*", Journal of Membrane Science **1995**, 103, 1-10.
18. Pegoretti, A., Fidanza, M., Migliaresi, C., and Di Benedetto, A. T., "*Toughness of the Fiber/Matrix Interface in Nnylon-6 Glass Fiber Composites*", Composites: Part A **1998**, 29A, 283-291.
19. Samorí, P., "*Self-assembly of Conjugated (Macro) Molecules: Nanostructures for Molecular Electronics*", Ph.D thesis, **2000** (accessed by web link: <http://prophysik.chemie.de/publikat/samorithesis.pdf> in 2004).
20. Wu S. W. Wu, S. H., Wang, F. Y., Ma, C. C. M., Chang, W. C., Kuo, C. T., Kuan, H. C., and Chen W. C., "*Mechanical, Thermal and Morphological Properties of Glass Fiber and Carbon Fiber Reinforced Polyamide-6 and Polyamide-6/ clay Nanocomposites*", Materials Letters, **2001**, 49, 327-333.
21. Song, G. B., Joly, H., Liu, F. S., Peng, T. J., Wan, P., and Liang, J. K., "*Surface and Interface Characteristics of TiO₂-muscovite Nanocomposites*", Applied Surface Science, **2003**, 220, 1(4), 159-168.
22. Costescu, R. M., Wall, M. A., and Cahill D. G., "*Thermal Conductance of Epitaxial Interfaces*", Phys. Rev. B **2003**, 67, 05430 2.
23. Shin, MPC Industry Collegium Report, Vol. 17, No. 3, June **2001**.
24. Formhals A., "*Process and Apparatus for Preparing Artificial Threads*", US patent 1,975,504, **1934**.
25. Formhals A., "*Artificial Fibers from Materials such as Cellulose Acetate*", US patent 2,158,415, **1939**.

26. Formhals A., "Apparatus for producing artificial fibers from fiber-forming liquids by an "electrical spinning" method. " US patent, 2,323,025, **1943**.
27. Formhals A., "*Spinner for Synthetic Fibers*". US Patent, 2,349,950, **1944**.
28. Hohman, M. M., Shin, M., Rutledge, G., and Brenner M., "*Electrospinning and Electrically Forced Jets. I. Stability Theory*", *Physics of Fluids*, **2001**, 13, 8, 2200-2220.
29. Hohman, M. M. Shin, M., Rutledge, G., and Brenner M., "*Electrospinning and Electrically Forced Jets. II. Applications*", *Physics of Fluids* **2001**, 13, 8, 2221-2236.
30. Maxwell, J. C., "*A Treatise on Electricity and Magnetism*" Dover (3rd Ed.), New York, 9, **1954**.
31. Lewis, T., and Nielsen, L. "*Dynamic Mechanical Properties of Particulate-filled Polymers*", *J. Appl. Polym. Sci.* **1970**, 14, 1449.
32. Hatta, H., and Taya, M., "*Effective Thermal Conductivity of a Misoriented Short Fiber Composites*", *Journal of Appl. Phy.*, 1985, 57(7), 2478-2486.
33. Nan, C. W., and Birringer, R., "*Effective Thermal Conductivity of Particulate Composites with Interfacial Thermal Resistance*", *American Institute of Physics*, **1997**, 81(10), 6692.
34. Esparragozaa, I. E., Azizb, A. H., and Damleb A. S., "*Temperature Distribution along a Fiber Embedded in a Matrix under Steady State Conditions*", *Composites: Part B* **2003**, 34, 429–436.

35. Hasselman, D. P. H., and Donaldson, Y. J., “*Role of Particle Size in the Effective Thermal Conductivity of Composites with an Interfacial Thermal Barrier*”, *Journal of Wide Band Gap Mat.*, **2000**, 7(4), 306.
36. Sweeting, R. D., and Liu, X. L., “*Measurement of Thermal Conductivity for Fiber-reinforced Composites*” *Composites Part A* **2004**, 35A (7-8), 933-938.
37. Islam Md. R, M. Pramila, A., “*Thermal Conductivity of Fiber Reinforced Composites by the FEM*”, 1999, *J. Comp. Mater*, 33, 1699.
38. Cahill, D. G., Ford, W.F., Goodson, K.E., Mahan G.D., Majumdar, A., Maris, H.J., Merlin R., and Phillpot S.R., “*Nanoscale Thermal Transport*”, *Journal of Applied Physics*, **2003**, Vol 93, No 2., 793-818.
39. Biercuk, M., Llaguno, M. C., Radosavljevic, M., Hyun, J. K., Fischer, J. E. and Johnson, A. T., “*Carbon Nanotube Composites for Thermal Management*” *Applied Physics Lett.*,**2002**, 80, 2767- 2769.
40. Yang, R., and Chen, G., “*Two-dimensional Nanoscale Heat Conduction Using Ballistic-Diffusive Equations*”, presented at IMECE 2001, New York.
41. Chen, G., “*Ballistic-Diffusive Equations for Transient Heat Conduction From Nano to Macroscales*”, *Journal of Heat Transfer*, **2002**, 124(2), 320-328.
42. Cahill, D., Goodson, K., and Majumdar, A., “*Thermometry and Thermal Transport in Micro/nanoscale Solid-state Devices and Structures*”, *Journal of Heat Transfer*, **2002**, 124, 223.
43. Mirmira, S. R., and Fletcher, L. S., “*Review of the Thermal Conductivity of Thin Films*”, *Journal of Thermophysics and Heat Transfer*, **1998**, Vol.12, No.2, 121-131.

44. Che, C., and Cagin T., "*Thermal Conductivity of Nanotubes*", Nanotechnology, 7th Conference on Molecular Technology, **1999**, California.
45. Benedict, L. X., Louie, S. T., and Cohn, M. L., "*Heat Capacity of Carbon Nanotubes*", Solid State Commun., **1996**, 100, 177
46. Maruyama, S., "*A Molecular Dynamics Simulation of Heat Conduction of Finite Length SWNTs*", Physica B, **2002**, 323, 1-4, 193-195.
47. Maruyama, S., "*Molecular Dynamics Method for Microscale Heat Transfer*", Advances in Numerical Heat Transfer, **2000**, 2, 189-226.
48. Ando, T., "*Theory of Transport in Carbon Nanotubes*", Semicond. Sci. Technol., **2000**, 15, 12-27.
49. Beyer, G., "*Nanocomposites: a New Class of Flame Retardants for Polymers*", Plastics Additives & Compounding, **2002**, 4(10), 22-28.
50. Iijima, S., "*Helical Microtubules of Graphitic Carbon*", S Nature, **1991**, 354, p56.
51. Gilman, J. W., Kashiwagi, T., Nyden, M. R., Brown, J. E. T., Jackson, C. L., Lomakin, S. M., Giannelis, E. P., and Manias, E., "*Flammability Studies of Polymer Layered Silicate Nanocomposites: Polyolefin, Epoxy, and Vinyl Ester Resins*", Chemistry and Technology of Polymer Additives, **1999**, 14, 249-265.
52. Babrauskas, V., and Peacock, R.D., "*Heat Release Rate: the Single most Important Variable in Fire Hazard*", Fire Safety Journal, **1992**, 18, 255-261.
53. Nyden, M. N., and Gilman, J., "*Molecular Dynamics Simulations of the Thermal Degradation of Nano-confined Polypropylene*", Flammability of Polystyrene-Clay Nanocomposites", Comp. Theor. Polymer Sci., **1997**, 7, 191-198.

54. Gilman, J. W., Jackson, C. L., Morgan, A. B., Harris, R. H., Jr., Manias, E., Giannelis, E. P., Wuthenow, M., Hilton, D., and Phillips, S. H., "Flammability Properties of Polymer-layered-silicate Nanocomposites, Polypropylene and Polystyrene Nanocomposites", Chem. Mater, **2000**, 1866-1873.
55. Morgan, A., Gilman, J. W., Harris, S. and Jackson, J., "Flammability of Polystyrene-clay Nanocomposites", Polymeric Materials Science & Engineering (ACS), **2000**, vol. 83, p53.
56. Zhu, J., Lamelas, F. J., and Wilkie, C. H., "Fire Properties of Polystyrene – clay Nanocomposites", Chem. Mater., **2001**, 13, 3774-3780.
57. Vander Wal, R. L. and Hall, L. Z., "Flame Synthesis of Fe Catalyzed Single-walled Carbon Nanotubes and Ni Catalyzed Nanofibers: Growth Mechanisms and Consequences", Chemical Physics Letters, **2001**, 349,178-184.
58. Laplaze D. , Alvarez, L., Guillard, T., Badie J.M., and Flamant G., "Carbon Nanotubes: Dynamics of Synthesis Process", Carbon, **2002**, 40, 1621-1634.
59. Morgan, A. B., Gilman, J. W., Harris, R. H., Jr., Jackson, C. L., Wilkie, C. A., and Zhu, J., "Flammability of Polystyrene-clay Nanocomposites", Polymer. Mater. Sci. Eng., **2000**, 83, 53-54.
60. Wan, X., "Study of Heat Transfer at Micro-and Nanoscales in Ultrashort Time Domain", Purdue University, 2001.
61. Osman, M., and Srivaskava, D., "Temperature Dependence of the Thermal Conductivity of Single-walled Carbon Nanotubes", Nanotechnology, **2001**, 12, 21-24.

62. Berber S., Kwon, T., and Tomanek, D., “*Unusually High Thermal Conductivity of Carbon Nanotubes*”, Physical Review of Carbon Nanotubes, **2000**, 84, No20.
63. Maruyama, S., “*Molecular Dynamics Method for Microscale Heat Transfer*”, Advances in Numerical Heat Transfer, **2000**, 2, 189-226.
64. Chen, G. Yang B., Liu, W., and Zeng, T., “*Nanoscale Heat Transfer for Energy Conversion Applications*”, Proc. Energy conversion and Applications, **2001**, 1, 28-296.
65. Ren, S.Y., and Dow, J., “*Thermal Conductivity of Superlattices*”, Phys. Rev. B, **1982**, 25, 3750-3755.
66. http://www.mech.northwestern.edu/fac/brinson/nano/pubs/FT_Fisher_PhD_Thesis_ALL.pdf (accessed in June 2004).
67. Brenner, D., “*Empirical Potential for Hydrocarbons for use in Simulating the Chemical Vapor Deposition of Diamond Films*”, Physical Review B, **1990**, 42(15), 9458-9471.
68. Hannson, A., Paulsson, M., and Stafström, S., “*Effect of Bending and Vacancies on the Conductance of Carbon Nanotube*”, Physical Review B, **2000**, 62(11), 7639-7644.

CHAPTER 3

NANO-MICRO FIBER BASED FILM, WEB AND YARN MANUFACTURING

In this chapter, experimental studies are explained for nano-micro fiber based film, web and yarn manufacturing. Thus, electrospinning, electrical field, optimum properties of spinning, coating, differential scanning microscopy (DSC), thermo gravimetric analysis (TGA), scanning electron microscope (SEM), air permeability and surface tension of the fabric are discussed.

3.1. Materials

3.1.1. Polyvinyl Alcohol (PVA) Properties

The reason why PVA is selected in this work is because polyvinyl alcohol based fibers have been used for a long time as a reinforcement for polyester resins and the solution preparation does not take much time [1]. Besides, PVA provides high polarity and hydrogen bonding. This makes PVA infusible but soluble in water. Commercially, PVA is classified in two groups: partially and fully hydrolyzed PVA, which depends on the amount of acetate groups they have.

PVA is resistant to oils, fats, greases and it provides strong adhesion for paper and textiles. The chemical structure of PVA is seen in Figure 3.1 [2].

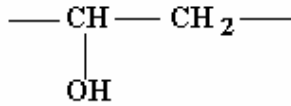


Figure 3.1. Repeating unit of PVA.

PVA's density may change depending on its amorphous and crystalline structure. As seen in Table 3.1, the density of the amorphous part of the polymer (ρ_a) is around 1.26 g/cm³ and the density of the crystalline part of the polymer (ρ_c) is around 1.35 g/cm³. This gives a ratio of $\rho_c/\rho_a = 1.07$.

Table 3.1. Densities of PVA [3].

	ρ_c (g/cm ³)	ρ_a (g/cm ³)	ρ_c/ρ_a
PVA	1.35	1.26	1.07

Thermal expansivity is an important thermodynamic property and it is described mostly as a ratio between the pressure (P), volume (V) and temperature (T). This is also important in terms of thermodynamics to give an explanation about the equilibrium state of a system [3]. To measure PVA's specific thermal expansivity, the following equation is used;

$$\left(\frac{\partial v}{\partial T} \right)_p \equiv e \quad (\text{cm}^3/\text{g}^\circ\text{K}) \quad (3.1)$$

where e is the thermal expansivity, T is temperature, v is the volume, and P is the constant pressure.

The temperature coefficient of density:

$$\left(\frac{\partial \rho}{\partial T}\right)_p \equiv \rho \quad (\text{g/cm}^3\text{K}) \quad (3.2)$$

The coefficient of thermal expansion is another important parameter in heat transfer. Its accuracy is important for design, especially in microfilm production. It basically gives the fractional change in volume for a given unit change of temperature and can be given as follows:

$$\frac{1}{v} \left(\frac{\partial v}{\partial T}\right)_p \equiv \alpha \quad (^\circ\text{K}^{-1}) \quad (3.3)$$

The coefficient of thermal expansion can be used in two ways: as a volumetric thermal expansion coefficient and as a linear thermal expansion coefficient. The linear coefficient of thermal expansion is used more often. It is simply described as the fractional change in length of a bar per degree of temperature.

$$\frac{1}{L} \left(\frac{\partial L}{\partial T}\right)_p \equiv \beta \quad (^\circ\text{K}^{-1}) \quad (3.4)$$

In the present study, the PVA is provided by Sigma-Aldrich Co., MI, in the powder form. The average molecular weight is 70,000-100,000. The PVA was gradually added to the distilled water while stirring until 12-15% weight ratio was obtained. Then heating took place about 4 hours and it was let to cool down. By using a centrifugal device, the solution was rotated 5 minutes to reduce air bubbles. Another PVA, obtained from ACROS ORGANICS, was also used. It was 95% hydrolyzed with an average molecular weight of 95,000.

3.1.2. Laponite® Properties

Laponite® is a nano clay but compared to the natural clays (hectorite, bentonite...), it has much smaller dimensions (Figure 3.2). In this study, the Laponite® was provided by DH Litter Company. Normally in a Laponite® particle there are between 30000-40000 unit cells. These unit cells are combination salts of sodium, magnesium and lithium with sodium silicate. The chemical formulation of the Laponite® is;



The surface has a negative charge and the edges have small localized positive charges. Laponite® has three metal cations mostly Mg^{2+} , in a half unit cell.

Laponite® is prepared similar to the PVA in our study. Laponite® is added to the PVA solution as a ratio of 1/3 wt%. It was mixed with the PVA before dissolving it inside the distilled water. The heating time was decreased for stirring because of high surface area.

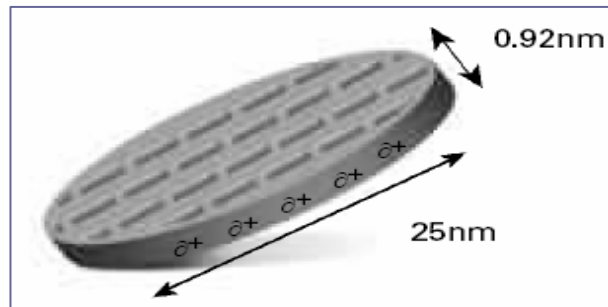


Figure 3.2. The structure of Laponite® [4].

3.2. Continuous Nano-Micro Fiber Based Yarn Manufacturing

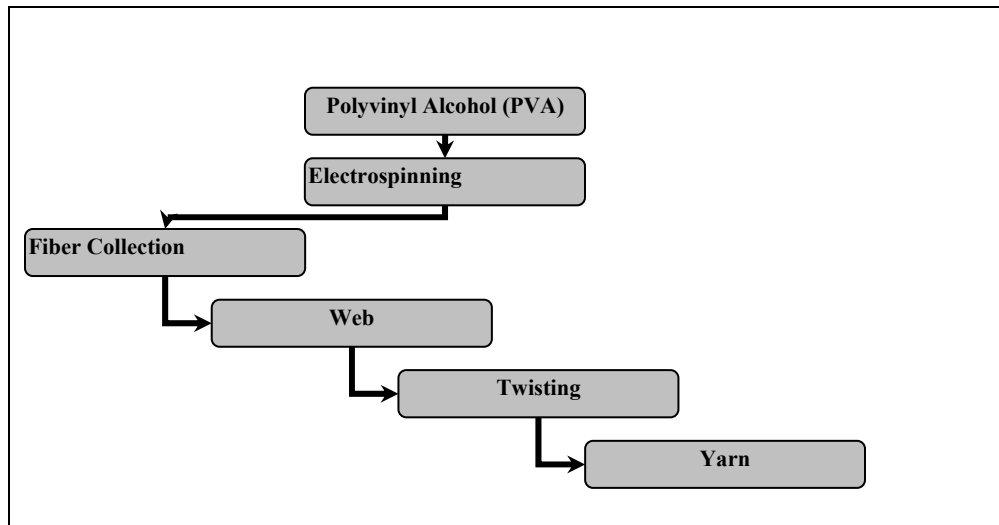


Figure 3.3. Steps for continuous nano-micro fiber based web yarn manufacturing.

Electrospinning or “electrostatic spinning” is a well known method for producing fibers with a size down to nano scale. Although it is considered to be a new method for nano scale, the electrospinning method as an idea goes back to almost 60 years. The first attempt to produce polymer filaments by using an electrostatic force was made in the 1930s by Formhals [5]. He used a polymer solution such as cellulose acetate and placed it inside the electrical field. Another milestone was achieved by Vonnegut and Neubauer in 1952 [6]. They managed to produce 0.1 mm in diameter fibers by developing a simple apparatus. They simply used a glass tube which was down to a capillary. This glass tube had a radius of a few tenths of millimeter. They filled the tube with water and the electrical wire was connected with a voltage between 5-10 kV; then they introduced the liquid inside this field. Another study was done by Simons in the field of nonwovens [7]. He managed to produce ultra thin and very light weight nonwoven by

immersing the positive charge into the solution and placing the negative charge to a belt where he collected the fibers. Electrospun acrylic fibers were produced by an apparatus of Baumgarten [8]. He managed to use a capillary tube maintained in constant size by adjusting the pump and he applied a high voltage.

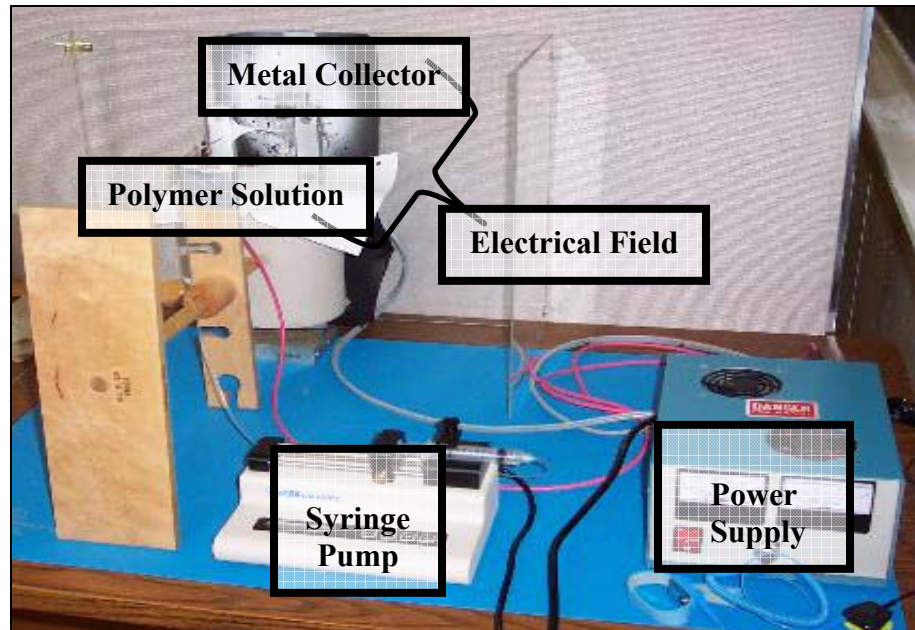


Figure 3.4 Parts of the electrospinning setup.

In the present study, the components of the electrospinning device are shown in Figure 3.4. The collector is an aluminum plate and it is placed behind the nonwoven fabric where the fibers are collected. The distance between the needle and the collector can be arranged but mostly it is kept around 30 cm which is enough for collecting the fibers. The syringe pump speed was adjusted to have a flow rate between 0.5-1 ml/h depending on solution viscosity. When the viscosity is higher, the pump speed is decreased. When the flow rate is high, big beads were observed.

It is also important to note that, electrospinning is not the only method to produce nano-micro sized fibers. There are numerous techniques to produce nano sized polymer based fibers. In Table 3.2, a short explanation of the techniques is given and compared with each other.

Table 3.2. Nanofiber manufacturing methods [9].

	Explanation and Advantages	Disadvantages
Drawing	It is almost similar to dry spinning method. It can produce very long single nanofibers one by one.	Only viscoelastic materials can be used because of the possibility of strong deformations
Template Synthesis	It uses a nanoporous membrane as a template to make nanofibers. Raw materials such as conducting polymers, metals, semiconductors and carbons can be fabricated for electronic applications	It can not be used to get one-by-one continuous nanofibers.
Phase Separation	It consists of dissolution, gelatin, and extraction using a different solvent, freezing, and drying.	It takes long time to transfer the solid polymer onto the nanoporous foam.
Self-Assembly	In this process, individual components can organize themselves into the desired aim.	It takes much time to be completed.

3.2.1. Defining the Maximum Collected Nanofiber Web Area

To find the optimum values for manufacturing, voltage, needle, distance between the collector and needle and pump values are discussed.

The applied voltage was changed between 10 kV and 20 kV. Two different needle sizes were used: 18 G 1 ½ and 22 G 1 ½. The distance between the collector and needle was also changed to get the optimum length. The distance was taken as 10 cm, 15 cm, 20 cm, 25 cm, and 30 cm from the collector. Temperature of the solution was kept at room temperature which was around 22 °C. The needle tip-target distance was investigated and it was found that it had no significant effect on electrospinning. Huang et al., suggested that a critical concentration of polymer solution has to be used to produce electrospun fibers as extensive chain entanglements are necessary to produce the fibers [9]. Table 3.3 shows the optimum parameters for electrospinning.

Table 3.3. Optimization of the experimental parameters (10% PVA water solution)

	Experiments									
	1 st	2 nd	3 rd	4 th	5 th	6 th	7 th	8 th	9 th	10 th
Voltage(kV)	20	20	20	20	15	20	20	20	20	15
Needle (G 1 ½)	18	18	18	18	18	22	22	22	22	22
Tip-needle distance (cm)	30	10	15	20	25	30	10	15	20	25
Temperature of the solution (°C)	25	24	23	22	22	22	22	22	22	22
Spinning time (min)	5	5	5	5	5	5	5	5	5	5

To investigate the dimensions of the coated area, an aluminum foil was used to cover the coated area and the solution was placed closer to the coated area. The dimensions of the foil were measured. The shape was circular with two regions: the high density area with dimensions of 115 mm (vertically) and 90 mm (horizontally). The less dense area has dimensions of 147 mm (vertically) and 147 mm (horizontally) (Figures 3.5 and 3.6).

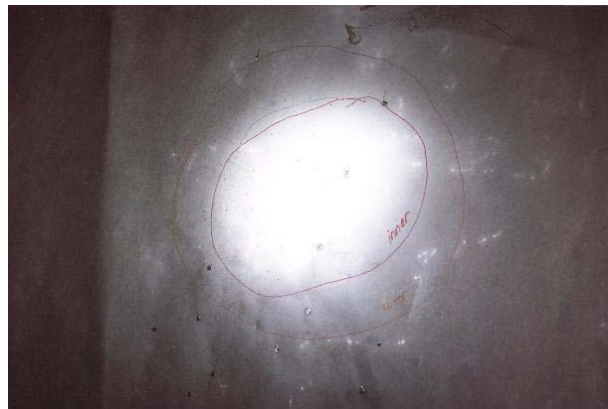


Figure 3.5 Nano-micro fiber spread area.

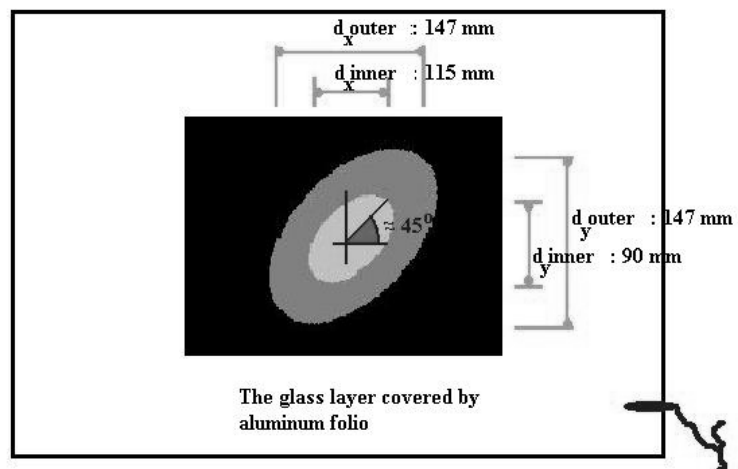


Figure 3. 6. Schematic shape of the nano-micro fiber spread area.

3.2.2. The Voltage Effect in Electrospinning

Electrospinning is a process that contains an electrical field where millimeter diameter fluid is pushed through. After introducing the fluid inside the electrical field, the Taylor cone happens at the tip of the nozzle. When the jet accelerates, it thins inside the field [9].

After many experimental studies, the most important part of the process was found out: the rapidly whipping fluid jet. The whipping of the jet to perform the spinning is so rapid; recently Hohman et al., showed that it could be captured by long exposure photograph technique [10].

Jaworek and Krupa classified the modes for the interaction of fluid and electrical field and divided them into four in a review study [11]. The first is dripping and it can be explained when Taylor cone happens; spherical droplets detach from it. The second phase is spindle mode where the jet is elongated into a thin filament. The third one is oscillating jet mode where the drops are emitted from a twisted jet. The last one is precession mode in which jet breaks into droplets, when the whipping jet is emitted from the nozzle.

It is shown by Fridrikh et al., that the fiber diameter in spinning can be controllable [12]. They presented a model to demonstrate the fluid jet inside the electrical field to find out the relationship between the fiber diameter and volume charge density. In order to do this, they changed the properties of electrospinning field such as material conductivity (K), dielectric permittivity (ϵ), dynamic viscosity (μ), surface tension (γ), density, operating characteristics (flow rate (Q), applied electrical field (E) and electric current (I)).

They found out that,

$$h_t = \left(\gamma \bar{\varepsilon} \frac{Q^2}{I^2} \frac{2}{\pi(2 \ln \chi - 3)} \right)^{1/3} \quad (3.6)$$

where h_t is the terminal diameter, Q is the flow rate, I is the electrical current, ε is the dielectric permittivity, γ is the surface tension and χ is the dimensionless wavelength of the instability. The same group also studied the stability theory to explain the relationship of the charged fluid jet inside a tangential electrical field by the function of all fluid parameters. Hohman et al., used the stability theory to develop a quantitative method to find out the starting point of electrospinning. Their theory predicts two conditions of the modes; the first emphasizes that the centerline of the jet remains straight but the jet radius is adjusted, for the second one, the reverse condition was done which involves constant centerline [13].

The schematic of the experimental device used in the present work is shown in Figure 3.7. We placed the collector not on the ground but on the wall. The reason was to reduce the beading effect.

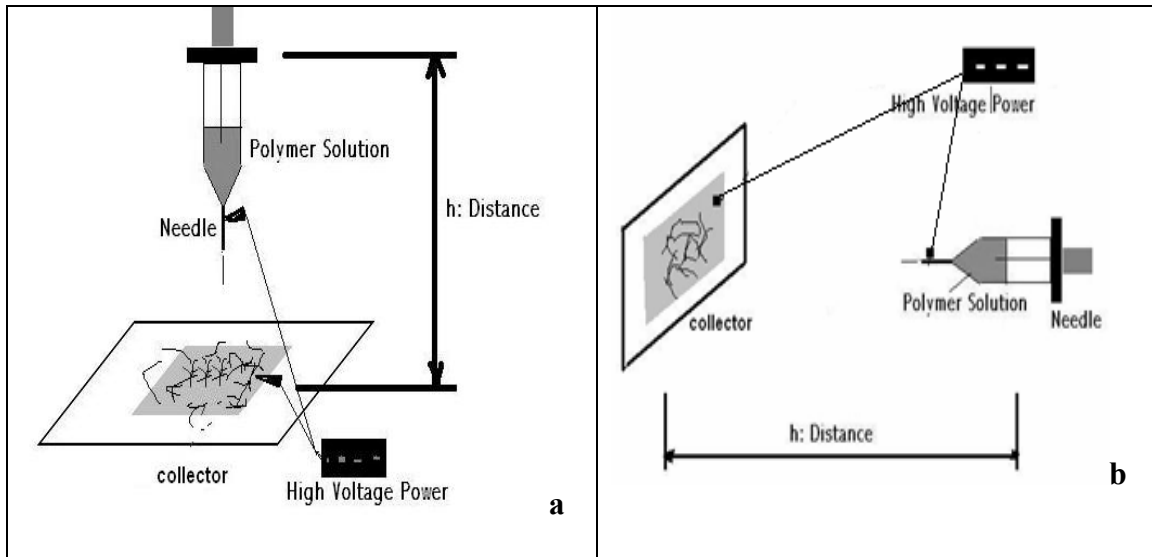


Figure 3.7. Direction of electrospinning a) The set-up of Hofman [13], b) The experimental set-up used in the present work.

Another important property is the voltage effect. When the applied voltage is less than 15 kV, it was seen that there is no spinning inside the electrical field, mostly because of the surface tension of the polymer. The electrical force is not enough to overcome the surface tension of the polymer. When the applied voltage is 15 kV and higher, the spinning starts.

The effect of voltage over polymer solution is summarized in Figures 3.8, 3.9 and 3.10. When the voltage is increased, the spinning starts earlier. Also it was observed that, the electric field strength increase the electrostatic repulsive force on the fluid jet and this causes thinner fiber formation.

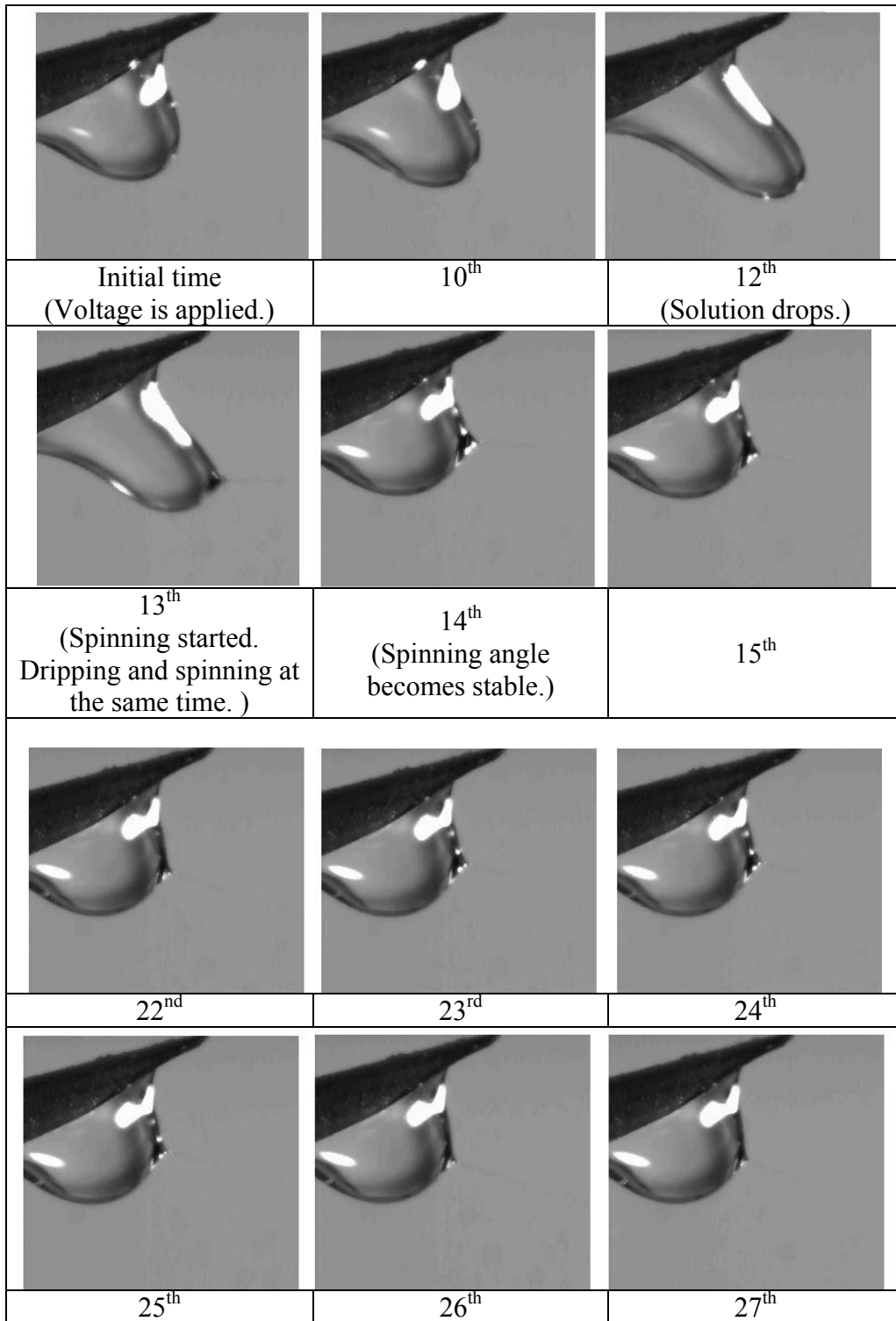


Figure 3.8. Electrospinning with 15 kV.

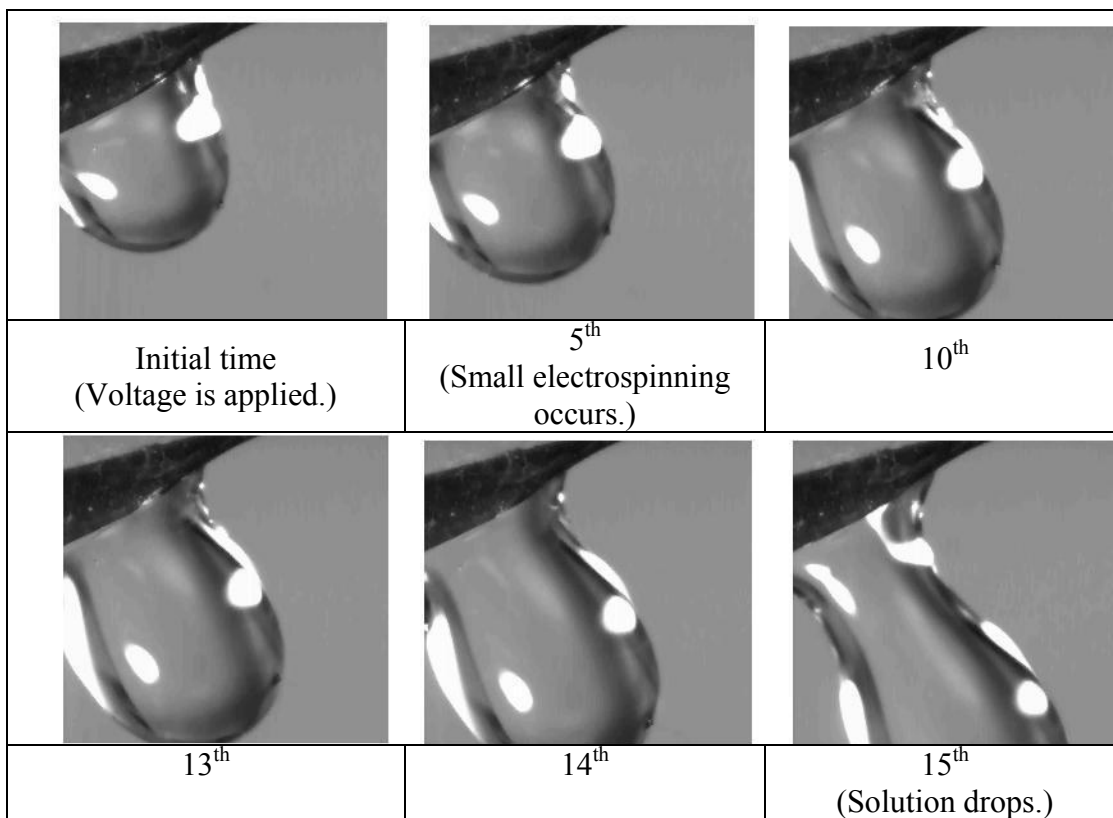


Figure 3.9. Electrospinning with 17.5 kV.

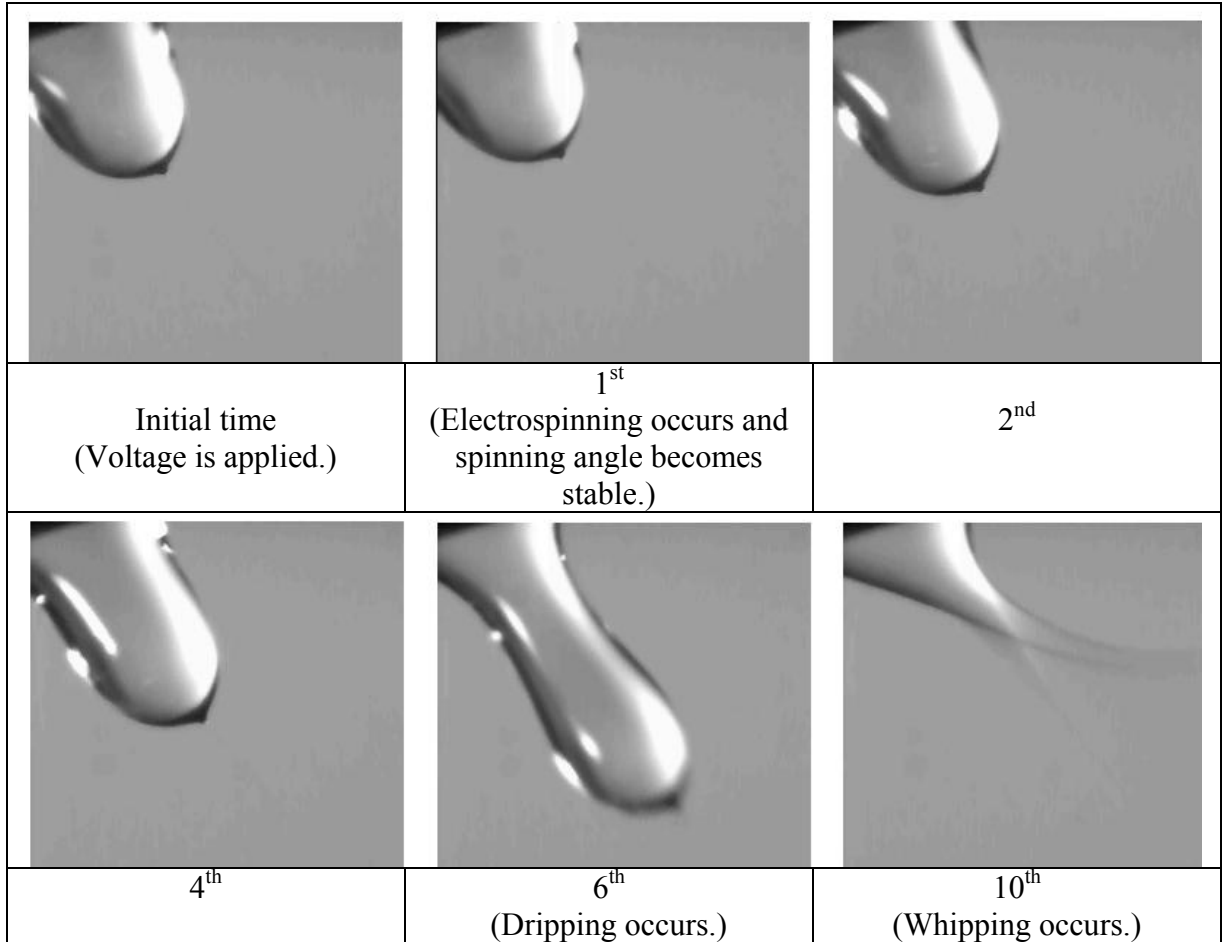


Figure 3.10. Electrospinning with 20 kV.

The polymer drop is balanced by upward and downward forces. These forces are simply classified into two groups: electrical forces and non-electrical forces. The electrical and gravitational forces (F_{grav}) are downward and the rheological (F_{rheo}), inertial (F_{in}), surface tension (F_{surf}) and aerodynamics forces (F_{aero}) act upward, as shown in Figure 3.11 [14]. The dominant electrical force (F_{elec}) is described as:

$$F_{elec}(F) = F_{rheo}(A) + F_{in}(B) + F_{surf}(C) + F_{aero}(D) - F_{grav}(E) \quad (3.7)$$

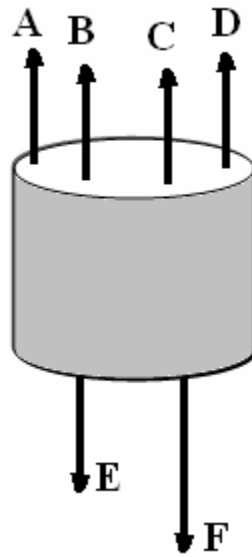


Figure 3.11. Forces acting on polymer solution [14].

In the experimental study, when the first fiber formation occurred, the direction of the spinning was captured and the spinning angle was determined. For the applied 15 kV voltage value, the spinning angle was found between -7° , and -10° ; and for 17.5 kV, it was observed that the angle is around -30° and for 20 kV the spinning angle is around 45° . After these observations, equation (3.7) can be transformed into;

$$F_{\text{elec}} = f(\phi) \quad (3.8)$$

where ϕ is the spinning angle and it has a relationship with the voltage. If it is assumed that;

$$V(15 \text{ kV}) \sim \phi (\pi/18)$$

$$V(17.5 \text{ kV}) \sim \phi (\pi/6)$$

$$V(20 \text{ kV}) \sim \phi (\pi/4)$$

and when these values are plotted in Excel, Figure 3.12 is obtained.

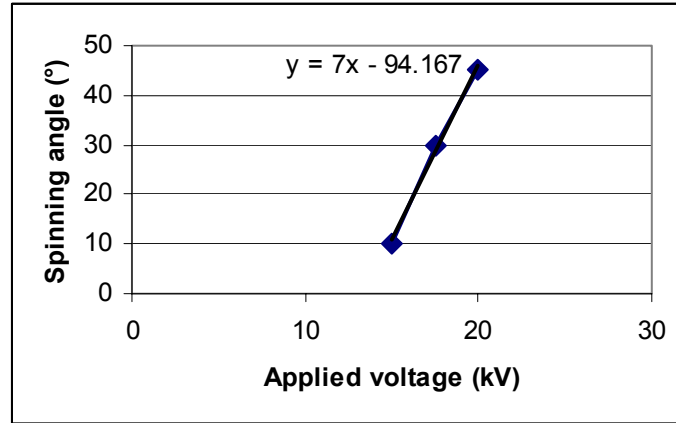


Figure 3.12. Applied voltage effect on the spinning angle.

From the graph, the empirical relationship between the voltage and spinning angle is obtained as;

$$Y=7x-94.167 \quad (3.9)$$

where x is the applied voltage and Y is the spinning angle (°)

So the equation 3.9 can be written as;

$$F_{elec} = f(7*[V]-94.167) \quad (3.10)$$

The observed relationships can be seen in Figure 3.13.

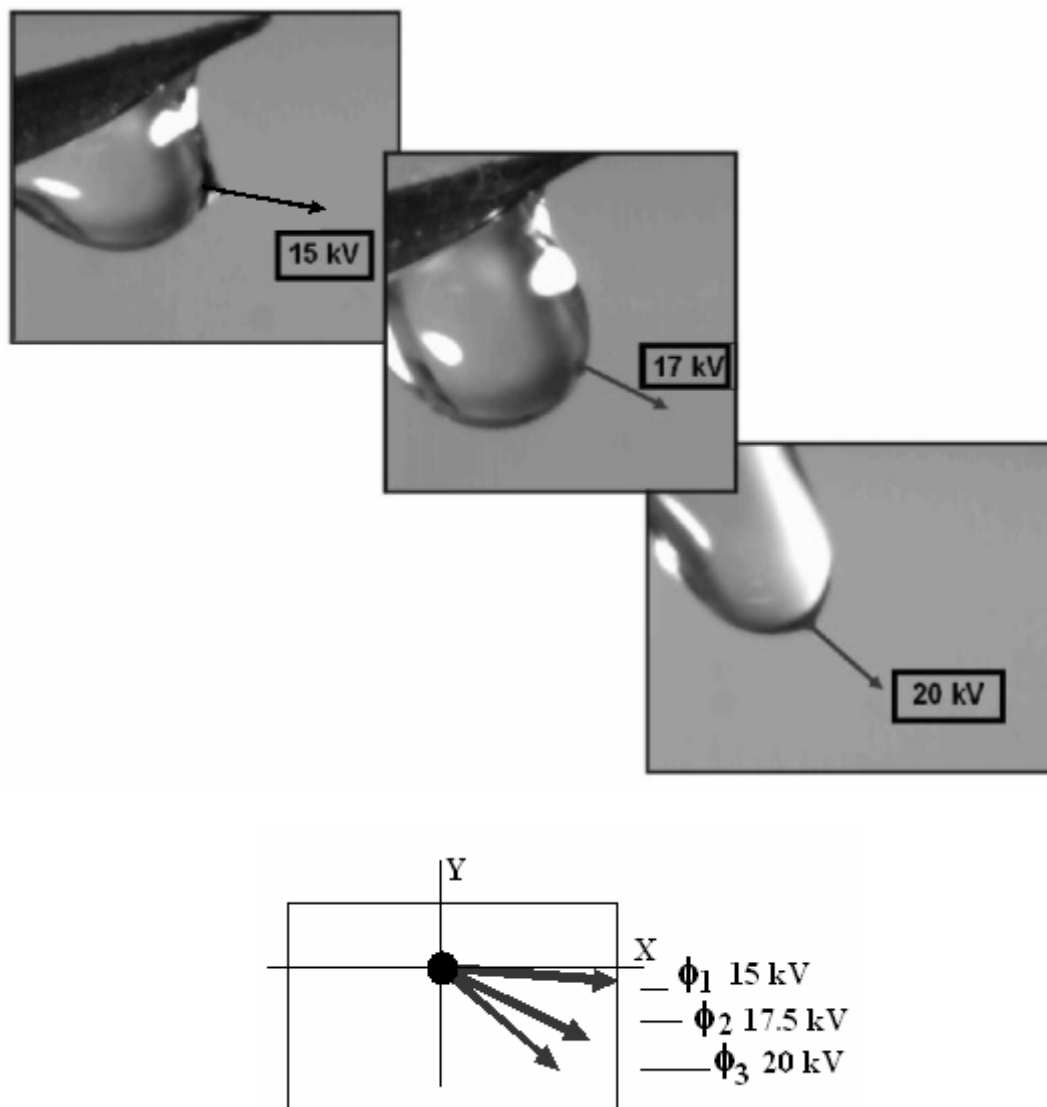


Figure 3.13. Electrospinning directions for 15, 17.5 and 20 kV applied voltage values.

3.2.3. Scanning Electron Microscope (SEM) Imaging

Before putting the dried sample under SEM (EMS 550X in Biology Department of Auburn University), it was covered with Au using EMS 550X Sputter Coating Device. Argon gas was applied to start the Au coating process. Since the coated sample is a polymer, the coating time was increased to 4 minutes in order not to have melting problem under the SEM.

The voltage level was adjusted to 10 kV and was kept the same for all the samples. The SEM images of the PVA samples can be seen in Figure 3.14.

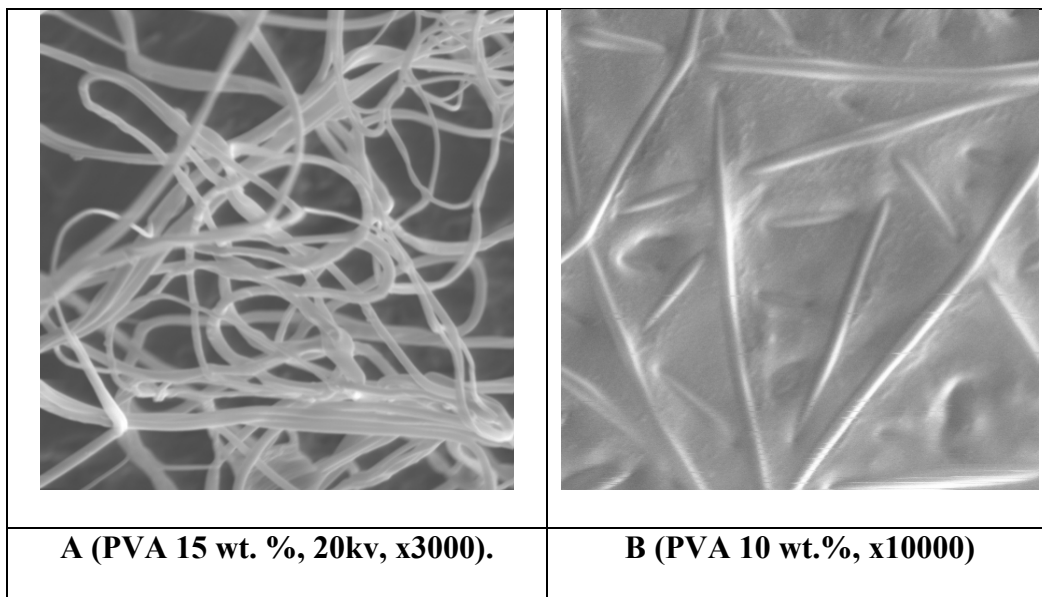


Figure 3.14. Image of the PVA fiber samples

3.2.4. Continuous Manufacturing Device

The continuous nanofiber based yarn manufacturing is a challenge. The electrical field needs to be somewhat controlled. Optimum viscosity of the solution must be used. Ko et al., combined the electrospinning method and conventional yarn manufacturing (Figure 3.15).

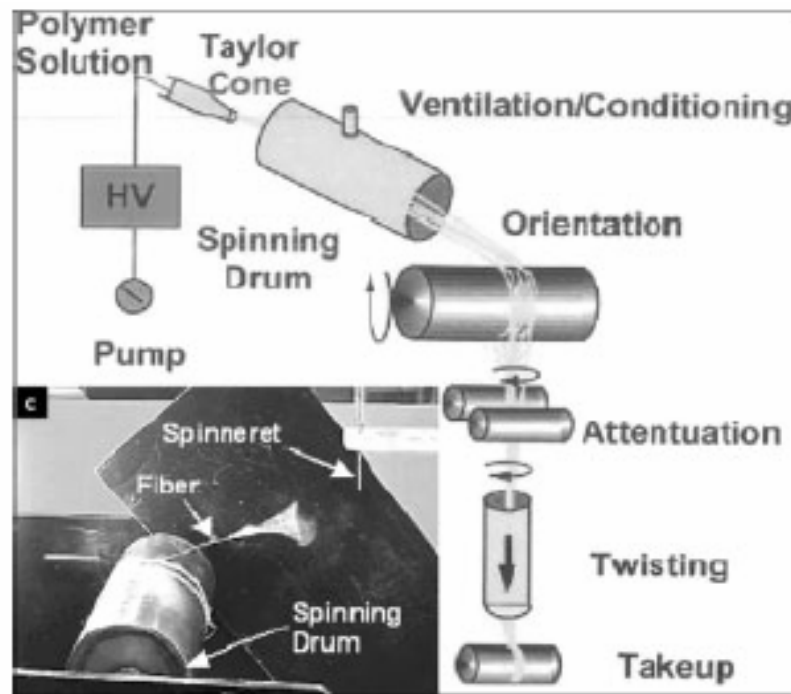


Figure 3.15. Schematic of the continuous yarn spinning made by SQNT-filled composite [15].

We designed a nanofiber web collecting mechanism which is shown in Figure 3.16. It was found that, by using the optimum properties of electrospinning and having an appropriate environment for the electrospun fibers, they could be easily pulled from the collected surface and can be made into a yarn in a continuous manufacturing process.

Parts of the device are:

- Nonwoven fabric covered cylinder.
- Basic electrospinning device
 - Needle and syringe
 - Power supply
 - Syringe pump for giving stable solution flow.
- Pulling mechanism which forwards the gathered nanofiber web to the next process.
- Nonwoven fabric covered cylinder which is made of aluminum; this part must be attached to the main collector to gather the nanofibers.
- Power unit to provide the desired movement for both cylinder and pulling mechanism.

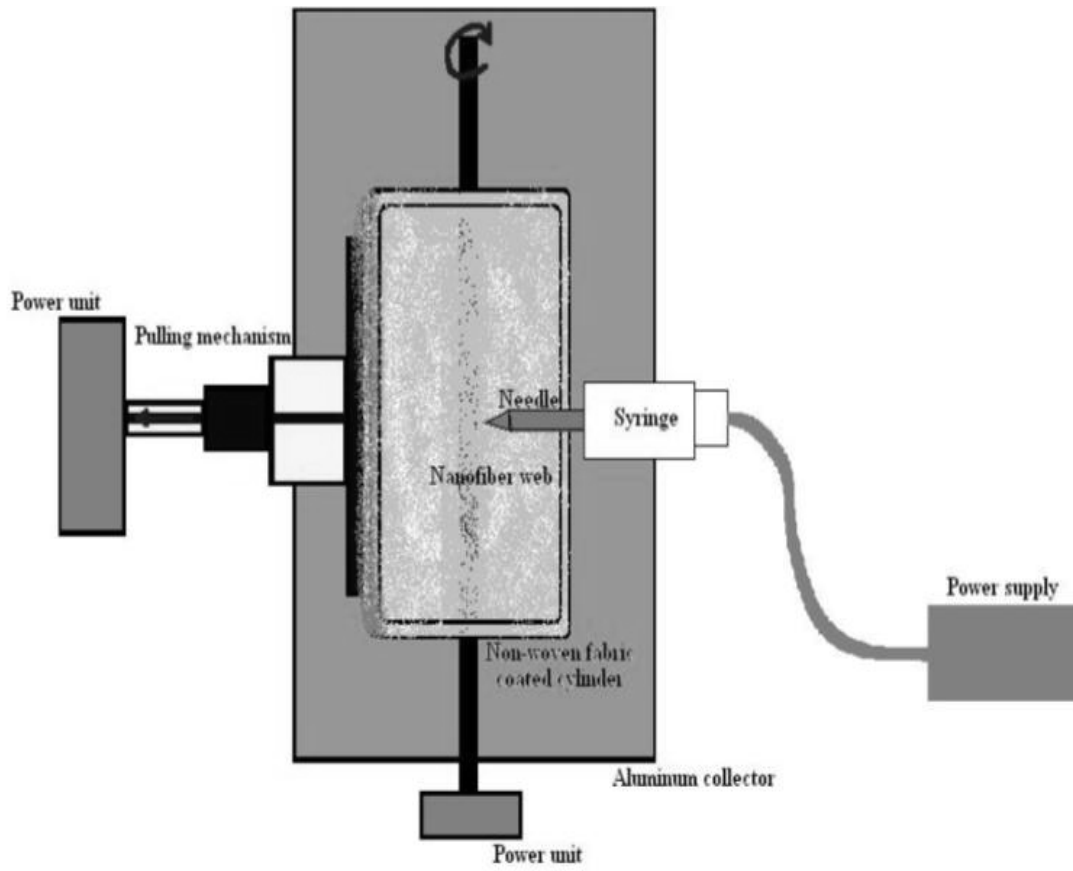


Figure 3.16. Schematic of yarn manufacturing device

After producing the nano-micro fiber based yarn, tensile strength measurements were done. We used Instron tensile testing device to measure the elongation and maximum force to break the nano-micro fiber based yarn. Tensile stress is measured as the force required to rupture a fiber with a unit of force/linear density. There are some factors which affect fiber strength: the molecular length, orientation, intermolecular forces and degree of crystallinity. When the area under the stress strain curve is bigger, the breaking energy is maximized.

3.2.5. Coating

Nanofibers have interesting properties which is the result of their extremely high surface to weight ratio compared to the other conventional fibrous structures. This makes these fibers ideal to be used in application areas such as filtration because of high pore volume, tight pore size, etc. Recently, in protective clothing, electrospun fiber webs have been used.

In this study, the fibers are collected on different kind of fabric surfaces and the best fabric was chosen to pull the web form easily. As seen in Figure 3.17, paper, woven, and nonwoven fabrics were used for coating.

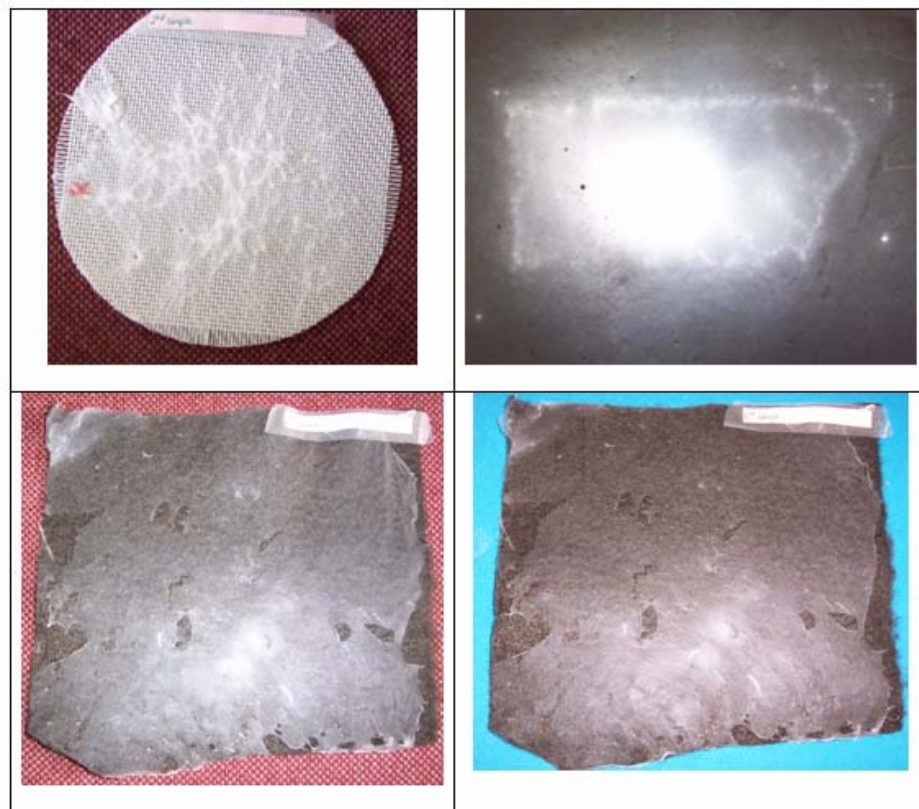


Figure 3.17. Coated fabrics.

The coating time differed from one hour to two hours. When the coating was done over a nonwoven fabric, the nanofibers were seen in the form of web rather than film.

3.2.6. Twisting of Manufactured Nano-micro Fibers

After getting the fibers in a web form, the fibers were gently pulled and twisted by hand since the web form is so sensitive. Making a yarn will help to handle the fibers easily.

Figure 3.18 shows the twisting process. It is important to note that, Since PVA can be sticky, twisting is done effectively.

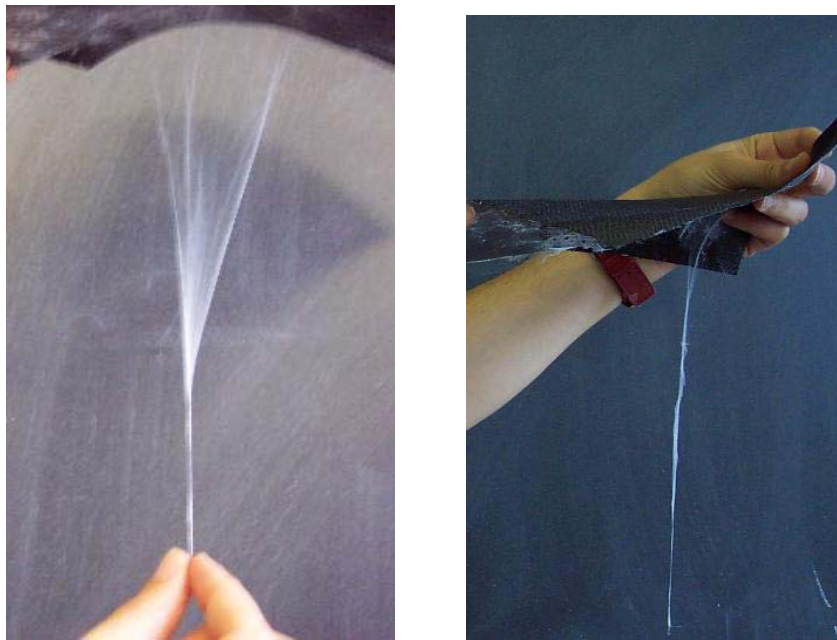


Figure 3.18. Twisting of nano fiber based web.

3.2.7. Differential Scanning Calorimetry (DSC) Studies

In normal conditions, in the melting region there are two processes that require energy; heat capacity and heat of fusion. Anything which melts very rapidly (faster than the modulation) will resolve the heat of the fusion into a nonreversing heat flow. In general, a slower heating rate allows for more cycles in the melting region. Distributing the heat of fusion over many cycles effectively decreases the amplitude of each cycle. This decrease in amplitude leads to a decrease in reversing of the heat flow at the melt as shown in Figure 3.19 [16].

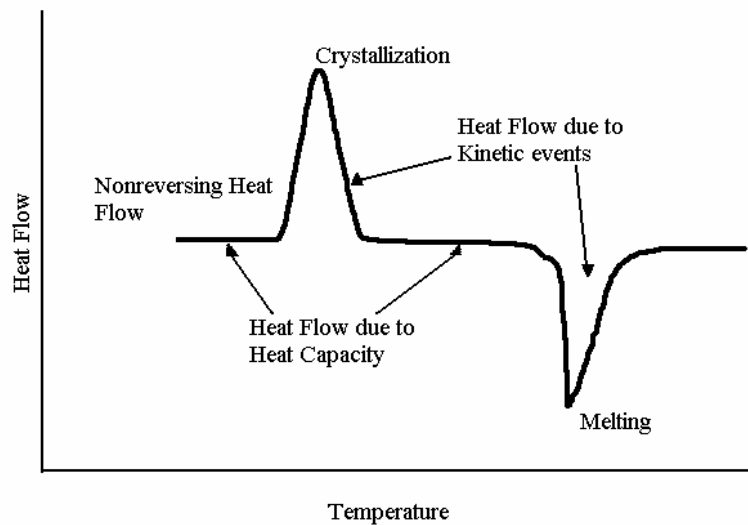


Figure 3.19. Heat flow and temperature relationship in DSC [16].

Increasing the sample mass increases the temperature gradient in the sample and it increases the time for heat transfer to occur. This translates to less melting in-phase with the temperature modulation.

3.2.8. Air Permeability Measurements

Air permeability is a term to describe the breathability of the fabrics for various purposes such as industrial filter fabrics, tents, medical fabrics, etc. [17]. To determine the air permeability of micro-nano structures, air permeability test apparatus was used. The most commonly used methods for air permeability in the literature are ENISO 9237 and AS 2001.2.34.

The area of the orifice is;

$$A_{\text{orifice}} = 2.54 * 10^{-6} \text{ m}^2.$$

The air permeability is calculated by using the measured penetration time:

$$\text{Air permeability} = \frac{\text{Volume difference based on applied pressure (m}^3\text{)}}{\text{Penetration time (min ute)/The area of the orifice (m}^2\text{)}} \quad (3.11)$$

$$\text{Air permeability} = \frac{0.0003 \text{ m}^3 * 2.54 * 10^{-6} \text{ m}^2}{46.4 \text{ sec} * \frac{1 \text{ min}}{60 \text{ sec}}} = 9.86 * 10^{-6} \frac{\text{m}^3}{\text{min/m}^2} \quad (3.12)$$

3.2.9. Dynamic Contact Analyzer

In our study, surface tensions of the PVA and PVA+Laponite® based solutions were measured. Laponite was taken as a ratio of 5% of the PVA solvent. It means that for 12% PVA, the Laponite® is 5% of this PVA. The total weight of the solution was 100 gr.

3.2.10. Thermal Conductivity Measurement

Thermal conductivity can be measured by various experimental ways such as DSC method or air permeability measurements.

a) By MDSC (Modified Differential Scanning Calorimetry) Method

In MDSC (almost similar to DSC), the magnitude of the measured kinetic heat flow is a function of time at constant temperature which is the working procedure of it.

The general theory can be written as;

$$\frac{dQ}{dt} = C_p \frac{dT}{dt} + f(T, t) \quad (3.13)$$

where Q is the heat flux, C_p is the heat capacity, T is the temperature, and t is the time.

Total Heat Flow (DSC) = Heat Capacity Components + Kinetic Component

= Heating Rate Dependent + Time Dependent

= MDSC Reversing + MDSC Non-reversing

Reversing heat flow contains:

- Glass Transition
- Melting (most)

Non-reversing heat flow:

- Enthalpy relaxation
- Evaporation
- Crystallization
- Decomposition
- Cure

- Melting (some)

The values can be summarized in Table 3.4.

Table 3.4. Effects on DSC graph areas.

	Amplitude	Period	Heating Rate	Sample Mass
Change	+	-	-	+
Reversing area in the melt	-	-	-	-
Nonreversing area in the melt	+	+	+	+

(+): Increasing (-): Decreasing

In thermal conductivity measurement two specimens are used: one thin (0.4 mm) and one thick (3 mm). The thin sample is encapsulated in a standard aluminum pan to measure the specific heat capacity. The thick sample is used to measure the apparent heat capacity without a pan [16].

$$K^0 = \frac{8LC^2}{C_p M d^2 P} \quad (3.14)$$

where;

K^0 ; Uncorrected thermal conductivity (W/M°C)

L; Sample length (mm)

C; Apparent heat capacity (mJ/°C)

C_p ; Specific heat capacity (J/g°C)

M; Thick sample mass (mg)

d; Thick sample diameter (mm)

P; Period of measurement (sec)

b) By Air Permeability Test

It is known that, by using air permeability test, thermal conductivity can be calculated based on Darcy's permeability equation. This method depends on the relationship between Darcy's permeability equation and Fourier's thermal conductivity equation. Based on this, thermal conductivity can be predicted easier compared to the other methods [18].

Basically, by using the following two equations;

$$q_{fp} = k_{fp} \frac{\Delta P}{L} \quad (3.15)$$

and

$$q_{tc} = k_{etc} \frac{\Delta T}{L} \quad (3.16)$$

where,

q_{fp} ; linear flow rate

k_{fp} ; air flow permeability,

ΔP ; pressure drop

L ; sample thickness

q_{tc} ; flow rate from Fourier's law

k_e ; effective thermal conductivity

ΔT ; temperature differential

The effective thermal conductivity can be obtained as;

$$k_{\text{etc}} = \frac{k_{\text{fp}}(\Delta P)q_{\text{tc}}}{(\Delta T)q_{\text{fp}}} \quad (3.17)$$

3.3. References

1. <http://composite.about.com/library/glossary/p/bldef-p4165.htm>. (accessed in April 2005).
2. Broughton, R. M., TXEN 6310 Lecture Notes, Auburn University, Spring 2004.
3. Van Krevelen, D.W., "*Properties of Polymers Correlations with Chemical Structure*", Elsevier Publishing Company, **1972**, 2.
4. www.laponite.com (accessed in Jan 2005).
5. Formhals, A., "Process and Apparatus for Preparing Artificial Threads", US Patent 1,975,504, **1934**.
6. Vonnegut, B., and Neubauer, R., "Production of Monodisperse Liquid Particles by Electrical Atomization", J. of Colloid Science, **1952**, 7, 616-622.
7. Simons, H. L., "Process and Apparatus for Producing Patterned Non-woven Fabrics", US patent 3,280229, **1966**.
8. Baumgarten PK., "Electrostatic Spinning of Acrylic Microfibers", J of Colloid and Interface Science, **1971**, 36, 71-9.
9. Huang Z. M., Zhang, Y. Z., Kotaki, M., and Ramakrishna, S., "A Review on Polymer Nanofibers by Electrospinning and Their Applications in Nanocomposites", Comp. Sci. and Techn., **2003**, 63, 2223-2253.

10. Hohman, M. M., Shin, M., Rutledge, G., and Brenner, M. P., “*Electrospinning and Electrically Forced Jets. I. Stability Theory*”, *Physics of Fluids*, **2001**, 13, 2201-2221.
11. Jaworek, A., and Krupa, A., “*Classification of the Modes of End Spraying*”, *J. Aerosol Sci.*, **1999**, 30(5), 873.
12. Fridrikh, S. V., Yu, J., Brenner, M., and Rutledge, G., “*Controlling the Fiber Diameter during Electrospinning*”, *Physical Review Letters*, **2003**, 90(14), 144502.
13. Hohman M., Shin, M., Brenner, M., and Rutledge, G., “*Electrospinning and Electrically Forced Jets. II. Applications*”, *Physical Fluids* **2001**, 13(8), 2201-2220.
14. <http://www.gpi-test.com/4110.htm>. (accessed in Nov. 2004)
15. Ko, F., Gogotsi, Y., Ali, A., Naguib, N., Ye, H., Yang, G., Li, C., and Willis, P., “*Electrospinning of Continuous Carbon Nanotube-filled Nanofiber Yarns*”, *Adv. Mater.* **2003**, 15(14), 1161-1165.
16. TA Instruments, “DSC Operator’s Manual”, July 1998.
17. Pamela Banks-Lee and Mohammadi, M., “*Utilization of Air Permeability in Predicting the Thermal Conductivity*”, *International Nonwoven Journal*, **2004**, 13(2), 28-33.
18. http://www.inda.org/subscrip/inj04_2/p28-33-banks.pdf (accessed in Nov. 2004)

CHAPTER 4

ANALYTICAL MODELING OF FILLER FIBER REINFORCED COMPOSITES

Nomenclatures:

K	Thermal conductivity
L	Length
Q	Heat flow rate
R	Thermal resistance
T	Temperature
V	Volume fraction
T	Thickness of the interface (barrier)
A	Radius of barrier with filler radius
R	Radius

Subscripts:

T	Total
B	Barrier
e	Effective
f	Main fiber
d	Filler fiber
-	(bar) Dimensionless
^	(hat) Without barrier

Greeks:

β	Thermal conductivity ratio between the filler fiber and the main fiber = k_d/k_f
γ	Thermal conductivity ratio between the barrier and the main fiber = k_b/k_f

Fiber-reinforced composites have had significant importance for a long time. Many experimental, theoretical and numerical studies have been carried out by various research groups in the universities and the industry.

In general, in a composite, there are three different types of components having different fundamental properties. Figure 4.1 shows the basic components of the composite, which are matrix, interface and filler fiber, used in the model.

In this study, the composites are assumed to have not only rectangular shape but also the cylindrical shape. In order to solve the problem which is shown in Figure 4.1, the hexagonal unit cell was developed and analyzed to find the effective thermal conductivity.

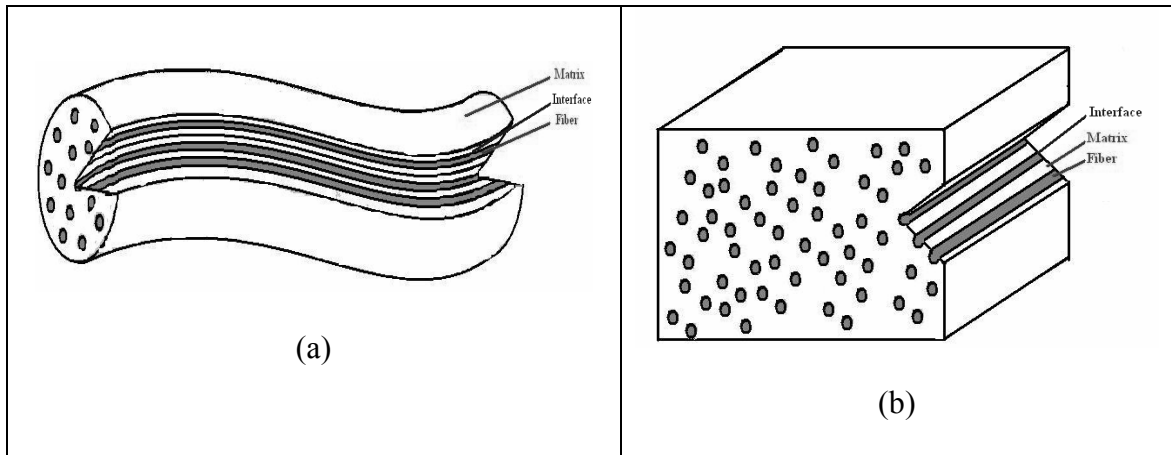


Figure 4.1. Composite structures for the model. a) Cylindrical shape b) Rectangular shape

4.1. Description of the Problem

Based on the analytical calculation of Zou et al., the hexagonal unit cell was developed and analyzed analytically [1]. The applied procedure depends on the thermal-electrical analogy method which has been widely used in different kind of problems.

The problem consists of two real and one imaginary component. Imaginary part is the thermal barrier part and compared to the filler size, it has much smaller size. The real parts are the main fiber as a matrix and filler fiber.

In the present model, a hexagonal unit cell is developed as shown in Figure 4.2. Because of the continuous behavior, it is assumed that, 2-D modeling is sufficient to represent the behavior of the structure.

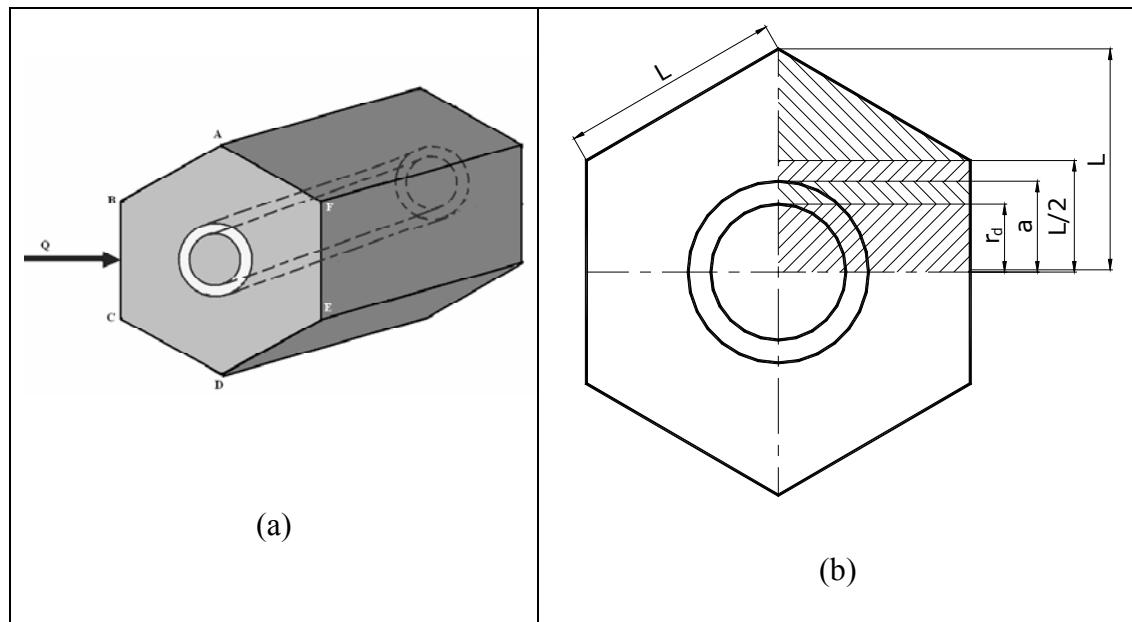


Figure 4.2. Hexagonal model for transverse heat conduction. a) 3-D model b) 2-D model. (Q : heat flux.)

The cross-section of the hexagonal unit cell was partitioned into regions and the thermal resistance method was applied to each region. For total thermal resistance, it is considered that these regions are connected parallel.

$$\frac{1}{R_t} = \left[\frac{1}{R_{1a}} + \frac{1}{R_2} + \frac{1}{R_3} + \frac{1}{R_4} \right] \quad (4.1)$$

where R_t is the total thermal resistance of the composite.

R_{1a} , R_2 , R_3 , R_4 : The thermal resistance of the first, second, third and fourth regions, respectively (Figure 4.3).

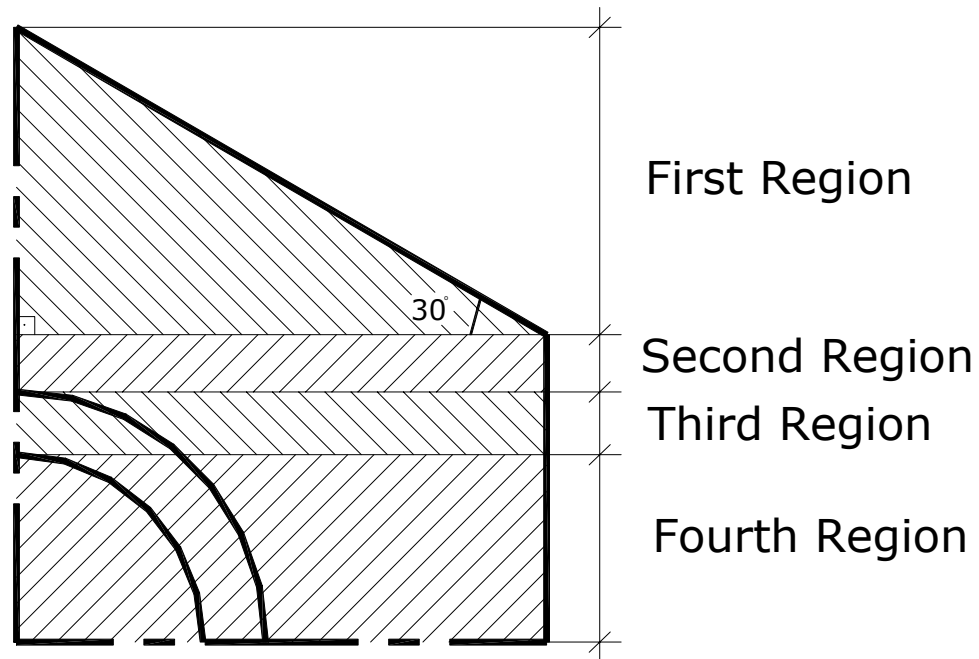


Figure 4.3. Symmetric part of the hexagonal model and the region divisions.

The thermal characteristics of the components are:

k_f : thermal conductivity of main fiber,

k_d : thermal conductivity of filler fiber,

k_b : thermal conductivity of barrier,

The assumptions for the modeling are;

- a) Because of the continuity, the modeling is done in 2-D.
- b) Filler fibers are embedded in a homogenous matrix
- c) Filler fibers have cylindrical shape and have a radius of r_d ; the barrier interface thickness is taken as “t” which is equal to “a- r_d ” where a is the distance of barrier boundary from the center. The length of each side of the hexagonal unit cell is taken as “L”.
- d) Temperature difference was applied only to the left and right sides, -1 °C and 1 °C, respectively.
- e) The volume fraction of the filler fibers inside the matrix is taken between 10-30%. The distribution of the filler fibers is considered to be uniform and parallel.
- f) The thermal contact resistance is negligible depending on the existence of thermal barrier layer.
- g) The composite is considered without any cracks; it is considered not to have voids.

4.2. Modeling for Analytical Thermal Resistance

To investigate the total thermal resistance behavior of the proposed composite with respect to the change of variable k_f/k_d , the symmetric part of the whole hexagonal

area, which is shown in Figure 4.3, is considered. In this case, the total thermal resistance of the designated part is obtained as,

$$\frac{1}{R_{t_f}} = \sqrt{3} k_f \quad (4.2)$$

Then, by dividing equation (4.1) by equation (4.2), dimensionless total thermal resistance of the composite (\bar{R}_t) is given as

$$\frac{1}{\bar{R}_t} = \frac{\frac{1}{R_{1a}} + \frac{1}{R_2} + \frac{1}{R_3} + \frac{1}{R_4}}{\sqrt{3} k_f} \quad (4.3)$$

4.2.1. Thermal Resistance of the First Region, R_{1a}

The first region consists of only the main fiber component. Thermal resistance of the 1st part is calculated by considering that, it is half of a rectangle (Figure 4.4.)

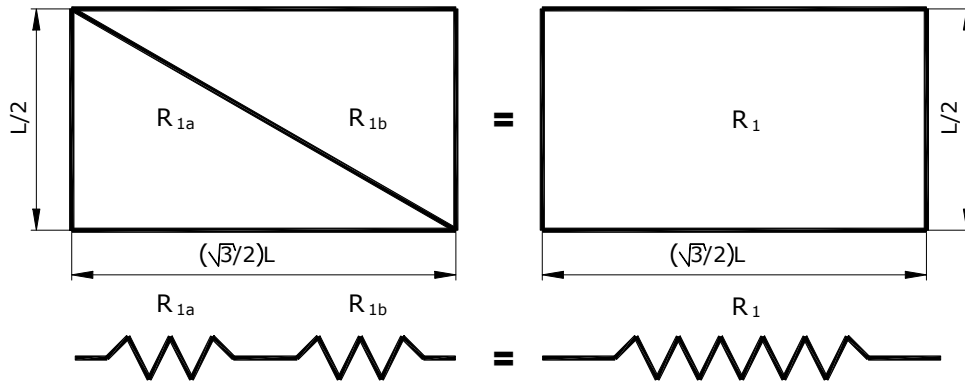


Figure 4.4. The first region.

As a result, the value of R_{1a} is half of R_1 which results in the following equation.

$$R_{1a} = \frac{\frac{\sqrt{3}}{2}L}{2k_f \frac{L}{2}} = \frac{\sqrt{3}}{2k_f}$$

$$\frac{1}{R_{1a}} = \frac{2k_f}{\sqrt{3}} \quad (4.4)$$

4.2.2. Thermal Resistance of the Second Region, R_2

Thermal resistance of this region can be written as;

$$\frac{1}{R_2} = \frac{k_f \left(\frac{L}{2} - a \right)}{\frac{\sqrt{3}}{2}L} \quad (4.5)$$

4.2.3. Thermal Resistance of the Third Region, R_3

The third region is the combination of the main fiber and the barrier region (Figure 4.5.).

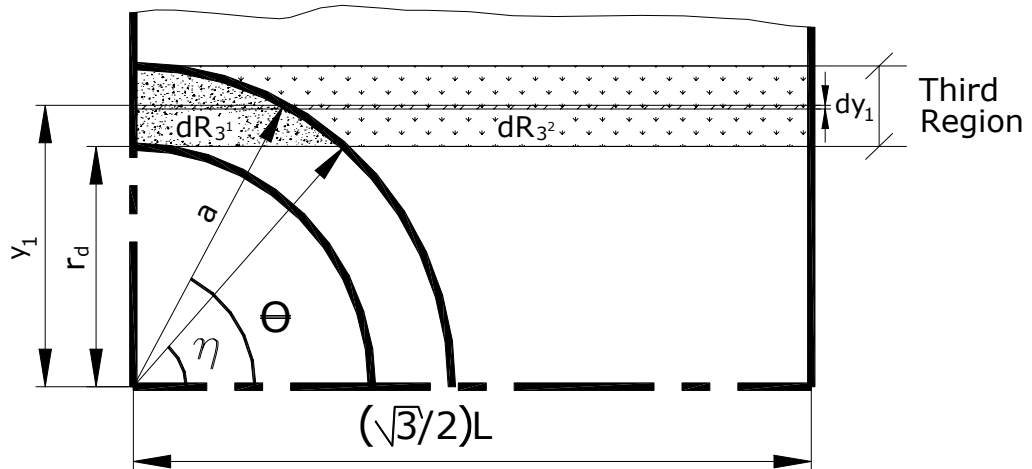


Figure 4.5. Schematic of the third region.

The 3rd part was divided into infinite divisions and

$$dR_3 = dR_{3^1} + dR_{3^2} = \frac{a \cos \theta}{k_b dy_1} + \frac{\left(\frac{\sqrt{3}}{2} L - a \cos \theta \right)}{k_f dy_1}$$

$$dR_3 = \frac{a k_f \cos \theta + \left(\frac{\sqrt{3}}{2} L - a \cos \theta \right) k_b}{k_b k_f dy_1} \quad (4.6)$$

where;

$$y_1 = a \sin \theta$$

$$dy_1 = a \cos \theta d\theta \quad (4.7)$$

After putting the forms inside the equation (4.6), we get;

$$\frac{1}{dR_3} = \frac{k_b k_f a \cos \theta d\theta}{a k_f \cos \theta + \left(\frac{\sqrt{3}}{2} L - a \cos \theta \right) k_b} \quad (4.8)$$

Before solving the above equation, it is assumed that;

$$b = \frac{\sqrt{3}}{2} \frac{L}{a}$$

$$\gamma = \frac{k_b}{k_f} \quad (4.9)$$

$$c = \frac{(1-\gamma)}{\gamma}$$

Then the equation 4.8 becomes;

$$\begin{aligned}\frac{1}{R_3} &= \int_{\eta}^{\frac{\pi}{2}} \frac{k_f \gamma \cos \theta d\theta}{\cos \theta + \gamma [b - \cos \theta]} = \int_{\eta}^{\frac{\pi}{2}} \frac{k_f \gamma d\theta}{1 + \gamma [b \sec \theta - 1]} \\ &= \int_{\eta}^{\frac{\pi}{2}} \frac{k_f \gamma d\theta}{(1 - \gamma) + b \gamma \sec \theta} = \int_{\eta}^{\frac{\pi}{2}} \frac{k_f d\theta}{\frac{(1 - \gamma)}{\gamma} + \frac{1}{\gamma} b \gamma \sec \theta}\end{aligned}$$

$$\frac{1}{R_3} = \int_{\eta}^{\frac{\pi}{2}} \frac{k_f d\theta}{c + b \sec \theta} \quad (4.10)$$

After integrating the right side of the above equation;

$$\frac{1}{R_3} = \left(\frac{\pi}{2} - \eta \right) \frac{k_f}{c} - \frac{b k_f}{c} \int_{\eta}^{\frac{\pi}{2}} \frac{d\theta}{b + c \cos \theta} \quad (4.11)$$

where;

θ is varying from η to 90° such that

$$\sin \eta = \frac{r_d}{a} \text{ and therefore } \eta = \sin^{-1} \frac{r_d}{a} \quad (4.12)$$

The solution of the integral depends on b and c ; the first option is if $b^2 > c^2$ and the other option is if $c^2 > b^2$ [2-4]. Then, the solution for the third region becomes as follows:

$$(*) \ b^2 > c^2 \Rightarrow$$

$$\frac{1}{R_3} = \left(\frac{\pi}{2} - \eta \right) \frac{k_f}{c} - \frac{2b k_f}{c \sqrt{b^2 - c^2}} \left[\tan^{-1} \left(\sqrt{\frac{b-c}{b+c}} \tan \frac{\pi}{4} \right) - \tan^{-1} \left(\sqrt{\frac{b-c}{b+c}} \tan \frac{\eta}{2} \right) \right]$$

$$\frac{1}{R_3} = \left(\frac{\pi}{2} - \eta\right) \frac{k_f}{c} - \frac{2bk_f}{c\sqrt{b^2 - c^2}} \left[\tan^{-1} \sqrt{\frac{b-c}{b+c}} - \tan^{-1} \left(\sqrt{\frac{b-c}{b+c}} \tan \frac{\eta}{2} \right) \right] \quad (4.13)$$

$$(**) b^2 < c^2 \Rightarrow$$

$$\frac{1}{R_3} = \left(\frac{\pi}{2} - \eta\right) \frac{k_f}{c} - \frac{bk_f}{c\sqrt{c^2 - b^2}} \left[\ln \left(\frac{\sqrt{\frac{c+b}{c-b}} + \tan \frac{\pi}{4}}{\sqrt{\frac{c+b}{c-b}} - \tan \frac{\pi}{4}} \right) - \ln \left(\frac{\sqrt{\frac{c+b}{c-b}} + \tan \frac{\eta}{2}}{\sqrt{\frac{c+b}{c-b}} - \tan \frac{\eta}{2}} \right) \right] \quad (4.14)$$

as a next step, when $\tan(\pi/4)$ is equal to 1;

$$\frac{1}{R_3} = \left(\frac{\pi}{2} - \eta\right) \frac{k_f}{c} - \frac{bk_f}{c\sqrt{c^2 - b^2}} \left[\ln \left(\frac{\sqrt{\frac{c+b}{c-b}} + 1}{\sqrt{\frac{c+b}{c-b}} - 1} \right) - \ln \left(\frac{\sqrt{\frac{c+b}{c-b}} + \tan \frac{\eta}{2}}{\sqrt{\frac{c+b}{c-b}} - \tan \frac{\eta}{2}} \right) \right] \quad (4.15)$$

The rest of the solution steps for the third region are as follows;

$$\frac{1}{R_3} = \left(\frac{\pi}{2} - \eta\right) \frac{k_f}{c} - \frac{bk_f}{c\sqrt{c^2 - b^2}} \left[\ln \left(\frac{\frac{\sqrt{c+b} + \sqrt{c-b}}{\sqrt{c-b}}}{\frac{\sqrt{c+b} - \sqrt{c-b}}{\sqrt{c-b}}} \right) - \ln \left(\frac{\frac{\sqrt{c+b} + \sqrt{c-b} \tan \frac{\eta}{2}}{\sqrt{c-b}}}{\frac{\sqrt{c+b} - \sqrt{c-b} \tan \frac{\eta}{2}}{\sqrt{c-b}}} \right) \right]$$

$$\frac{1}{R_3} = \left(\frac{\pi}{2} - \eta\right) \frac{k_f}{c} - \frac{bk_f}{c\sqrt{c^2 - b^2}} \left[\ln \left(\frac{\sqrt{c+b} + \sqrt{c-b}}{\sqrt{c+b} - \sqrt{c-b}} \right) - \ln \left(\frac{\sqrt{c+b} \cos \frac{\eta}{2} + \sqrt{c-b} \sin \frac{\eta}{2}}{\sqrt{c+b} \cos \frac{\eta}{2} - \sqrt{c-b} \sin \frac{\eta}{2}} \right) \right] \quad (4.16)$$

As a result;

$$\frac{1}{R_3} = \left(\frac{\pi}{2} - \eta\right) \frac{k_f}{c} - \frac{bk_f}{c\sqrt{c^2 - b^2}} \left[\ln \left(\frac{\left(\sqrt{c+b} + \sqrt{c-b}\right)^2}{\left(\sqrt{c+b}\right)^2 - \left(\sqrt{c-b}\right)^2} \right) - \ln \left(\frac{\left(\sqrt{c+b} \cos \frac{\eta}{2} + \sqrt{c-b} \sin \frac{\eta}{2}\right)^2}{\left(\sqrt{c+b} \cos \frac{\eta}{2}\right)^2 - \left(\sqrt{c-b} \sin \frac{\eta}{2}\right)^2} \right) \right]$$

$$\frac{1}{R_3} = \left(\frac{\pi}{2} - \eta\right) \frac{k_f}{c} - \frac{bk_f}{c\sqrt{c^2 - b^2}} \left[\ln \left(\frac{c + \sqrt{c^2 - b^2}}{b} \right) - \ln \left(\frac{\left(\tan \frac{\eta}{2} \sqrt{c-b} + \sqrt{c+b}\right)^2}{\left(\tan \frac{\eta}{2} \sqrt{c-b}\right)^2 - \left(\sqrt{c+b}\right)^2} \right) \right]$$

$$\frac{1}{R_3} = \left(\frac{\pi}{2} - \eta\right) \frac{k_f}{c} - \frac{bk_f}{c\sqrt{c^2 - b^2}} \left[\ln \left(\frac{c + \sqrt{c^2 - b^2}}{b} \right) - \ln \left(\frac{c + b \cos \eta + \sqrt{c^2 - b^2} \sin \eta}{b + c \cos \eta} \right) \right] \quad (4.17)$$

When the “ln” terms are put together;

$$\frac{1}{R_3} = \left(\frac{\pi}{2} - \eta\right) \frac{k_f}{c} - \frac{bk_f}{c\sqrt{c^2 - b^2}} \left[\ln \frac{\left(\frac{c + \sqrt{c^2 - b^2}}{b}\right)}{\left(\frac{c + b \cos \eta + \sqrt{c^2 - b^2} \sin \eta}{b + c \cos \eta}\right)} \right] \quad (4.18)$$

then, the final result for the third region ($b^2 < c^2$) is ;

$$\frac{1}{R_3} = \left(\frac{\pi}{2} - \eta\right) \frac{k_f}{c} - \frac{bk_f}{c\sqrt{c^2 - b^2}} \ln \left(\frac{\left(c + \sqrt{c^2 - b^2}\right)(b + c \cos \eta)}{b\left(c + b \cos \eta + \sqrt{c^2 - b^2} \sin \eta\right)} \right) \quad (4.19)$$

4.2.4. Thermal Resistance of the Forth Region, R_4

Inside the 4th region, there are three components; the main fiber, the barrier and the filler. For infinite divisions of the each region, (Figure 4.6), the thermal resistances are added such that,

$$dR_4 = dR_{4^1} + dR_{4^2} + dR_{4^3} \quad (4.20)$$

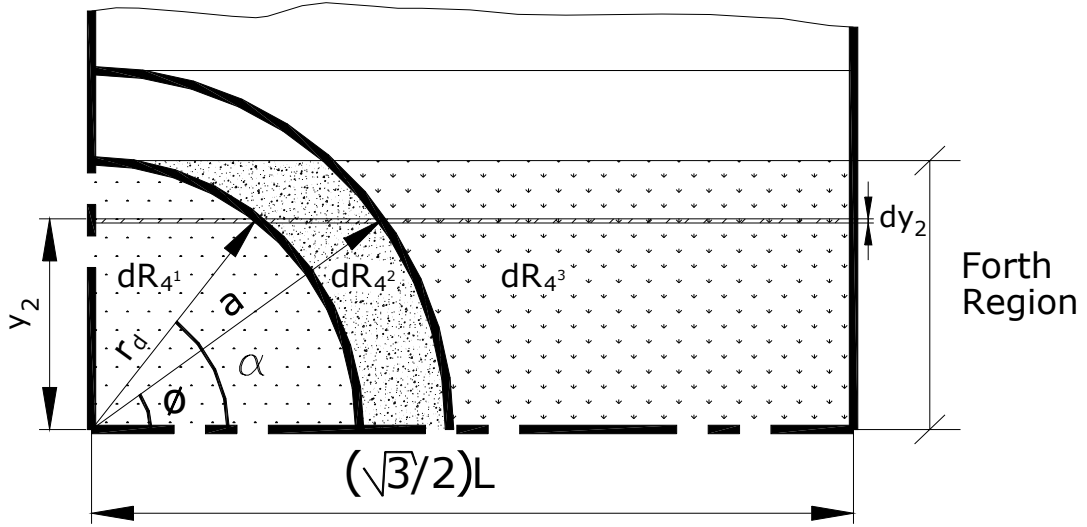


Figure 4.6. Schematic of the fourth region.

$$dR_4 = \frac{r_d \cos \alpha}{k_d dy_2} + \frac{a \cos \phi - r_d \cos \alpha}{k_b dy_2} + \frac{\frac{\sqrt{3}}{2}L - a \cos \phi}{k_f dy_2} \quad (4.21)$$

$$dR_4 = \frac{r_d \cos \alpha}{k_d a \cos \phi d\phi} + \frac{a \cos \phi - r_d \cos \alpha}{k_b a \cos \phi d\phi} + \frac{\frac{\sqrt{3}}{2}L - a \cos \phi}{k_f a \cos \phi d\phi}$$

$$\frac{1}{dR_4} = \frac{k_d k_b k_f a \cos \phi d\phi}{k_b k_f r_d \cos \alpha + k_f k_d (a \cos \phi - r_d \cos \alpha) + k_d k_b \left(\frac{\sqrt{3}}{2}L - a \cos \phi \right)} \quad (4.22)$$

where,

$$y_2 = r_d \sin \alpha = a \sin \phi$$

$$dy_2 = a \cos \phi d\phi$$

$$\sin \alpha = \frac{a}{r_d} \sin \phi$$

$$\cos \alpha = \sqrt{1 - \sin^2 \alpha} = \sqrt{1 - \left(\frac{a}{r_d} \sin \phi\right)^2} \quad (4.23)$$

$$\frac{1}{R_4} = \frac{k_d k_b k_f a \cos \phi d\phi}{k_b k_f r_d \sqrt{1 - \frac{a^2}{r_d^2} \sin^2 \phi} + k_d k_f \left\{ a \cos \phi - r_d \sqrt{1 - \frac{a^2}{r_d^2} \sin^2 \phi} \right\} + k_d k_b \left(\frac{\sqrt{3}}{2} L - a \cos \phi \right)} \quad (4.24)$$

It is also known from Figure (4.6) that ϕ is varying from 0° to η , and α is varying from η to 90° . Integrating equation (4.24),

$$\frac{1}{R_4} = \int_0^\eta \frac{k_d k_b k_f a \cos \phi d\phi}{k_b k_f r_d \sqrt{1 - \frac{a^2}{r_d^2} \sin^2 \phi} + k_d k_f \left\{ a \cos \phi - r_d \sqrt{1 - \frac{a^2}{r_d^2} \sin^2 \phi} \right\} + k_d k_b \left(\frac{\sqrt{3}}{2} L - a \cos \phi \right)}$$

The solution steps for the fourth region are as follows;

$$\frac{1}{R_4} = \int_0^\eta \frac{k_f \beta \gamma \cos \phi d\phi}{(\gamma - \beta) \sqrt{\frac{r_d^2}{a^2} - \sin^2 \phi} + \beta(1 - \gamma) \cos \phi + \beta \gamma b} \quad (4.25)$$

where;

$$\beta = \frac{k_d}{k_f} \quad (4.26)$$

$$\frac{1}{R_4} = \int_0^\eta \frac{k_f \cos \phi d\phi}{\left(\frac{1}{\beta} - \frac{1}{\gamma}\right) \sqrt{\frac{r_d^2}{a^2} - \sin^2 \phi} + \left(\frac{1}{\gamma} - 1\right) \cos \phi + b}$$

Considering the following relations lead to further mathematical manipulations:

$$d = \frac{1}{\beta} - \frac{1}{\gamma}$$

$$a = r + t$$

$$\frac{r_d^2}{a^2} = \frac{1}{\frac{a^2}{r_d^2}} = \frac{1}{\frac{(r_d + t)^2}{r^2}} = \frac{1}{\left(\frac{r_d + t}{r}\right)^2} = \frac{1}{\left(1 + \bar{t}\right)^2} \quad (4.27)$$

\bar{t} represents the dimensionless barrier thickness $\left(\bar{t} = \frac{t}{r_d}\right)$

Therefore, the last form of the integral becomes as follows;

$$\frac{1}{R_4} = \int_0^{\eta} \frac{k_f \cos \phi \, d\phi}{b + c \cos \phi + d \sqrt{\frac{1}{\left(1 + \bar{t}\right)^2} - \sin^2 \phi}} \quad (4.28)$$

4.3. Dimensionless Total Thermal Resistance of the Model, R_t

Dimensionless total thermal resistance of the model is found by inserting equation (4.4), (4.5), and either (4.13) for the case of $b^2 > c^2$ or (4.19) for $b^2 < c^2$, and also (4.28) into equation (4.3).

Therefore, the final form of the effective thermal conductivity becomes;

$$b^2 > c^2 \Rightarrow$$

$$\frac{1}{\bar{R}_t} = \left\{ \frac{2k_f}{\sqrt{3}} + \frac{k_f \left(\frac{L}{2} - a \right)}{\frac{\sqrt{3}}{2} L} + \left(\frac{\pi}{2} - \eta \right) \frac{k_f}{c} + \int_0^\eta \frac{k_f \cos \phi d\phi}{b + c \cos \phi + d \sqrt{\frac{1}{(1+t)^2} - \sin^2 \phi}} \right. \\ \left. - \frac{2bk_f}{c\sqrt{b^2 - c^2}} \left[\tan^{-1} \sqrt{\frac{b-c}{b+c}} - \tan^{-1} \left(\sqrt{\frac{b-c}{b+c}} \tan \frac{\eta}{2} \right) \right] \right\} \frac{1}{\sqrt{3} k_f} \quad (4.29)$$

$$b^2 < c^2 \Rightarrow$$

$$\frac{1}{\bar{R}_t} = \left\{ \frac{2k_f}{\sqrt{3}} + \frac{k_f \left(\frac{L}{2} - a \right)}{\frac{\sqrt{3}}{2} L} + \left(\frac{\pi}{2} - \eta \right) \frac{k_f}{c} + \int_0^\eta \frac{k_f \cos \phi d\phi}{b + c \cos \phi + d \sqrt{\frac{1}{(1+t)^2} - \sin^2 \phi}} \right. \\ \left. - \frac{bk_f}{c\sqrt{c^2 - b^2}} \ln \left(\frac{(c + \sqrt{c^2 - b^2})(b + c \cos \eta)}{b(c + b \cos \eta + \sqrt{c^2 - b^2} \sin \eta)} \right) \right\} \frac{1}{\sqrt{3} k_f} \quad (4.30)$$

After some minor simplifications of the both parts, dimensionless total thermal resistance of the model is obtained as;

$$b^2 > c^2 \Rightarrow$$

$$\begin{aligned}
\frac{1}{\bar{R}_t} = & 1 - \frac{\sqrt{3}}{3b} + \left(\frac{\pi}{2} - \eta\right) \frac{\sqrt{3}}{3c} + \frac{\sqrt{3}}{3} \int_0^\eta \frac{\cos \phi \, d\phi}{b + c \cos \phi + d \sqrt{\frac{1}{(1+t)^2} - \sin^2 \phi}} \\
& - \frac{2\sqrt{3}b}{3c\sqrt{b^2 - c^2}} \left[\tan^{-1} \sqrt{\frac{b-c}{b+c}} - \tan^{-1} \left(\sqrt{\frac{b-c}{b+c}} \tan \frac{\eta}{2} \right) \right]
\end{aligned} \tag{4.31}$$

$b^2 < c^2 \Rightarrow$

$$\begin{aligned}
\frac{1}{\bar{R}_t} = & 1 - \frac{\sqrt{3}}{3b} + \left(\frac{\pi}{2} - \eta\right) \frac{\sqrt{3}}{3c} + \frac{\sqrt{3}}{3} \int_0^\eta \frac{\cos \phi \, d\phi}{b + c \cos \phi + d \sqrt{\frac{1}{(1+t)^2} - \sin^2 \phi}} \\
& - \frac{\sqrt{3}b}{3c\sqrt{c^2 - b^2}} \ln \left(\frac{(c + \sqrt{c^2 - b^2})(b + c \cos \eta)}{b(c + b \cos \eta + \sqrt{c^2 - b^2} \sin \eta)} \right)
\end{aligned} \tag{4.32}$$

4.4. Calculation of the Volume Fractions of the Model

The area of the hexagon is;

$$\begin{aligned}
A_{\text{hexagon}} &= \frac{3\sqrt{3}}{2} L^2 \\
A_{\text{barrier}} &= \pi(a^2 - r_d^2) \\
A_{\text{disk}} &= \pi r_d^2 \\
A_{\text{barrier}} + A_{\text{disk}} &= \pi a^2
\end{aligned} \tag{4.33}$$

If the thickness of the model is 1 unit length, then the volume fraction of each region is found as follows:

Dimensionless volume fraction of the disk (filler fiber)

$$\bar{v}_d = \frac{\pi r_d^2}{\frac{3\sqrt{3}}{2} L^2} = \frac{2\pi}{3\sqrt{3}} \frac{r_d^2}{L^2} \quad (4.34)$$

Dimensionless volume fraction of the disk and barrier

$$\bar{v}_b + \bar{v}_d = \frac{\pi a^2}{\frac{3\sqrt{3}}{2} L^2} = \frac{2\pi}{3\sqrt{3}} \frac{a^2}{L^2} \quad (4.35)$$

To see the effect of the change of v_d on the value of b , the ratio of $\frac{L}{a}$ has to be calculated,

$$\bar{v}_b + \bar{v}_d = \frac{2\pi}{3\sqrt{3}} \frac{a^2}{L^2}$$

$$\frac{L^2}{a^2} = \frac{2\pi}{3\sqrt{3}(\bar{v}_b + \bar{v}_d)} \quad (4.36)$$

$$\frac{L}{a} = \sqrt{\frac{2\pi}{3\sqrt{3}(\bar{v}_b + \bar{v}_d)}} = \sqrt{\frac{2}{3\sqrt{3}}} \sqrt{\frac{\pi}{(\bar{v}_b + \bar{v}_d)}}$$

$$b = \frac{\sqrt{3}}{2} \frac{L}{a} = \frac{\sqrt{3}}{2} \sqrt{\frac{2}{3\sqrt{3}}} \sqrt{\frac{\pi}{(\bar{v}_b + \bar{v}_d)}} \approx 0.5373 \sqrt{\frac{\pi}{(\bar{v}_b + \bar{v}_d)}} \quad (4.37)$$

When v_b is 0, the value of b becomes;

$$b \approx 0.5373 \sqrt{\frac{\pi}{\bar{v}_d}} \quad (4.38)$$

The other b values depend on \bar{v}_d as given in Table 4.1.

Table 4.1. Dimensionless length (b) values.

\bar{v}_d	b
0.2	2.129187
0.3	1.738474
0.5	1.346616
0.7	1.138098
0.8	1.064593
0.95	0.977

4.5. Dimensionless Total Thermal Resistance of the Model without a Barrier

When there is no barrier then the model is considered to be consisting of three regions in a parallel connection as shown in Figure 4.7. Thermal resistances of the first and second regions are as follows, respectively.

$$\frac{1}{R_{1a}} = \frac{2k_f}{\sqrt{3}} \quad (4.39)$$

$$\frac{1}{R_2} = \frac{k_f \left(\frac{L}{2} - r_d \right)}{\frac{\sqrt{3}}{2} L} \quad (4.40)$$

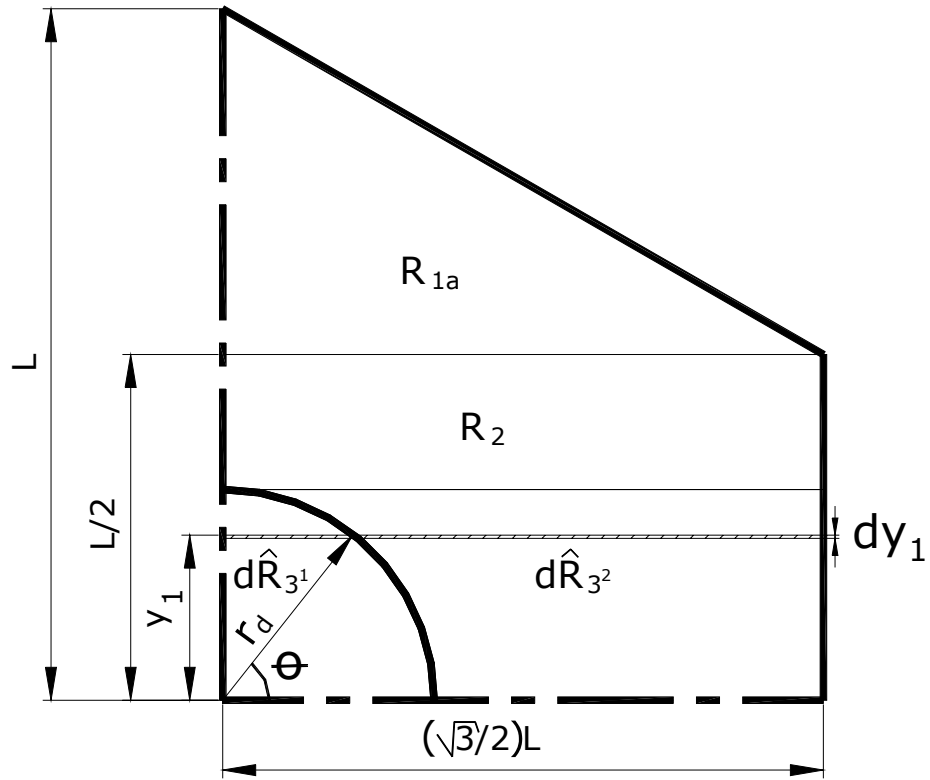


Figure 4.7. Schematic of the model without barrier.

Calculation of the thermal resistance of the third region requires more mathematical manipulations such that,

$$d\widehat{R}_3 = d\widehat{R}_{3^1} + d\widehat{R}_{3^2} = \frac{r_d \text{Cos}\theta}{k_d dy_1} + \frac{\left(\frac{\sqrt{3}}{2}L - r_d \text{Cos}\theta\right)}{k_f dy_1}$$

$$d\widehat{R}_3 = \frac{r_d k_f \text{Cos}\theta + \left(\frac{\sqrt{3}}{2}L - r_d \text{Cos}\theta\right) k_b}{k_d k_f dy_1} \quad (4.41)$$

where;

$$\begin{aligned} y_1 &= r_d \sin \theta \\ dy_1 &= r_d \cos \theta d\theta \end{aligned} \quad (4.42)$$

After putting the forms inside the equation (4.41), we get;

$$\frac{1}{d\widehat{R}_3} = \frac{k_d k_f r_d \cos \theta d\theta}{k_f r_d \cos \theta + \left(\frac{\sqrt{3}}{2} L - r_d \cos \theta \right) k_d} \quad (4.43)$$

Before solving the above equation, it is assumed that;

$$\widehat{b} = \frac{\sqrt{3}}{2} \frac{L}{r_d} \quad (4.44)$$

$$\widehat{c} = \frac{1}{\beta} - 1$$

After some mathematical manipulations, the equation (4.43) becomes;

$$\begin{aligned} \frac{1}{\widehat{R}_3} &= \int_0^{\frac{\pi}{2}} \frac{k_d k_f r_d \cos \theta d\theta}{k_f r_d \cos \theta + \left(\frac{\sqrt{3}}{2} L - r_d \cos \theta \right) k_d} \\ \frac{1}{\widehat{R}_3} &= \int_0^{\frac{\pi}{2}} \frac{k_f d\theta}{\widehat{c} + \widehat{b} \sec \theta} \end{aligned} \quad (4.45)$$

After integrating the right side of the above equation;

$$\frac{1}{\widehat{R}_3} = \frac{\pi k_f}{2 \widehat{b}} - \frac{\widehat{b} k_f}{\widehat{c}} \int_0^{\frac{\pi}{2}} \frac{d\theta}{\widehat{b} + \widehat{c} \cos \theta} \quad (4.46)$$

where;

θ is varying from 0° to 90°

If similar calculations are performed to solve equation (4.46), as it is done for the barrier case of equation (4.11), the solution depends on whether $\widehat{b}_2 > \widehat{c}_2$ or $\widehat{b}_2 < \widehat{c}_2$.

(*) $\widehat{b}^2 > \widehat{c}^2 \Rightarrow$

$$\frac{1}{\widehat{R}_3} = \frac{\pi k_f}{2 \widehat{c}} - \frac{2\widehat{b} k_f}{\widehat{c}\sqrt{\widehat{b}^2 - \widehat{c}^2}} \tan^{-1} \sqrt{\frac{\widehat{b} - \widehat{c}}{\widehat{b} + \widehat{c}}} \quad (4.47)$$

(*) $\widehat{b}^2 < \widehat{c}^2 \Rightarrow$

$$\frac{1}{\widehat{R}_3} = \frac{\pi k_f}{2 \widehat{c}} - \frac{\widehat{b} k_f}{\widehat{c}\sqrt{\widehat{c}^2 - \widehat{b}^2}} \ln \left(\frac{\widehat{c} + \sqrt{\widehat{c}^2 - \widehat{b}^2}}{\widehat{b}} \right) \quad (4.48)$$

Total dimensionless thermal resistance of the model without barrier is calculated as;

$$\frac{1}{\widehat{R}_t} = \left(\frac{1}{R_{1a}} + \frac{1}{R_2} + \frac{1}{\widehat{R}_3} \right) \frac{1}{\sqrt{3} k_f} \quad (4.49)$$

For $\widehat{b}^2 > \widehat{c}^2 \Rightarrow$

$$\frac{1}{\widehat{R}_t} = 1 - \frac{\sqrt{3}}{3\widehat{b}} + \frac{\pi \sqrt{3}}{2 \cdot 3\widehat{c}} - \frac{2\sqrt{3} \widehat{b}}{3\widehat{c}\sqrt{\widehat{b}^2 - \widehat{c}^2}} \tan^{-1} \sqrt{\frac{\widehat{b} - \widehat{c}}{\widehat{b} + \widehat{c}}} \quad (4.50)$$

$\widehat{b}^2 < \widehat{c}^2 \Rightarrow$

$$\frac{1}{\bar{R}_t} = 1 - \frac{\sqrt{3}}{3\hat{b}} + \frac{\pi\sqrt{3}}{2\ 3\hat{c}} - \frac{\sqrt{3}\hat{b}}{3\hat{c}\sqrt{\hat{c}^2 - \hat{b}^2}} \ln\left(\frac{\hat{c} + \sqrt{\hat{c}^2 - \hat{b}^2}}{\hat{b}}\right) \quad (4.51)$$

4.6. Computer Implementation of the Analytical Model

MATLAB programming (given in the Appendix) is used to implement the equations (4.29) and (4.30). Since these equations require for solving the integral part, the Simpson Method was used [5].

In Simpson's Rule, since the integral is the total area under the curve, the interval [a,b] is divided into an even number of n subintervals. The divisions are called $x_0=a, x_1, x_2, \dots, x_n=b$ and in this division, the x_i can be found as $x_i = a + i.\Delta x$

where

$$i = 0, 1, 2, \dots, n$$

$$\Delta x = \frac{b - a}{n}$$

The approximation scheme of the method for n=6 is given as

$$\int_a^b f(x)dx \approx \frac{\Delta x}{3} [f(x_0) + 4f(x_1) + 2f(x_2) + 4f(x_3) + 2f(x_4) + 4f(x_5) + f(x_6)] \quad (4.52)$$

Therefore, the integral part of the model is implemented such that;

$$\int_0^n \frac{\cos \phi \ d\phi}{b + c \cos \phi + d \sqrt{\frac{1}{(1+t)^2} - \sin^2 \phi}} \approx \frac{\Delta x}{3} [f(x_0) + 4f(x_1) + 2f(x_2) + 4f(x_3) + 2f(x_4) + 4f(x_5) + f(x_6)] \quad (4.53)$$

where

$$\Delta x = \frac{\eta}{6}$$

$$x_0 = 0, \quad x_1 = \frac{\eta}{6}, \quad x_2 = \frac{\eta}{3}, \quad (4.54)$$

$$x_3 = \frac{\eta}{2}, \quad x_4 = \frac{2\eta}{3}, \quad x_5 = \frac{5\eta}{6}, \quad x_6 = \eta$$

This form was applied in the integral form which is shown in equation 48, then;

$$f(x_0) = \frac{\cos 0}{b + c \cos 0 + d \sqrt{\frac{1}{(1+t)^2} - \sin^2 0}} = \frac{1}{b + c + d \sqrt{\frac{1}{(t+1)^2}}} \quad (4.55)$$

$$f(x_1) = \frac{\cos \frac{\eta}{6}}{b + c \cos \frac{\eta}{6} + d \sqrt{\frac{1}{(1+t)^2} - \sin^2 \frac{\eta}{6}}} \quad (4.56)$$

$$f(x_2) = \frac{\cos \frac{2\eta}{6}}{b + c \cos \frac{2\eta}{6} + d \sqrt{\frac{1}{(1+t)^2} - \sin^2 \frac{2\eta}{6}}} \quad (4.57)$$

$$f(x_3) = \frac{\cos \frac{\eta}{2}}{b + c \cos \frac{\eta}{2} + d \sqrt{\frac{1}{(1+t)^2} - \sin^2 \frac{\eta}{2}}} \quad (4.58)$$

$$f(x_4) = \frac{\cos \frac{2\eta}{3}}{b + c \cos \frac{2\eta}{3} + d \sqrt{\frac{1}{(1+t)^2} - \sin^2 \frac{2\eta}{3}}} \quad (4.59)$$

$$f(x_5) = \frac{\cos \frac{5\eta}{6}}{b + c \cos \frac{5\eta}{6} + d \sqrt{\frac{1}{(1+t)^2} - \sin^2 \frac{5\eta}{6}}} \quad (4.60)$$

$$f(x_6) = \frac{\cos \eta}{b + c \cos \eta + d \sqrt{\frac{1}{(1+t)^2} - \sin^2 \eta}} \quad (4.61)$$

4.7. References

1. Zou, M. Q., Yu, B. M., and Zhang, D. M., “*An analytical Solution for Transverse Thermal Conductivities of Unidirectional Fiber Composites with Thermal Barrier*”, J. Phys. D., **2002**, 35, 1867-1874.
2. Spiegel, M. R., Mathematical Handbook, Schaum’s Outline Series.
3. Standard Mathematical Tables, CRC Press, 26th Edition, **1981**.
4. Handbook of Mathematical, Scientific and Engineering Formulas, Tables, Functions, Graphs, Transforms, Research Education Association, **1994**.
5. Ciarlet, P.G., and Lions, J.L., Handbook of Numerical Analysis, Amsterdam; New York, **1990**.

CHAPTER 5

HEAT TRANSFER ANALYSIS OF NANO-MICRO FIBER COMPOSITES BY FINITE ELEMENT METHOD

5.1. Introduction

The purpose of this study is to investigate the thermal behavior of fiber composites by using finite element package program “ANSYS 7.0”. The fiber size varies between nano and micro level. The fibers also show difference in terms of direction, and shape. The effective thermal conductivity, total heat flow, temperature difference and heat flux are analyzed.

In the literature, many heat transfer problems in the area of fiber composites were solved by using finite element analysis. In many situations, calculation of heat conduction gave sufficient solution [1].

Finite Element Method (FEM) is a numerical tool to solve numerous kinds of problems. The technique depends on the decomposition of a domain with a complicated geometry into geometrically simple elements. Once the single element solution is obtained, it is used to get the complete system by applying the boundary conditions.

Basically, FEM consists of the following steps [2];

- a. Discretization of the domain which is a part of the process of dividing the geometry into smaller pieces called meshing.
- b. Set-up element matrices,
- c. Transformation from natural coordinates into local coordinates,
- d. Assembly,
- e. Introduction of boundary conditions,
- f. Solution of the linear system of equations.

5.2. A simple FEM Model

Basic steady state heat transfer equation for Figure 5.1 is written as;

$$\frac{d}{dx} \left(k \frac{dT}{dx} \right) + Q = 0 \quad 0 < x < L \quad (5.1)$$

Where x is the length of the thin rod, Q is the generated heat and T is the temperature [1].

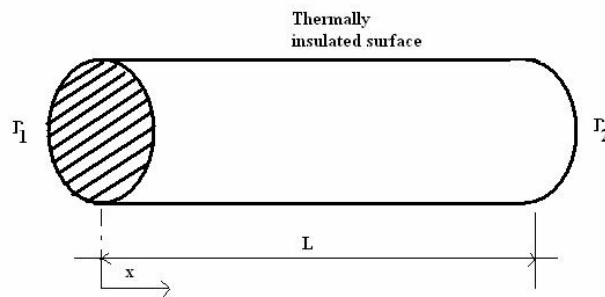


Figure 5.1. Heat conduction in a thin rod [1].

It is considered that the general boundary conditions are

$T=f$ on τ_1 and $q=\chi$ on τ_2 .

The FEM analysis starts with choosing the appropriate element type which is “the linear element” for this model. When the linear element is employed to the structure, Figure 5.1 transforms into Figure 5.2.

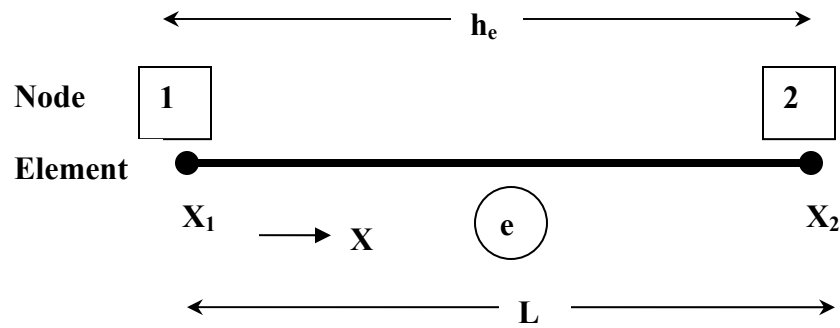


Figure 5.2. Number of the nodes on the element [1].

$$x = \sum_{j=1}^2 x_j N_j(\xi) = \frac{(x_1 + x_2)}{2} + h_e \frac{\xi}{2} = \frac{h_e}{2} + h_e \frac{\xi}{2} \quad (5.2)$$

Here, N_1 and N_2 are orderly $N_1(\xi) = \frac{(1-\xi)}{2}$ and $N_2(\xi) = \frac{(1+\xi)}{2}$

with the trial function;

$$\hat{T} = \sum_{j=1}^2 T_j N_j(\xi)$$

When this is inserted in the main equation (5.2)

$$\int_e k \frac{d\hat{T}}{dx} \frac{dN_i}{dx} dx = \int_e Q N_i dx - q_i, \quad i=1,2$$

$$q_i = [\hat{q}N_i]_r = [\hat{q}N_i]_{r_1} + [\hat{q}N_i]_{r_2}$$

$$\sum_{j=1}^2 \left[\int_e k \frac{dN_j}{dx} \frac{dN_i}{dx} dx \right] T_j = \int_e Q N_i dx - q_i, \quad i=1,2$$

$$\sum_{j=1}^2 \left[\int_e k \frac{dN_j}{dx} \frac{dN_i}{dx} dx \right] T_j = \sum_{j=1}^2 \left[\int_e N_j N_i dx \right] Q_j - q_i, \quad i=1,2$$

$$\sum_{j=1}^2 \left[\int_{-1}^1 k \frac{dN_j}{d\xi} \frac{dN_i}{d\xi} \frac{d\xi}{dx} dx \right] T_j = \sum_{j=1}^2 \left[\int_{-1}^1 N_j N_i \frac{dx}{d\xi} d\xi \right] Q_j - q_i, \quad i=1,2$$

$$dx = h_e \frac{d\xi}{2}$$

If the above equations are summed up;

$$\sum_{j=1}^2 \left[\frac{2}{h_e} \int_{-1}^1 k \frac{dN_j}{d\xi} \frac{dN_i}{d\xi} d\xi \right] T_j = \sum_{j=1}^2 \frac{h_e}{2} \left[\int_{-1}^1 N_j N_i d\xi \right] Q_j - q_i, \quad i=1,2$$

$$K_e T_e = M_e Q_e - q_e$$

Stiffness matrix is obtained as;

$$[K_e]_{ij} = \frac{2}{h_e} \int_{-1}^1 k \frac{dN_j}{d\xi} \frac{dN_i}{d\xi} d\xi$$

The mass matrix;

$$[M_e]_{ij} = \frac{h_e}{2} \left[\int_{-1}^1 N_j N_i d\xi \right]$$

The element vectors are;

$$T_e = \begin{bmatrix} T_1 \\ T_2 \end{bmatrix} \quad Q_e = \begin{bmatrix} Q_1 \\ Q_2 \end{bmatrix} \quad q_e = \begin{bmatrix} q_1 \\ q_2 \end{bmatrix}$$

And finally by combining all of them;

$$K_e = \frac{k_e}{h_e} \begin{bmatrix} 1 & -1 \\ -1 & 1 \end{bmatrix}$$

$$M_e = \frac{h_e}{6} \begin{bmatrix} 2 & 1 \\ 1 & 2 \end{bmatrix}$$

If the other element types are used, instead of linear element, which is the simplest element, the accuracy becomes higher, as shown in Figure 5.3. These elements are compared with the exact solution.

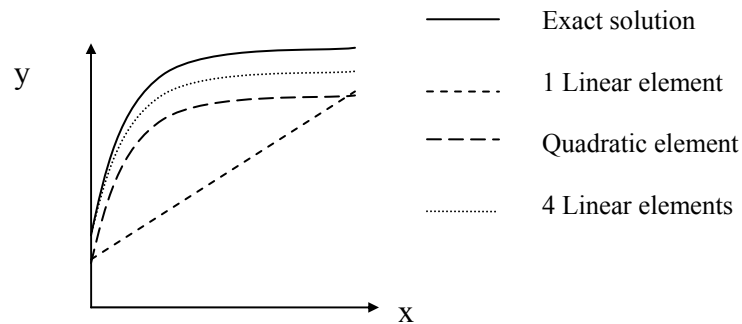


Figure 5.3. The finite element division.

It is clear that the more we divide the shape into parts, the more accurate results we get. But in nano size, it is not possible to divide the volume into many parts. ANSYS can solve and divide the problems up to 10^{-60} m. It makes a distinction for nanosize.

5.3. Modeling with ANSYS

The ANSYS software is evolved from a structural finite element analysis tool into a well developed multiphysics analysis tool and it has a capacity to be used in a broad range of areas including structural, thermal, fluid, acoustics, electromagnetics and electronic circuits more than 30 years. Especially the ANSYS/Multiphysics product can make a coupling between these physical areas. The size of the physical area can be down to the micro-system scale (10^{-6} m) and in some areas into the nano-scale (10^{-9} m) range [1].

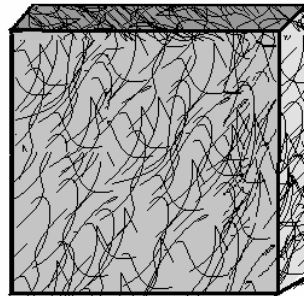
In ANSYS product family, steady-state and transient thermal analyses are supported by the divisions of ANSYS/Multiphysics, ANSYS/Mechanical, ANSYS/FLOTRAN and ANSYS/Thermal. In this study, ANSYS/Multiphysics was used to solve the steady-state problems.

The solution procedure

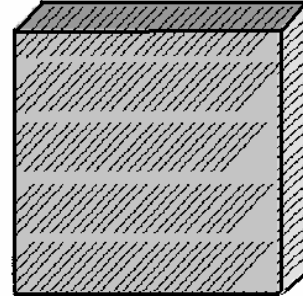
The basis for thermal analysis in ANSYS is a heat balance equation obtained from the principle of conservation of energy. The finite element solution performed via ANSYS calculates nodal temperatures, and then uses the nodal temperatures to obtain other thermal quantities. The ANSYS program could support five types of thermal boundary conditions; constant temperatures, constant heat fluxes, applied heat transfer (film) coefficient of convections, heat flow rates, and heat generation rates.

Step 1. Problem

Nano-micro fibers in the composite could be in the form of either aligned or random (Figure 5.4). In the modeling phase we considered our composite as aligned to use symmetry.



Random fiber composite



Aligned fiber composite

Figure 5.4. Composite structures

Step 2. Model

In modeling, (a) fiber volume fraction and matrix volume fraction, (b) fiber aspect ratio, (c) fiber-matrix modulus ratio, (d) fiber spacing, (e) fiber orientation and (f) fiber end gap size are important. Both the matrix and fiber must be taken in nano-level in the modeling phase.

In Figure 5.5, the models used in ANSYS are given for both 2-D and 3-D models.

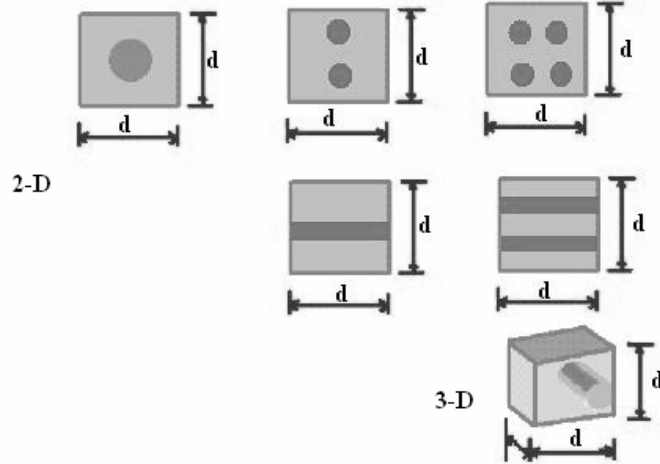


Figure 5.5. Radial, axial and 3-D nano-micro composite models (d: the length of the unit cells).

The model sizes inside the interface differ between nano and micro size: therefore, it is important to emphasize that the necessary computer memory increases as we decrease the size of the filler fiber, as can be seen in Figure 5.5. This comparison was done for 2-D models.

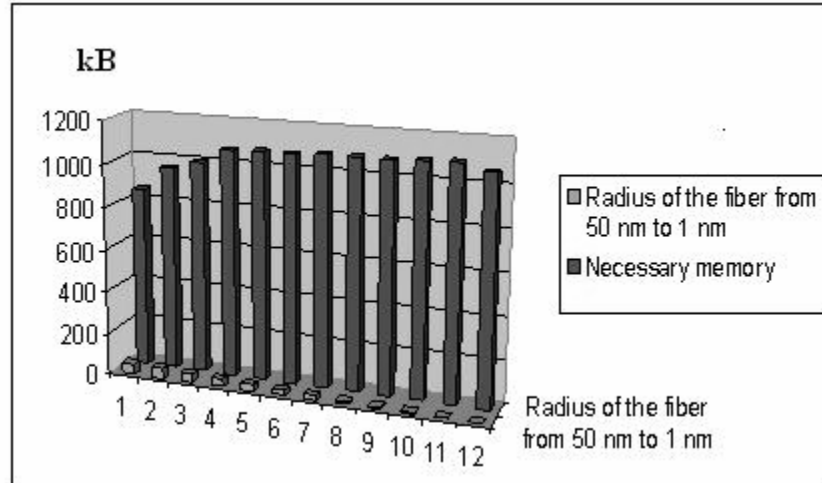


Figure 5.6. Necessary computer memory in modeling

Figure 5.6 shows the necessary memory for the modeling. When the size of the fiber decreases, the required memory size increases.

Step 3: ANSYS Analysis type

Thermal analysis in the ANSYS has four different element types. The first one is mass element that allows us to consider melting and freezing. The others are link, solid and shell elements. Solid element is used if in-plane and transverse conduction is needed.

Commonly used 2-D ANSYS elements

The first element type used in this study is PLANE35 2-D triangular thermal solid. It has a 6-node triangular element. It has a triangular shape which allows meshing

in irregular structures. It has one degree of freedom, and temperature, at each node (Figure 5.7).

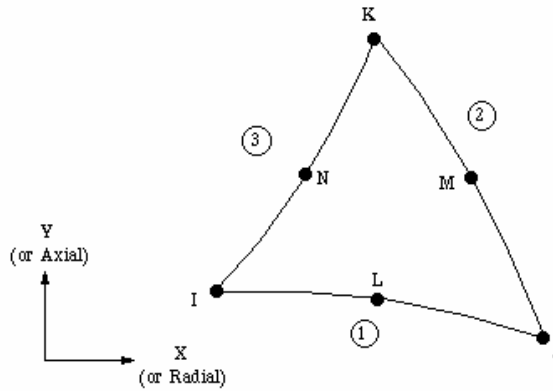


Figure 5.7. PLANE35 2-D 6 node triangular thermal solid [3].

The other element type “SOLID90” was used in modeling that has 20 nodes with a single degree of freedom (Figure 5.8).

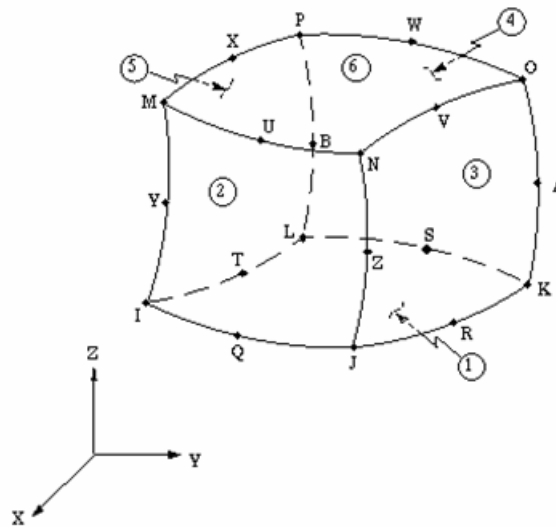


Figure 5.8. SOLID90 3-D 20 node triangular thermal solid [3].

Step 4. Material Properties

The thermal conductivity for nano-micro fibers was taken as a nanoclay thermal conductivity from the literature around 0.2 W/mK and for polymer or matrix around 1.2 W/mK.

Step 5. Meshing

There are four main element types for thermal analysis; mass, beam, link and solid. Beam models are for 1-D line models, but they are simple for advanced calculations. Mass model is only for specific needs such as melting. Based on the element type, appropriate mesh is chosen for the solution. The mesh types are shown in Figure 5.9.

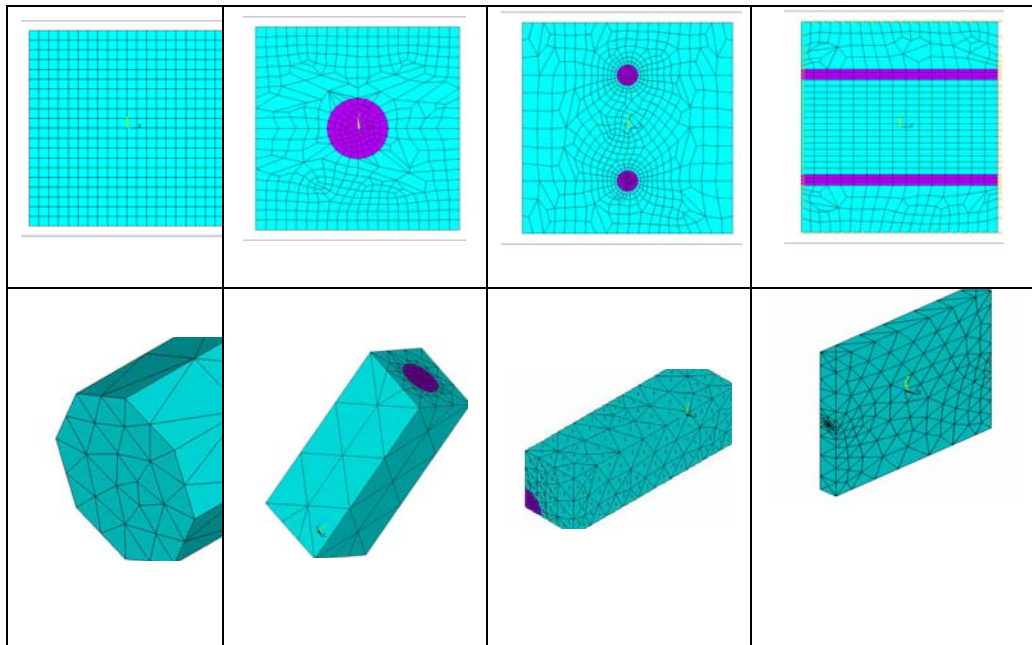


Figure 5.9. Mesh types of 2-D and 3-D nano-micro composite models

Step 6. Boundary Conditions and Applied Loads.

In ANSYS, for the thermal analysis, the following loads can be applied;

1. Convection
2. Radiation
3. Heat flow rates
4. Heat fluxes (heat flow per unit area)
5. Heat generation rates (heat flow per unit volume)
6. Constant temperature boundaries.

In the modeling, only the constant temperature and constant heat flux were applied.

5.4. Modeling Configurations

5.4.1. The Effect of Material Properties of the Filler Fiber

In this configuration, the effect of fiber material properties on the temperature difference profiles is obtained. Eight different material properties were used to obtain the temperature difference.

The geometry is a 2-D rectangle model. The fiber, which is in the cylindrical form is used as filler (Figure 5.10).

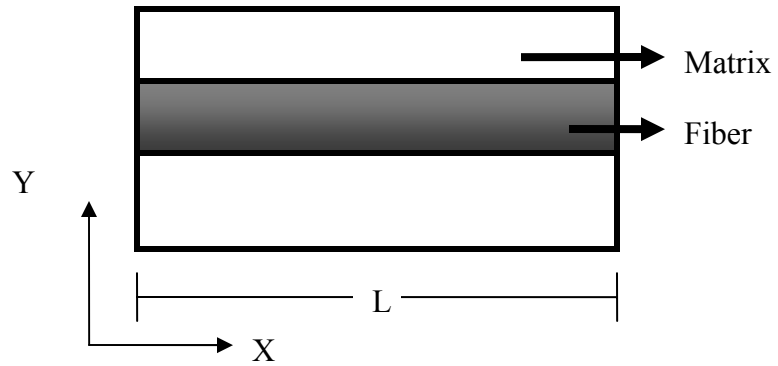


Figure 5.10. Problem description

Meshing is done after defining the material properties and the element type for the problem. Figures 5.11 and 5.12 show the meshing types for 3-D models.

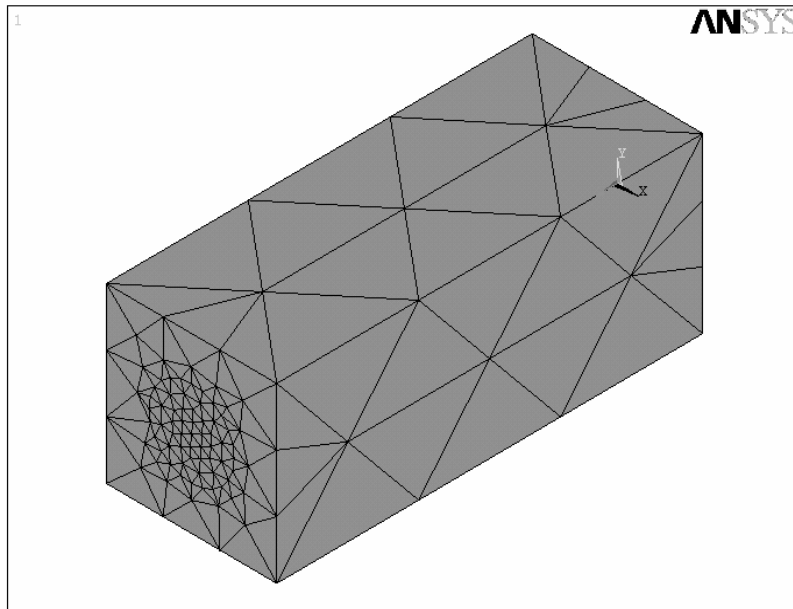


Figure 5.11. Mesh model of the problem

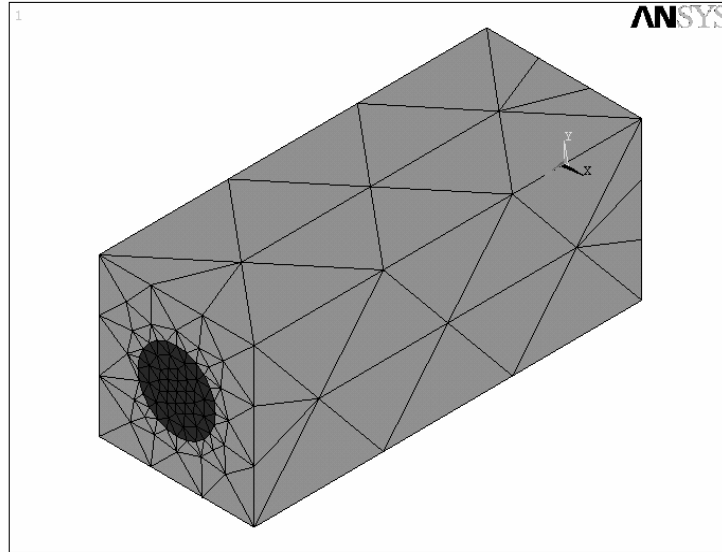


Figure 5.12. Application of two different materials.

Temperature difference was applied as a load to both right and left side in Figure 5.12. The bottom and upper parts were thermally isolated.

Materials with different thermal conductivity values were used for the fiber and matrix, as shown in Table 5.1.

Table 5.1. Thermal conductivity of the materials.

Materials	Thermal conductivity (W/mK)
PVA	2
Acrylic	0.2
Graphite	24
Carbon	1.7
Nylon 6	0.26
Polyethylene	0.46
Polypropylene	0.12
Polystyrene	0.13

The temperature distribution of the materials is given in Figure 5.13.

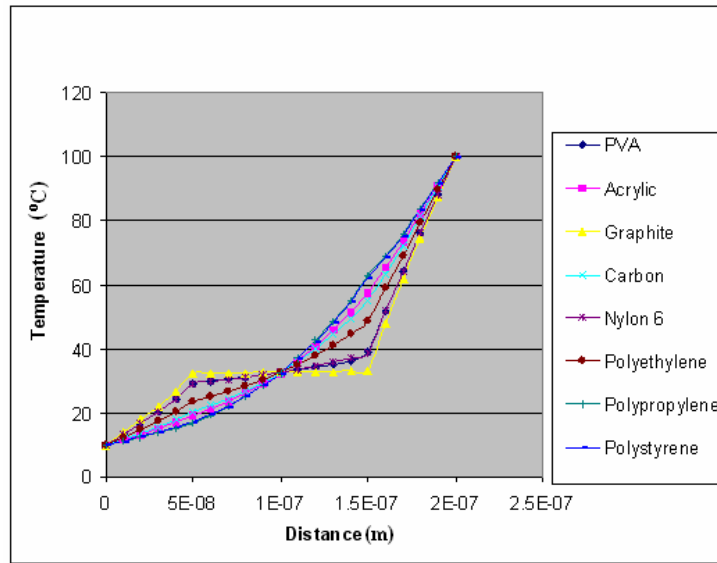


Figure 5.13. Temperature distribution for different materials.

5.4.2. Polymer’s Heat Deflection Temperature (HDT)

The polymer’s deflection temperature (HDT) can differ from one polymer to another polymer. If HDT is taken around 150° C, the maximum applicable heat flux was found for different radius of nanofiber. In Table 5.2., the HDT values of some polymers are given.

Table 5.2. Some of the polymers’ heat deflection temperatures and melting points [4].

Polymer Type	Deflection Temperature at 0.46 MPa (°C)	Deflection Temperature at 1.8 MPa (°C)	Melting Point (°C)
Acrylic	95	85	130
Nylon 6	160	60	220
Nylon 6 + 30% Glass Fiber	220	200	220
Polyethylene, HDPE	85	60	130
PET + 30% Glass Fiber	250	230	250
Polypropylene + 30% Glass Fiber	170	160	170
Polystyrene	95	85	-

Applied loads

- Constant temperature to the rectangular shape with cylindrical filler was applied to the left, top and bottom sides as 10 °C and, to the right side as 100 °C. The temperature distributions are given in Chapter 6. Also to get one dimensional temperature distribution, temperature was only applied on the left and right sides.
- Constant heat flux was applied to reach the heat deflection temperature (HDT). This is the temperature at which a standard test bar deflects 0.25 mm under a stated load of either 0.45 MPa or 1.82 MPa.
- To reach the HDT values, the necessary heat flux values are given in Figure 5.14.

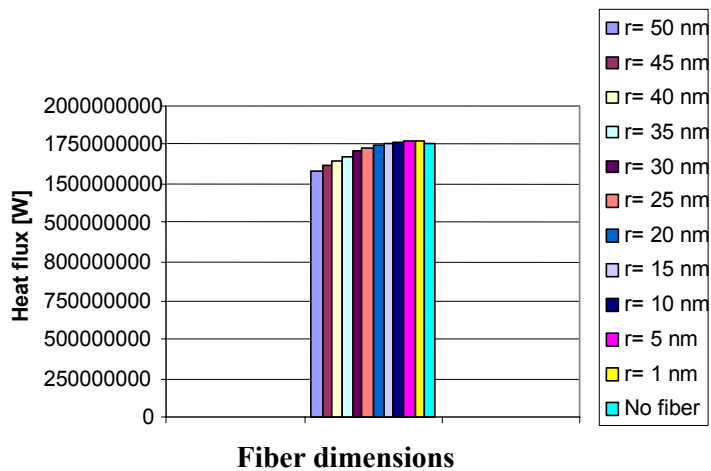


Figure 5.14. Maximum heat flux values for composite thermal stability.

5.4.3. Defining the Unit Cells

Rectangular and hexagonal unit cells are compared for the nano-micro composite study.

A square which has a dimension of $L \times L$ (in the model it was taken as 2 mm) and a hexagon with a length of L for each side were taken as a dimension in ANSYS. By using different fiber volume fraction, the dimensionless effective conductivities were found and compared with each other to discuss which unit cell is more suitable for our study.

As seen from Figure 5.15, both models have similar volume fraction, applied boundary conditions and material properties. As boundary conditions, -1°C and 1°C were applied to the left and right sides, respectively.

The dimensionless effective conductivity, which is explained in detail in Chapter 6, was found by using the average thermal flux value in the X direction when $Y = L/2$.

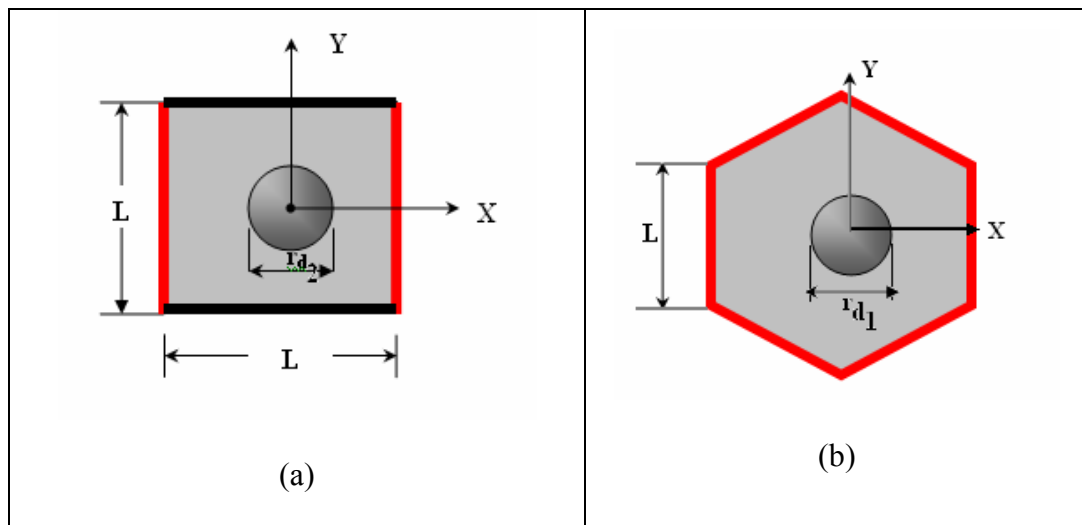


Figure 5.15. Unit cells a) Rectangular unit cell, b) Hexagonal unit cell

Table 5.3 lists the dimensionless effective thermal conductivities that were found depending on the material properties.

Table 5.3. Material properties and dimensionless effective thermal conductivities of the hexagonal and rectangular unit cells.

Example ($V_d=0.1$)	Fiber	Matrix	Effective Thermal Conductivity (k_e)		Dimensionless Effective Thermal Conductivity (k_e^+)		Rule of Mixtures	Comparison with Rule of Mixt. (%)	
	K_{e1} (W/mK)	K_{e2} (W/mK)	Rect.	Hex.	R	H		R	H
1	0.1	10	8.24	6.53	0.824	0.653	0.8002	109.34	137.9
2	10	10	10	10.04	1	1.004	1	100	99.60
3	100	10	11.8	14.4	1.18	1.44	3.7	161.02	131.9
Example ($V_d=0.2$)	Fiber	Matrix	Effective Thermal Conductivity (k_e^+)		Dimensionless Effective Thermal Conductivity (k_e^+)		Rule of Mixtures	Comparison with Rule of Mixt. (%)	
	K_{e1} (W/mK)	K_{e2} (W/mK)	Rect.	Hex.	R	H		R	H
1	0.1	10	6.76	4.8	0.676	0.48	0.802	118.64	167.1
2	10	10	10	10.2	1	10.02	1	100	98.04
3	100	10	13.9	18.71	1.39	1.871	2.8	201.44	149.6
Example ($V_d=0.3$)	Fiber	Matrix	Effective Thermal Conductivity (k_e^+)		Dimensionless Effective Thermal Conductivity (k_e^+)		Rule of Mixtures	Comparison with Rule of Mixt. (%)	
	K_{e1} (W/mK)	K_{e2} (W/mK)	Rect.	Hex.	R	H		R	H
1	0.1	10	5.61	2.44	0.561	0.244	0.703	125.12	288.1
2	10	10	10	10.07	1	1.007	1	100	99.30
3	100	10	16.4	25.2	1.64	2.52	3.7	225.61	146.8

Generally, thermal conductivity of the filler fibers has bigger values than the matrix and in order to use a conventional model, the difference between the thermal conductivities must be significant [5]. As seen from Table 5.3, compared to the rectangular unit cell, the hexagonal unit cell has less error with respect to the rule of mixtures. This leads us to use hexagonal cell for the ANSYS analysis.

Heat flux variation and temperature distribution of the unit cells are given below.

Figure 5.16 is the temperature difference and Figure 5.17 is the heat flux in the X

direction for rectangular shape. Figure 5.18 and 5.19 show the temperature and heat flux variation for the hexagonal shape.

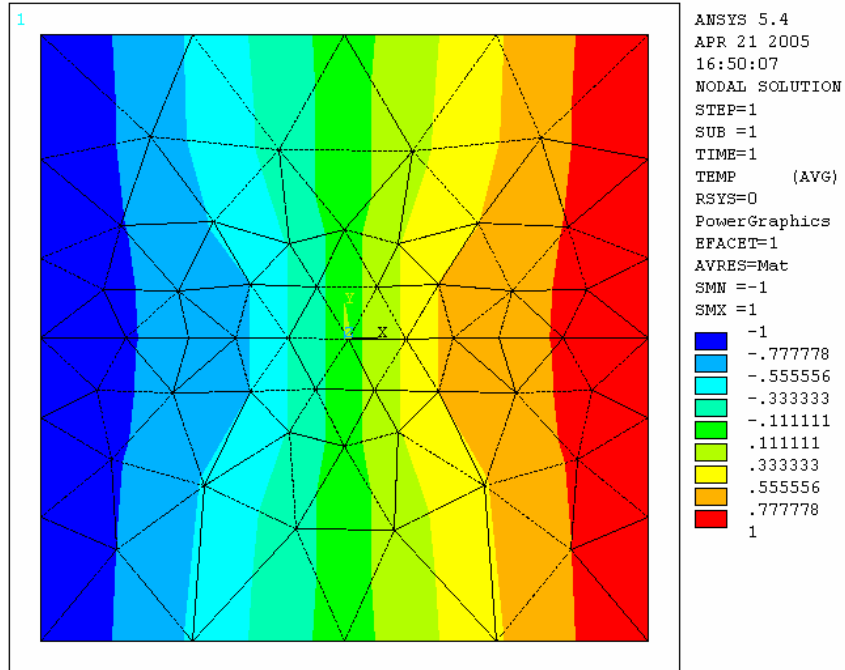


Figure 5.16. Temperature distribution in the X direction for rectangular shape.

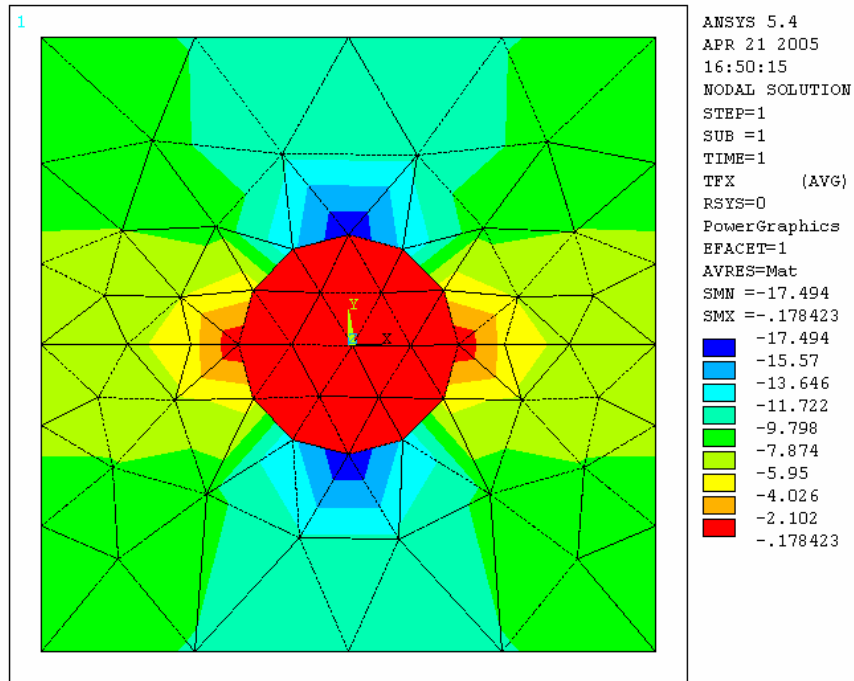


Figure 5.17. Heat flux variation in the X direction for rectangular shape.

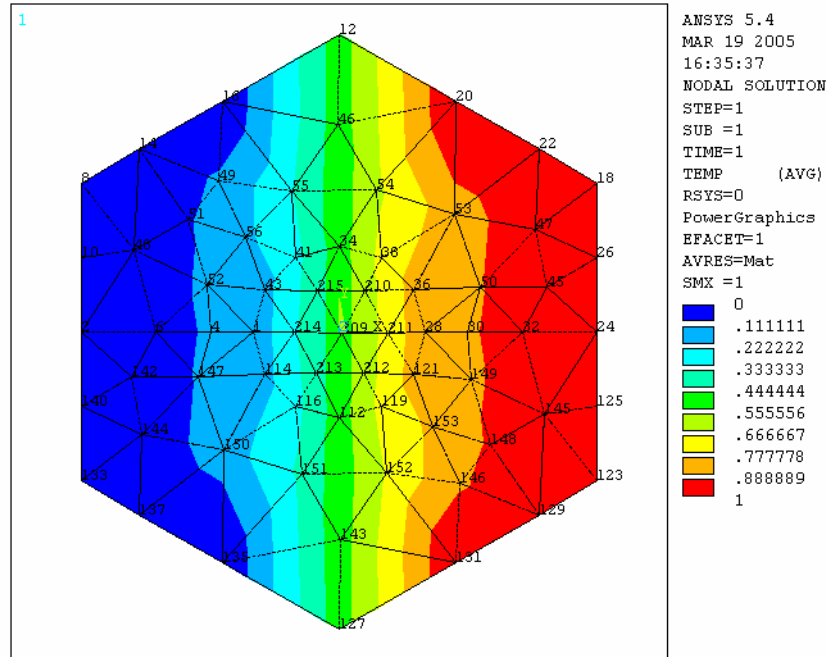


Figure 5.18. Temperature distribution in the X direction for hexagonal shape.

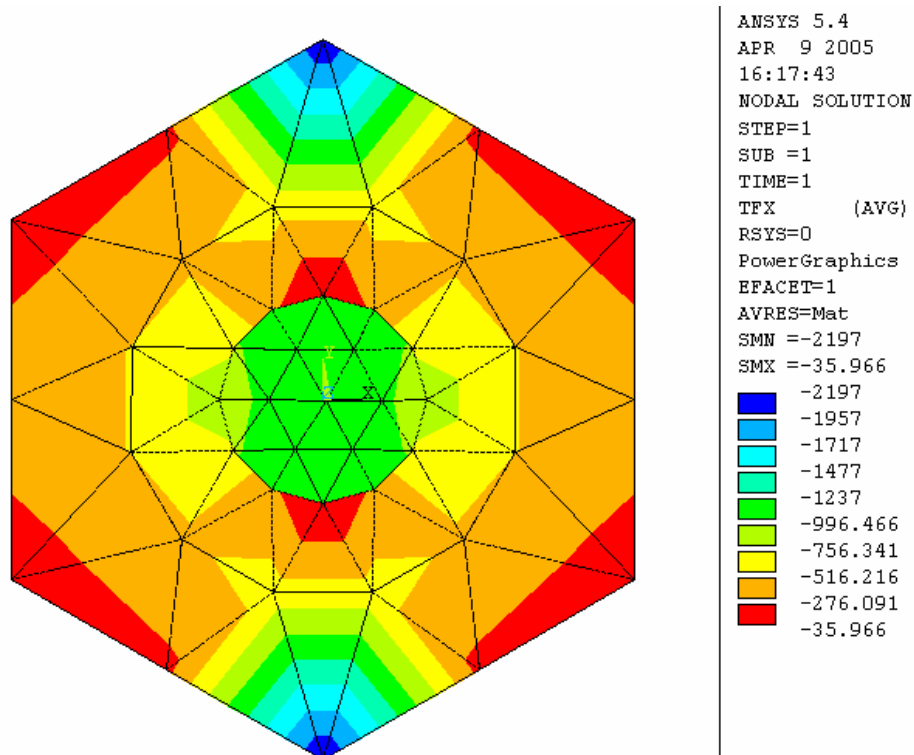


Figure 5.19. Heat flux distribution in the X direction for hexagonal shape.

5. 5. References

1. Lewis, R.W., The Finite Element Method in Heat Transfer, Wiley, **1996**.
2. Lecture notes, http://www.ltm.uni-erlangen.de/mitarbeiter/Willner/exerciseWillner_061204.pdf (accessed in Jan. 2005)
3. <http://www.ansys.com/services/documentation/manuals.htm> (accessed in May 2004).
4. <http://www.matweb.com/reference/deflection-temperature.asp> (accessed in March 2005)
5. Nan, C.-W., Shi, Z., Lin, Y., “A Simple Model for Thermal Conductivity of Carbon Nanotube-based Composites”, Chemical Physics Letters, **2003**, 375, 666-669.

CHAPTER 6

RESULTS AND DISCUSSION

Thermal conductivity of materials may differ from one material to another and it is considered as one of the main heat transfer properties of the materials. The recent studies have shown that, the dimensionless effective thermal conductivity is important for the flame resistance behavior of materials.

In this study, a heat transfer model is developed to discuss the dimensionless effective thermal conductivity of the nano-micro fiber composites and a device is developed for continuous yarn manufacturing based on nano-micro sized fibers.

Modeling studies consist of two parts: analytical and numerical modeling. The analytical heat transfer model is based on electrical analogy technique in which heat was considered to be applied in only one direction and therefore analytical modeling of transverse thermal conductivity became possible.

The analytical modeling was done considering the filler fiber placed inside another fiber which is different from the most other situations in which the composite is considered having fiber as reinforcement in a matrix. Here, since reinforcement and matrix have cylindrical shape, the hexagonal unit model was developed to study the heat transfer behavior.

The hexagonal model has three regions including the barrier region. The thickness of the barrier is normally around 10^{-6} - 10^{-8} m in the previous composite studies. In the ANSYS and MATLAB modeling, the thickness size was taken as $(0.1-0.3)*r_d$. Since the barrier thickness was taken as a separate region, after some value of the thickness, no difference in terms of k_e was observed. Comparisons were done among the three methods: analytical modeling using MATLAB, rule of mixture which is used only when the barrier thickness is taken to be zero and the ANSYS modeling.

For the analytical results, the MATLAB program was used to develop a simple model and then the boundary conditions were applied to it. For the ANSYS modeling, thermal conductivity values of the regions were given and then the total effective thermal conductivity was obtained by using the thermal flux values in the X direction. In the ANSYS modeling, since the model is not 3-D and the analysis type is steady-state, the whole shape was taken into consideration instead of the half part. If the symmetry property has to be used, there has to be symmetry in terms of physical structure, material properties and the applied loads. Among these, if one is not performed, the symmetry can not be considered. In the present model, the symmetry line is where $y=0$.

Another objective of this study is to develop continuous yarn from micro-nano sized fibers. Electrospinning method is used to produce and collect the fibers. Pulling and twisting of the yarn was done as a second step.

From the SEM results, it was seen that the radius of the fibers manufactured by electrospinning method varied between 200 nm and 2 μ m which is big enough to consider the continuum approach such as FEM for our model since it is well known that when the size of the particle is not bigger than the free path, the continuum approach

breaks down. Therefore, the term “nano-micro” is used in our study to include both nano and micro concepts.

For the most of the thermal conductivity models, it is known that when the volume fraction of the filler is less than 20-30%, most of the models do not give correct values. In this research, it was observed that, once the hexagonal shape is used, the volume fraction of the filler can be decreased to 10%.

6.1. MATLAB Results

The analytical model was solved by using MATLAB to find the variation of the dimensionless effective thermal conductivity. As for the thermal resistance approach and the dimensionless attempt to simplify the last form of the analytical equation, firstly, the equation was solved considering no barrier thickness in the model which makes the model consists of two divisions: matrix and the filler fiber where the filler fibers are both nano and micro dimensions. Then, the MATLAB program was run including a barrier thickness between $(0.1-0.3)*r_d$.

The dimensionless effective thermal conductivity is given in Figures 6.1-6.4, for volume fraction values of $(0.1-0.3)$, when the dimensionless barrier thickness (t^+) is $(0.1-0.3) \times r_d$. It is seen that, increasing the volume fraction of the filler fiber inside the matrix increases the total effective thermal conductivity values. Since the model is hexagonal shape, it helped us to restrict the volume fraction of the filler fiber between 0.1 and 0.3. This is because, the first region in the analytical model does not contain the barrier and filler fiber regions. When $\beta=1$, both the filler fiber and the reinforcement fiber have the same thermal conductivity; the dimensionless effective thermal conductivity

becomes one, which is an expected value from the model. The minimum values are obtained when the volume fraction value of the filler fiber is 0.3 and the β (k_d/k_f) value is smaller than one.

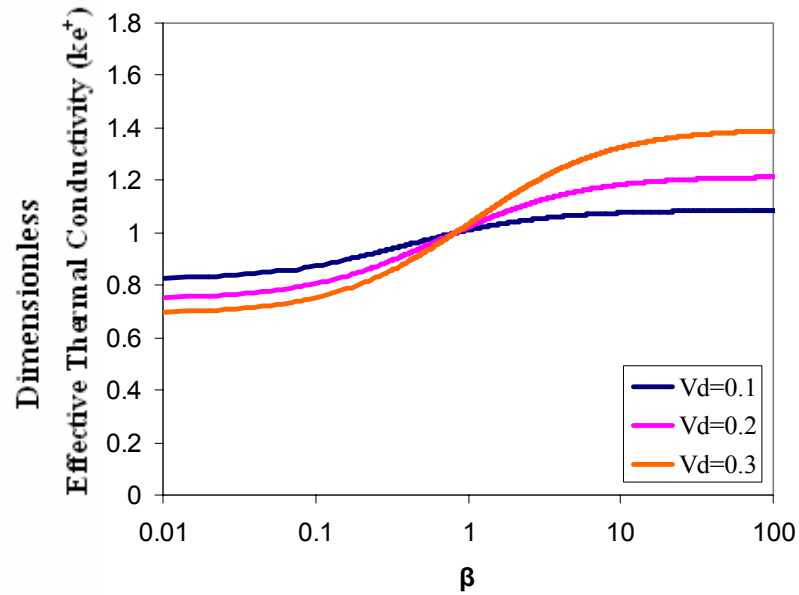


Figure 6.1. Change of dimensionless effective thermal conductivity with β for different V_d values, ($t=0$).

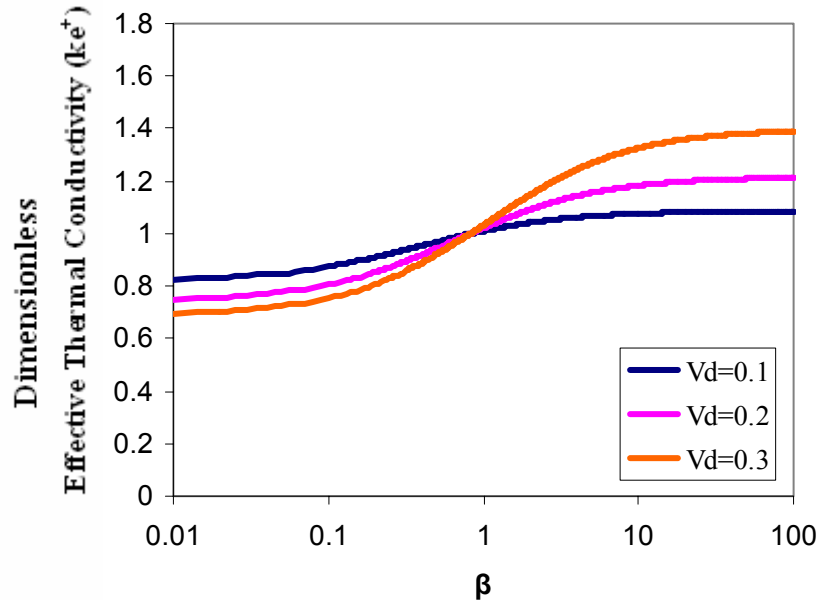


Figure 6.2. Change of dimensionless effective thermal conductivity with β for different V_d values, ($t=0.1 \times r_d$).

As seen from the Figures, when the barrier thickness is increased, the dimensionless effective thermal conductivity value (k_e) increases. This is because the barrier thermal conductivity values are taken as the average of the filler fiber and the reinforcement fiber's thermal conductivities.

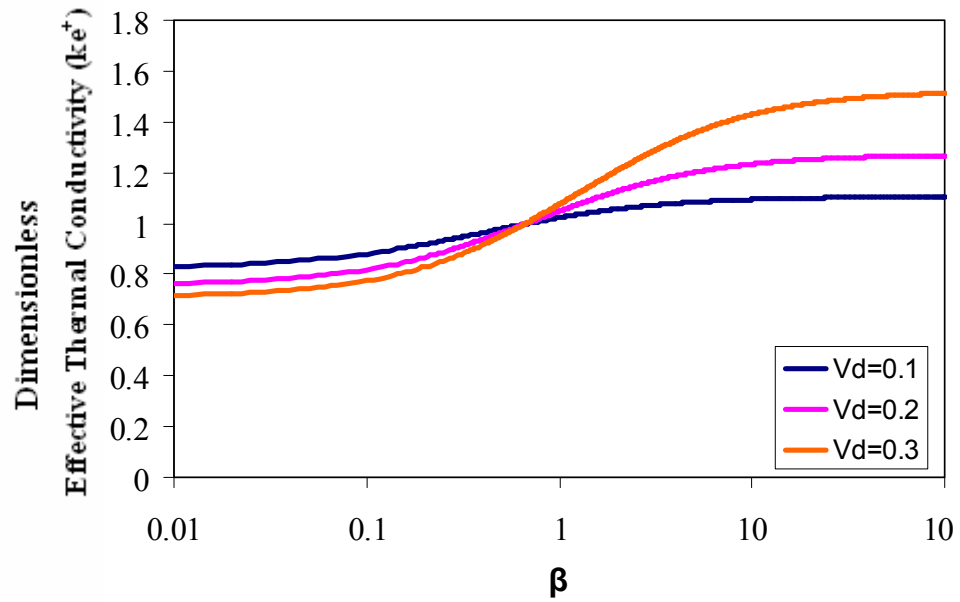


Figure 6.3. Change of dimensionless effective thermal conductivity with β for different V_d values, ($t=0.2 \times r_d$).

The maximum volume fraction value is taken as 0.3; from Figure 6.4, the maximum dimensionless effective thermal conductivity is around 1.7.

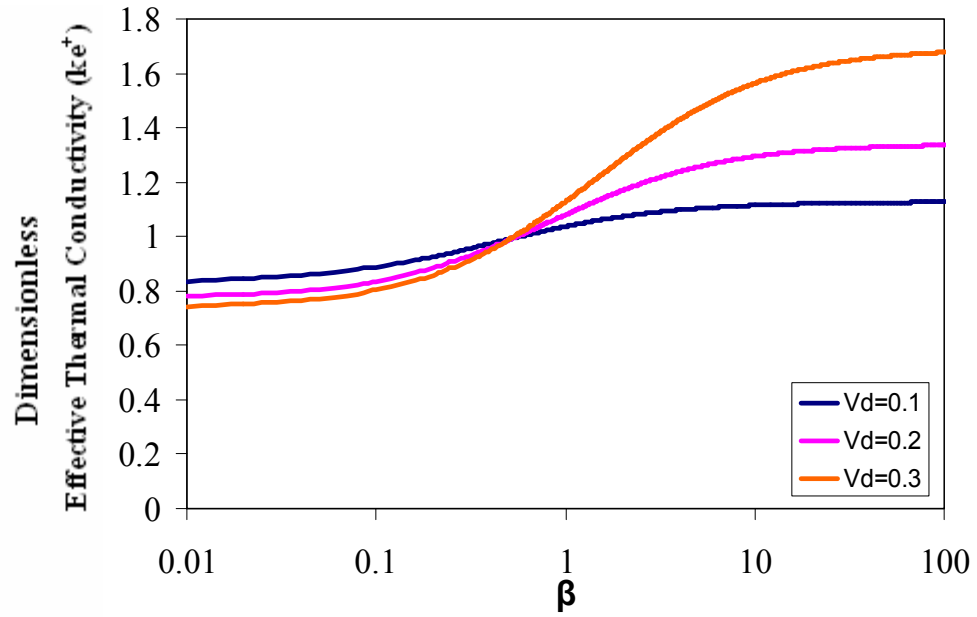


Figure 6.4. Change of dimensionless effective thermal conductivity with β for different V_d values, ($t=0.3 \times r_d$).

Figures 6.5-6.7 show the effect of barrier thickness on k_e . As explained earlier, the barrier region is taken as the third region in the hexagonal model. Since its thickness values do not show big difference, the k_e values are found to be close.

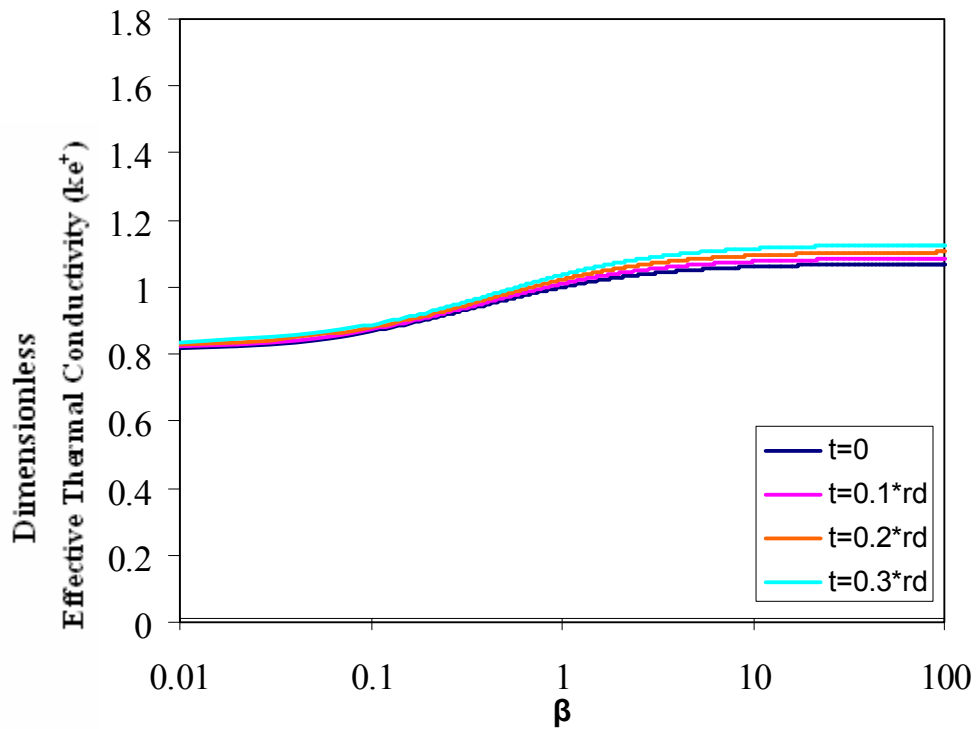


Figure 6.5. Effect of the barrier thickness on the dimensionless effective thermal conductivity, ($V_d=0.1$).

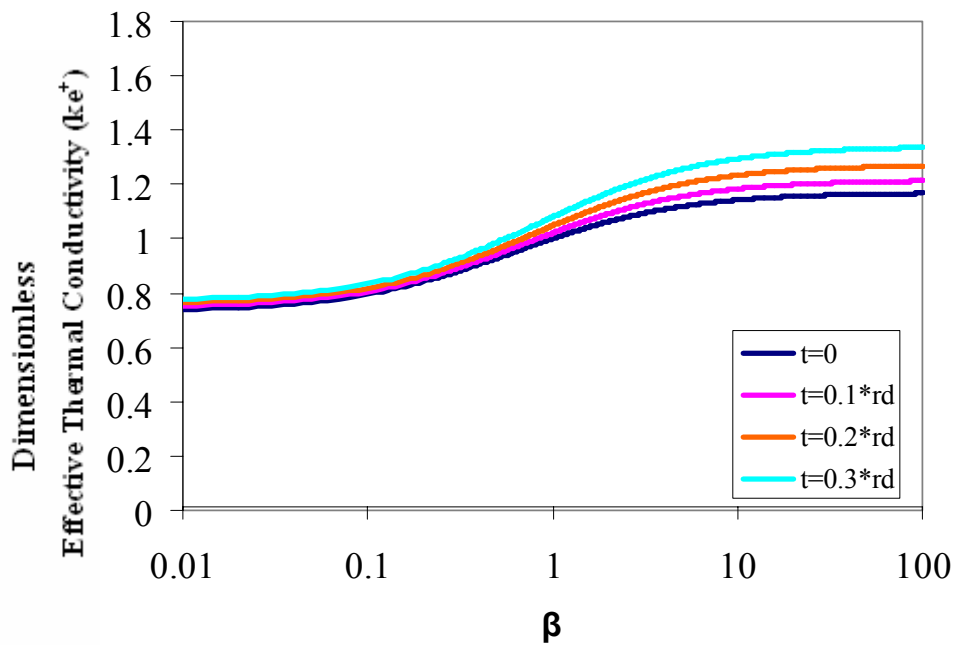


Figure 6.6. Effect of the barrier thickness on the dimensionless effective thermal conductivity, ($V_d=0.2$).

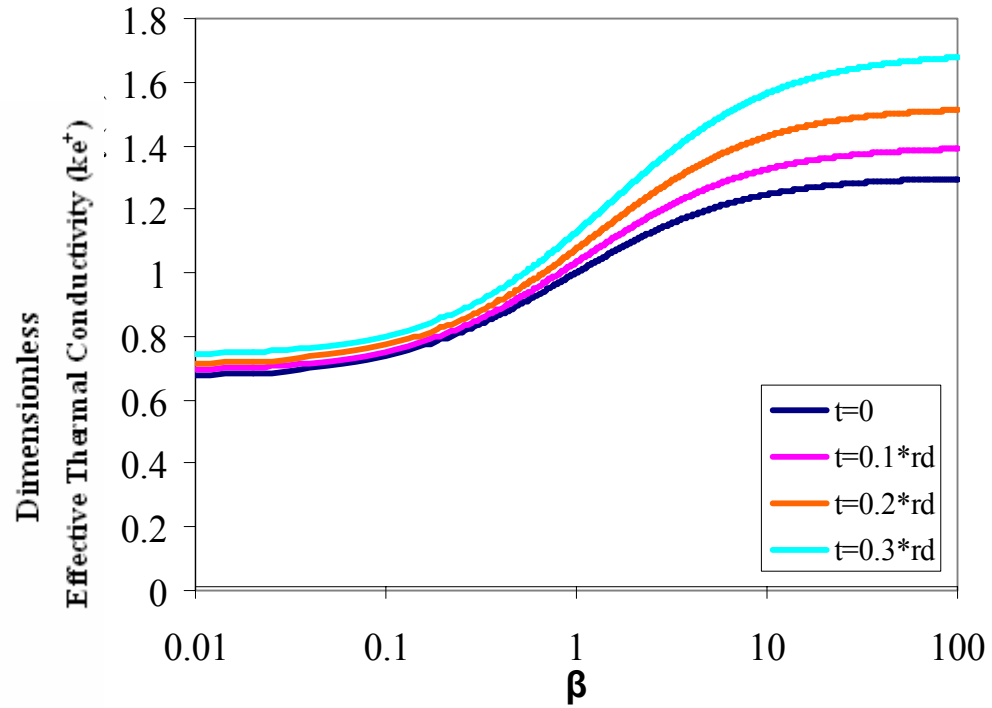


Figure 6.7. Effect of the barrier thickness on the dimensionless effective thermal conductivity, ($V_d=0.3$).

6.2. ANSYS Results

As reported by Islam [1], there are at least four different ways to calculate the dimensionless effective thermal conductivity by FEM. The first one, which is used in this study, is to apply temperature difference as boundary conditions to the left and right sides. The second is to apply both constant temperature and constant heat flux to the sides. The third is to apply constant heat flux to both sides and the last one is to apply temperature differences as boundary conditions at the horizontal boundaries.

Hexagonal unit cell was used with the ANSYS finite element program. The solution was obtained in different steps. The material properties were entered first,

followed by element type, then modeling the shape, and applying the boundary conditions. Finally, the results were obtained which is referred to as post procedure.

As the first step, to reduce the computer memory requirement, the symmetry effect was discussed. Since the problem is symmetrical around two planes of symmetry, only one quarter of the real volume specimen is considered in the model.

The GLUE command was used after establishing the parts of the model to give the initial composite properties to the shape. The domain is discretized into smaller regions both by PLANE35 and PLANE55 elements. PLANE35 has a triangle element and as a result it has one degree of freedom at the nodes. PLANE55 was used to model the areas which have small thickness especially the barrier region. An important thing to be noted here is that, although the layer elements are used in mechanical modeling to take the advantage of the composite structure, in heat transfer modeling, there are not so many available layered shell element types.

As material properties, only thermal conductivity was given and it is assumed to be constant and isotropic in every direction. After defining the material properties, and introducing to the areas, the meshing process starts. Meshing was done mostly automatically. The number of division was increased between the lines to get more sensitive results.

The boundary conditions for all the problems were taken similarly as applied constant temperatures to both left and right sides of the vertical line. For ANSYS, the effective thermal conductivity, when there is no heat flux applied and when the dimensions are $2a \times 2a$, is given for the unit cell as follows:

$$\left. \begin{aligned} \bar{q}_x &= \frac{1}{2a} \int_{-a}^a q_x(a, y) dy \\ \bar{T}_x &= \frac{\Delta T}{2a} \\ k_e &= -\frac{\bar{q}_x \cdot 2a}{\Delta T} \end{aligned} \right\} \quad (6.1)$$

where,

\bar{q}_x : average heat flux value in x direction,

a : length of the unit cell,

ΔT : temperature gradient,

k_e : effective thermal conductivity,

\bar{T}_x : average temperature value in x direction.

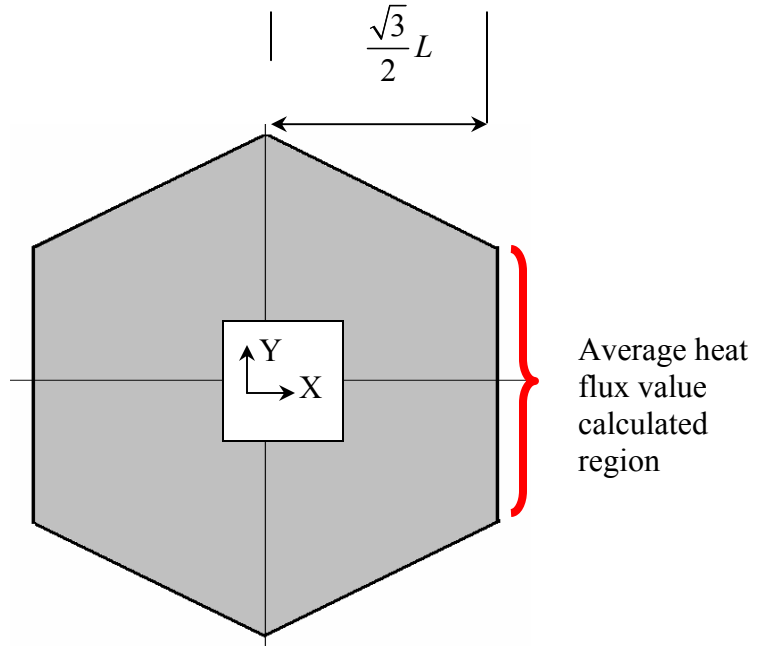


Figure 6.8. k_e^+ calculations for the hexagonal unit cell in ANSYS

For the hexagonal cell (Figure 6.8), the average heat flux in the X direction for the first region;

$$\bar{q}_x = \frac{\sqrt{3}}{2} L \int_0^{\frac{L}{2}} q_x \left(\frac{\sqrt{3}}{2} L, y \right) dy \quad (6.2)$$

The dimensionless effective thermal conductivity can be calculated as;

$$k_e^+ = - \frac{\bar{q}_x \cdot \frac{\sqrt{3}}{2} L}{\Delta T} \quad (6.3)$$

- Temperature was applied for the left side as -1°C and for the right side as 1°C .
- Thermal conductivity of the main fiber was taken as 10 W/mK and only the thermal conductivities of filler fiber and barrier were changed.

- k_b is taken as the average of the total thermal conductivities.

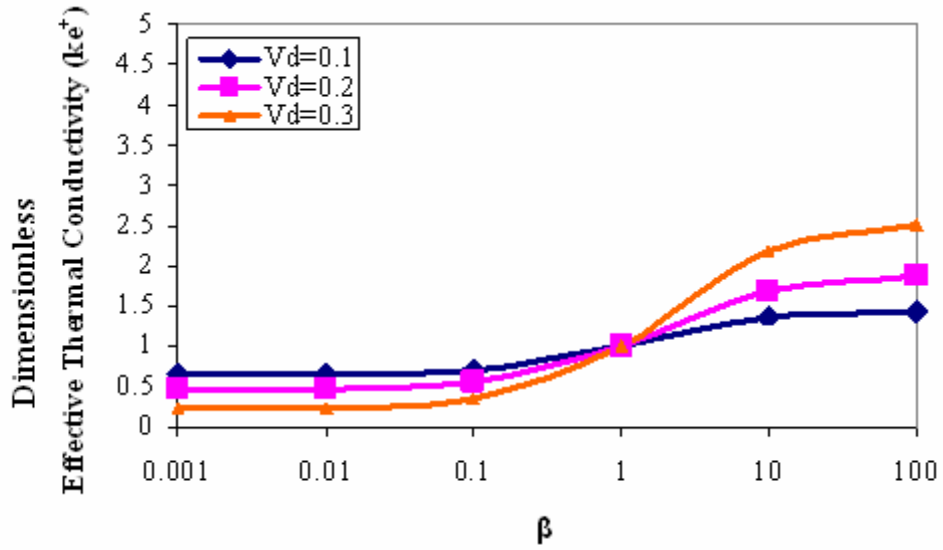


Figure 6.9. Dimensionless effective thermal conductivity ($t=0$).

In Figure 6.9, the k_e^+ value was compared when the barrier thickness is zero for different filler fiber volume fractions. The k_e^+ value is also calculated when there is a barrier thickness and the results are shown in Figures 6.10-6.12.

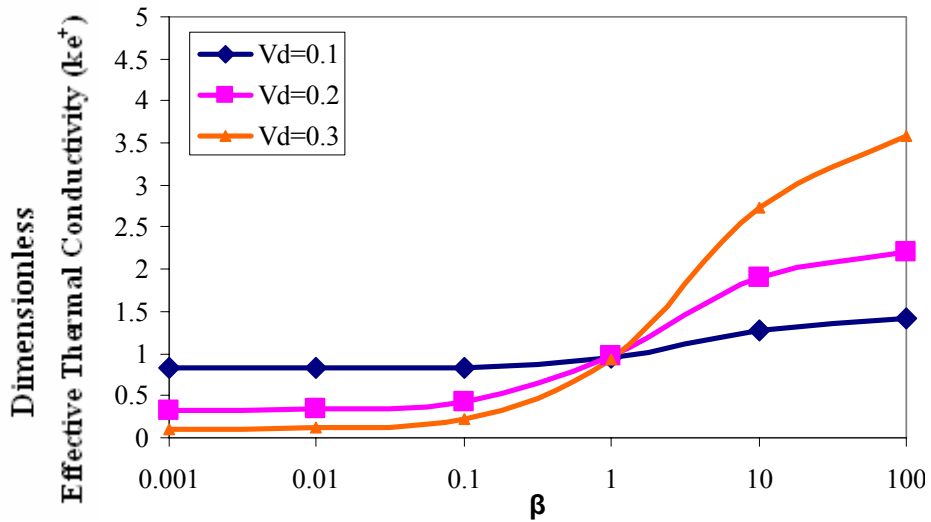


Figure 6.10. Dimensionless effective thermal conductivity ($t=0.1 \times r_d$).

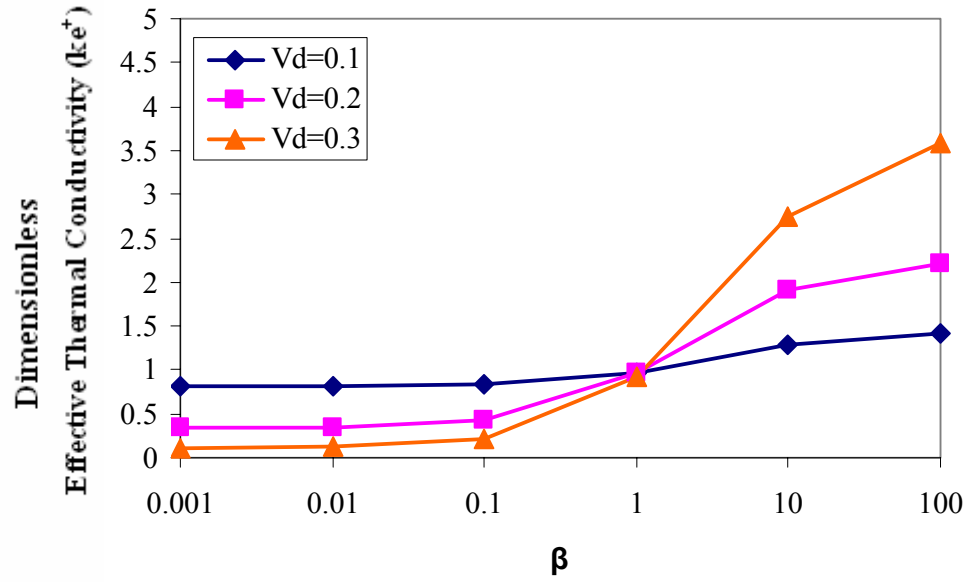


Figure 6.11. Dimensionless effective thermal conductivity ($t = 0.2 \times r_d$).

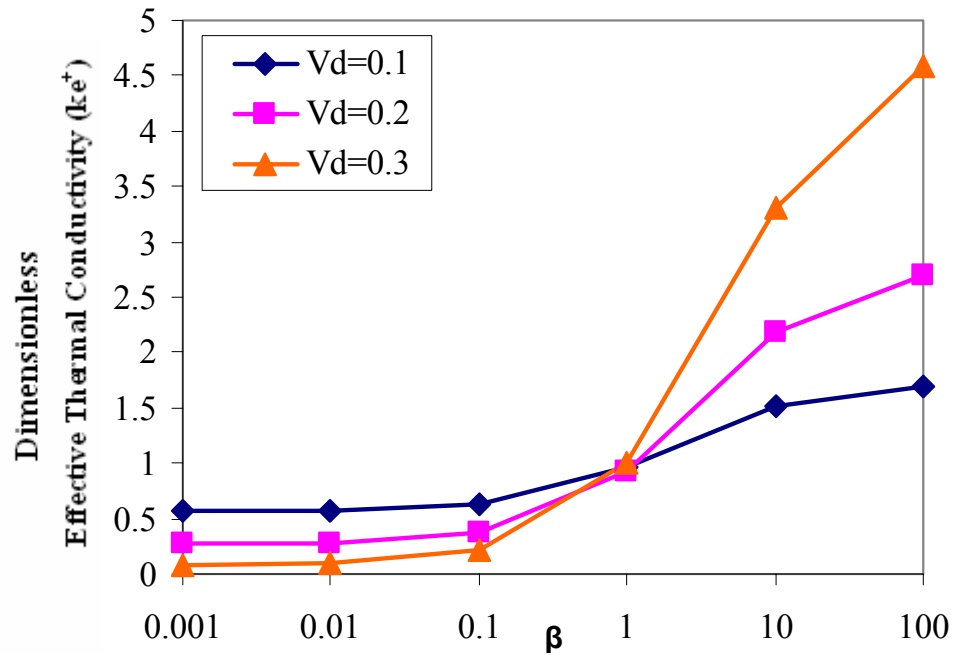


Figure 6.12. Dimensionless effective thermal conductivity ($t = 0.3 \times r_d$).

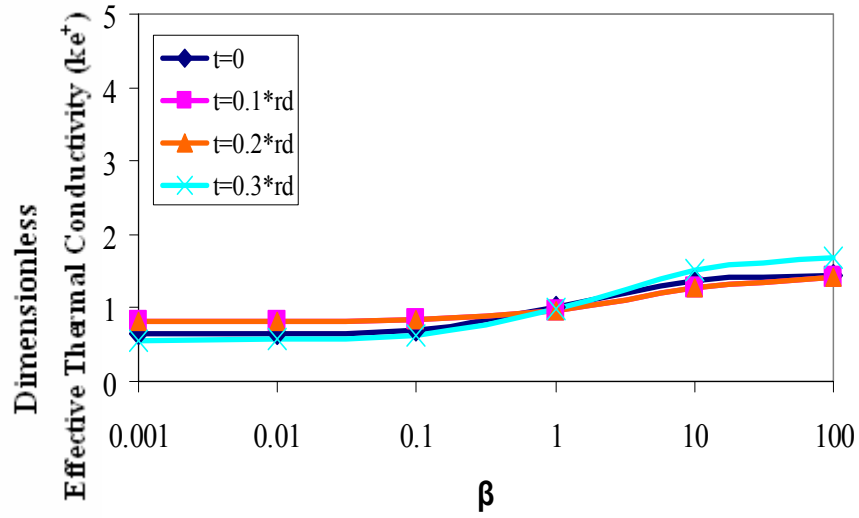


Figure 6.13. Dimensionless effective thermal conductivity ($V_d=0.1$).

Next, the effect of the barrier thickness is discussed when there is a constant V_d .

Compared to the MATLAB results, in ANSYS, the results showed more difference (Figures 6.13 - 6.15).

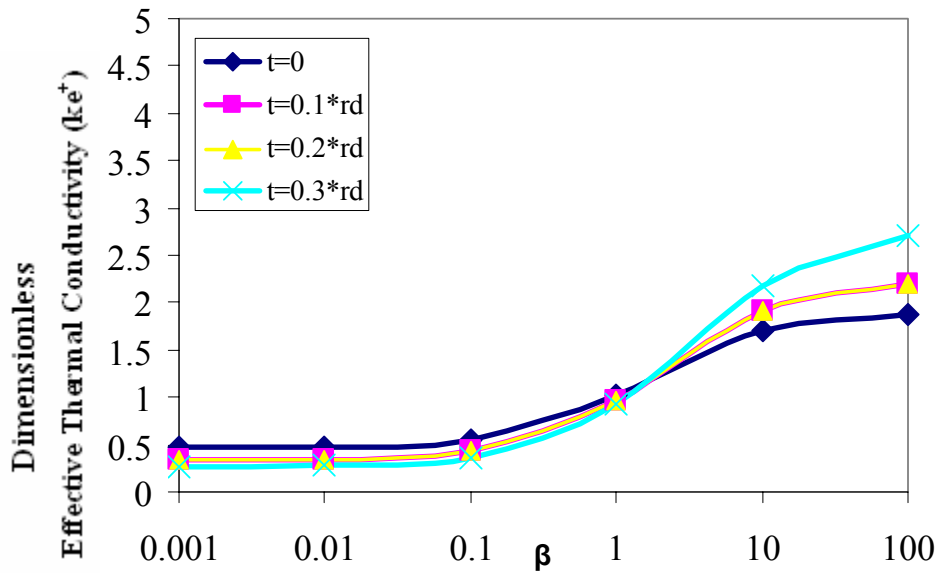


Figure 6.14. Dimensionless effective thermal conductivity ($V_d=0.2$).

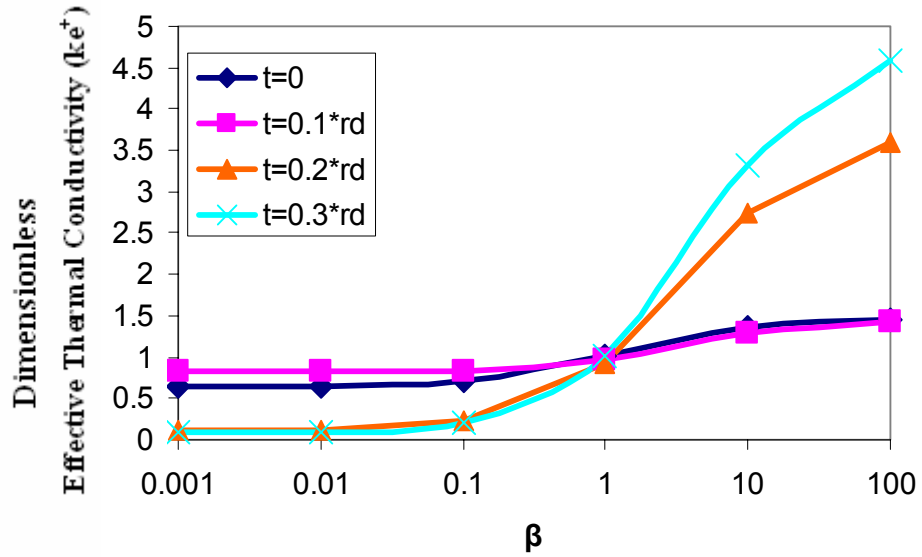


Figure 6.15. Dimensionless effective thermal conductivity ($V_d=0.3$).

The Rule of mixtures has been used for a long time to define the dimensionless effective thermal conductivity values when there is no thickness (Table 6.1 and Figure 6.16). The Rule of Mixtures can be described as;

$$k_c = vk_f + (1-v)k_m$$

where;

k_c : composite's thermal conductivity,

k_f : filler fiber's thermal conductivity,

k_m : matrix's thermal conductivity,

v : volume fraction of the filler fiber.

The Rule of Mixtures results were compared to ANSYS and MATLAB results in Figures 6.17-6.19. The MATLAB and ANSYS results showed much similarity compared to the Rule of Mixtures. The comparison with the Rule of Mixtures results was limited to

only when there is no barrier thickness. It was found that although the filler fiber and the matrix have similar thermal conductivity values, when the difference between the thermal conductivities increases, the difference between the dimensionless effective thermal conductivity values also increases.

Table 6.1. Dimensionless effective thermal conductivity by Rule of Mixtures.

	$\beta(k_d/k_f)$	Volume fraction of the filler fiber (V_d)		
		0.1	0.2	0.3
Dimensionless Effective Thermal Conductivity (k_e^+)	0.001	0.9001	0.8002	0.7003
	0.01	0.901	0.802	0.703
	0.1	0.91	0.82	0.73
	1	1	1	1
	10	1.9	2.8	3.7
	100	10.9	20.8	30.7

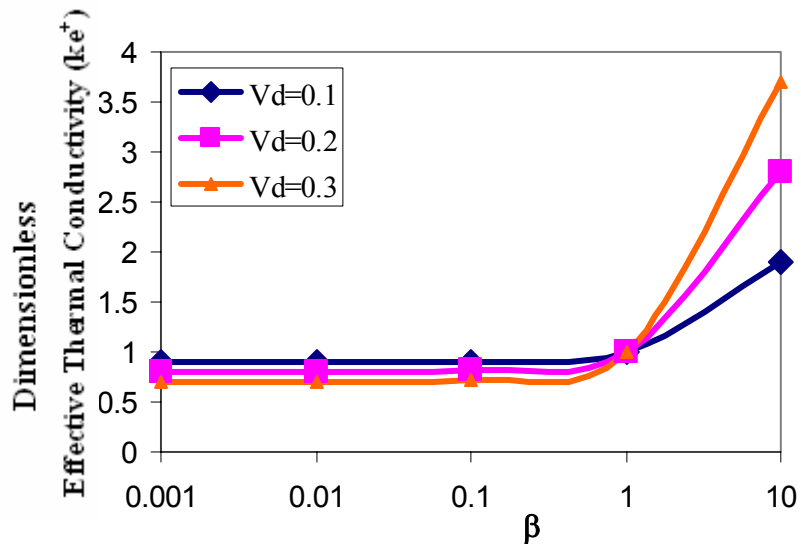


Figure 6.16. Dimensionless effective thermal conductivity by the Rule of Mixtures

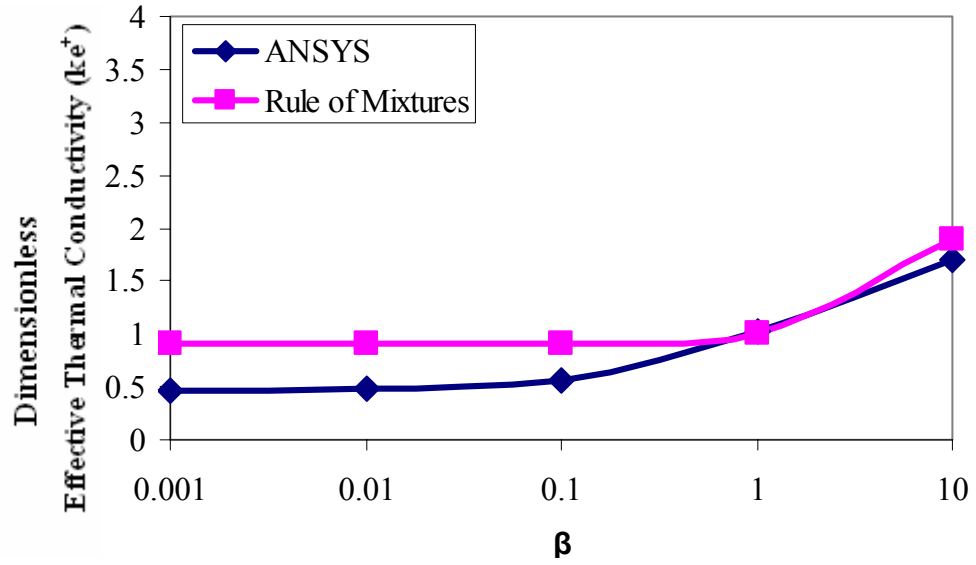


Figure 6.17. Dimensionless effective thermal conductivity comparison between the ANSYS and Rule of Mixtures ($V_d=0.2$).

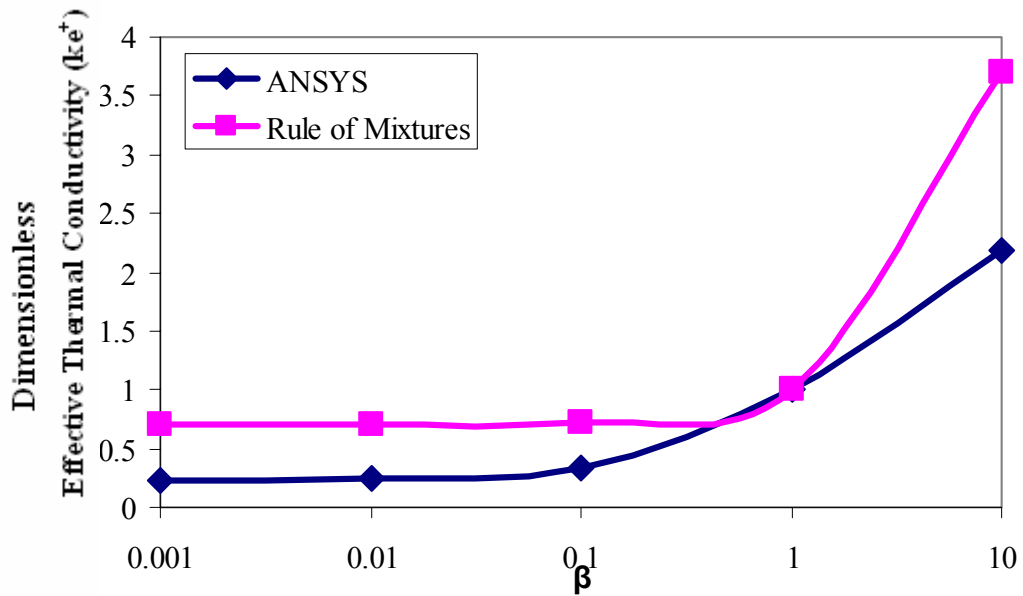


Figure 6.18. Dimensionless effective thermal conductivity comparison between the ANSYS and Rule of Mixtures ($V_d=0.3$).

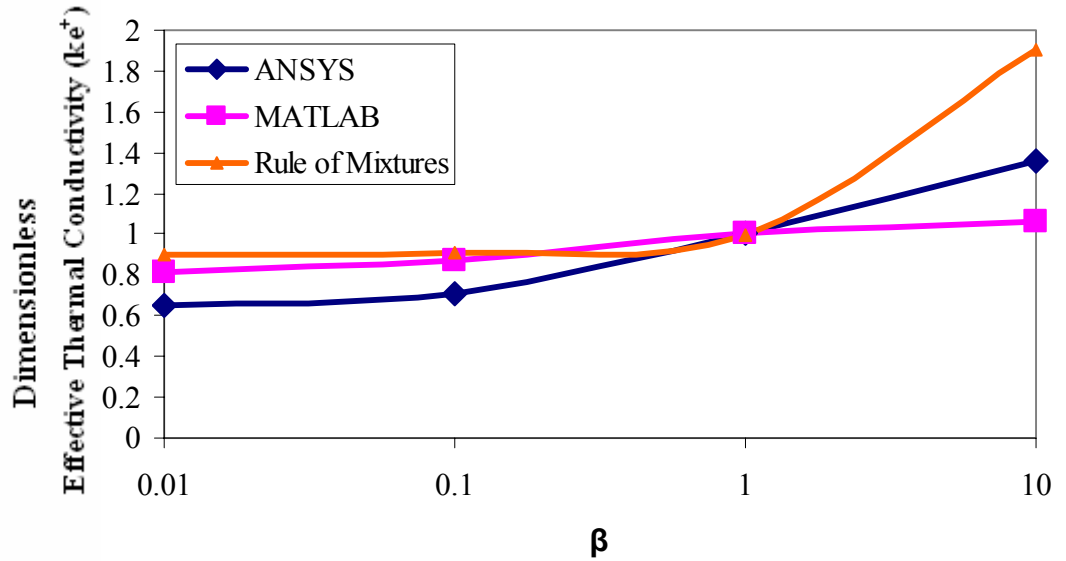


Figure 6.19. Comparison of the dimensionless effective thermal conductivity among the ANSYS, MATLAB and Rule of Mixtures ($t=0$ and $V_d=0.1$).

When the barrier thickness is zero, the barrier region becomes part of the matrix, thus only two different thermal conductivity values (for matrix and filler fiber) were given for the model. As stated earlier, under the steady-state conditions, the boundary conditions were applied to the left and right side of the model as $-1\text{ }^\circ\text{C}$ and $1\text{ }^\circ\text{C}$ respectively.

Figure 6.20 shows the meshing of the hexagonal unit cell. When the model becomes smaller, the dimensions of the triangle elements also become smaller. The different color distribution is the result of the same element type but different material properties. Two different material properties were introduced to the model: for cylindrical part and for the main fiber part.

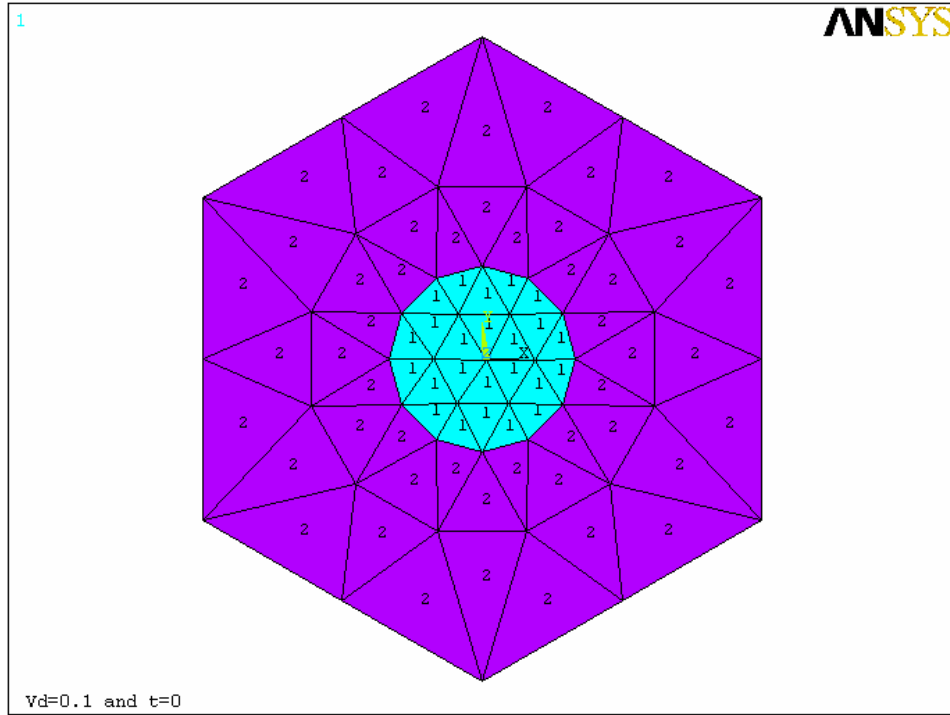


Figure 6.20. Meshing for the hexagonal model

Figure 6.21 shows the temperature distribution of the hexagonal when the thermal conductivity of the filler fiber (k_d) is 1000 W/mK and the thermal conductivity of the main fiber (k_f) is 10 W/mK. Since the boundary conditions are -1°C to the left side and 1°C to the right side and all the force was applied in the X direction, the temperature distribution is expected to increase closer to the filler fiber since it has bigger thermal conductivity.

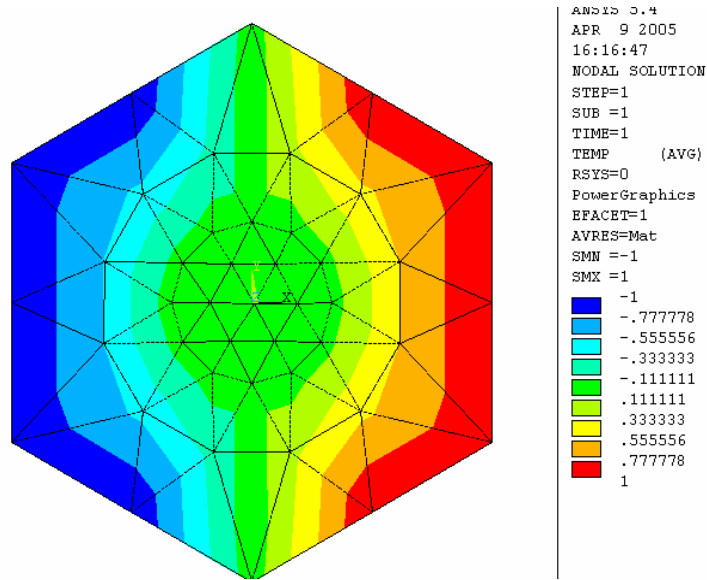


Figure 6.21. Temperature distribution of the hexagonal unit cell ($t=0$ and $V_d=0.1$).

Figure 6.22 shows the heat flux variation in the X direction under the similar conditions of Figure 6.21. Figure 6.23 shows the vectorel form of the heat flux variation. It is important to note that, there is no barrier layer for the results up to Figure 6.28.

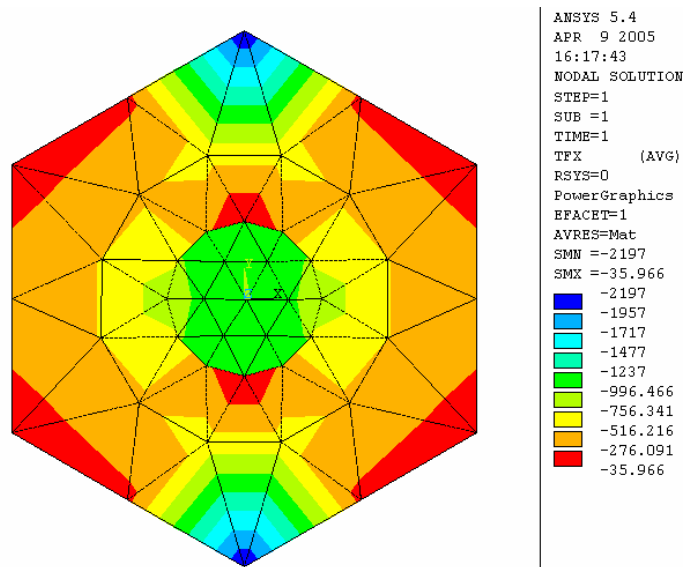


Figure 6.22. Heat flux distribution in the X direction of the hexagonal unit cell ($t=0$ and

$V_d=0.1$).

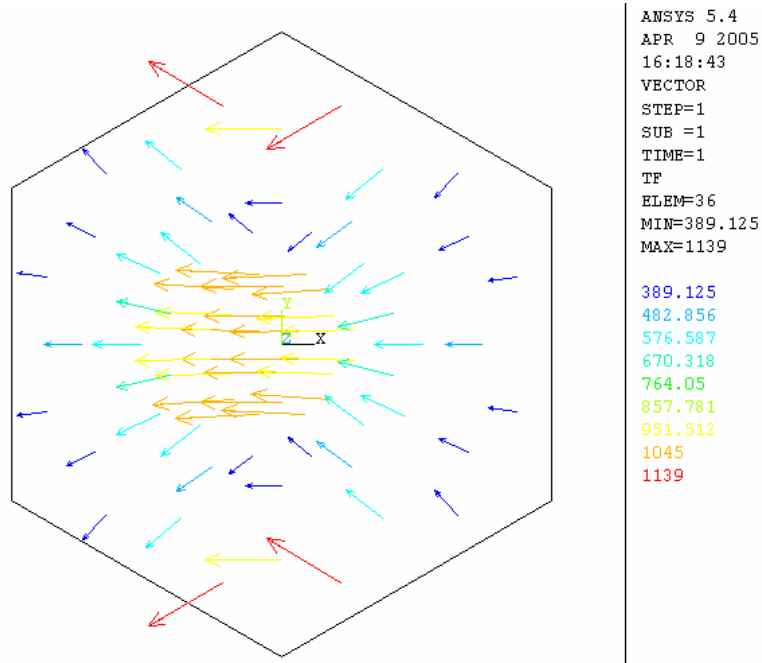


Figure 6.23. Heat flux vector in the X direction of the hexagonal unit cell ($t=0$ and $V_d = 0.1$).

In Figure 6.24, thermal gradient in the X direction is given. At the top and bottom, thermal gradient has maximum values, since no boundary conditions were applied to these edges.

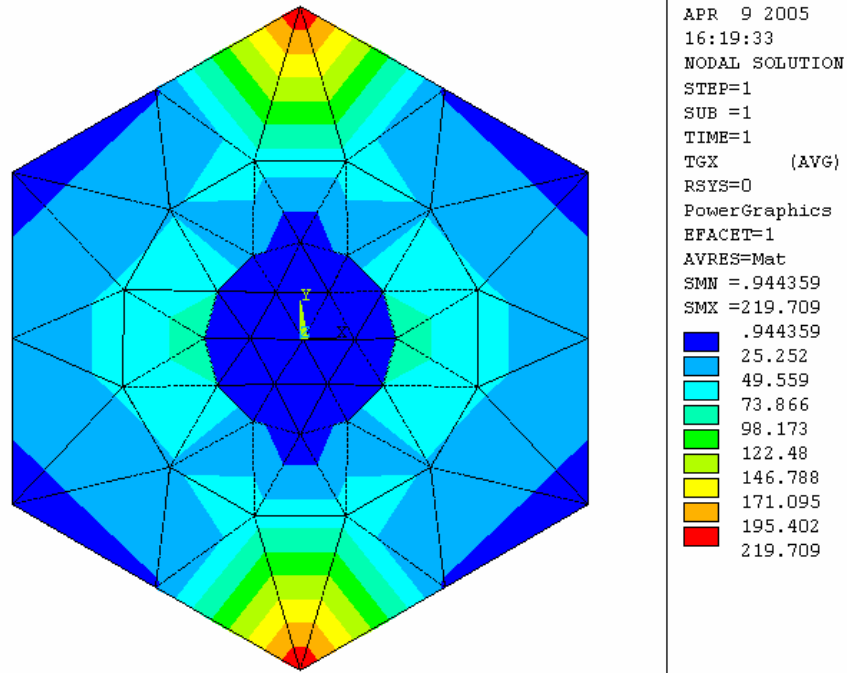


Figure 6.24. Thermal gradient in the X direction of the hexagonal unit cell ($t=0$ and $(V_d=0.1, k_d=1000, k_f=10)$).

In Figures 6.25 and 6.26, k_d is decreased to 0.01 W/mK and the other factors are kept the same. Heat flux and thermal gradient values showed difference especially closer to the filler fiber area.

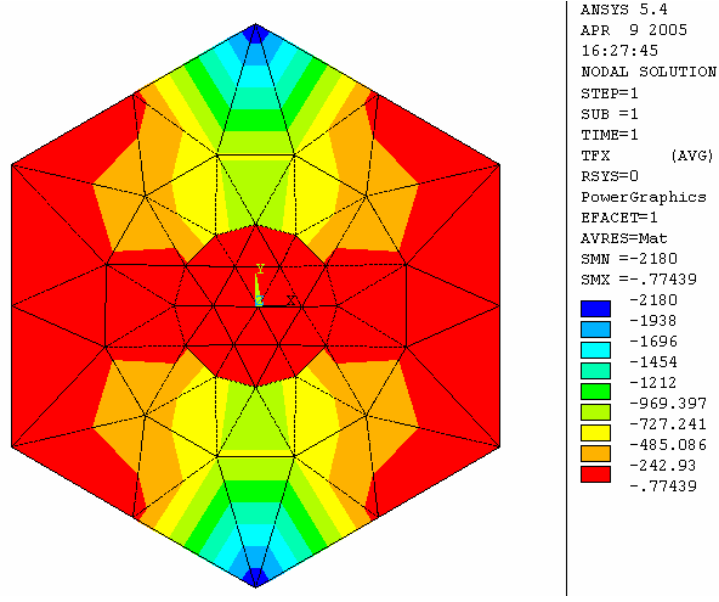


Figure 6.25. Heat flux in the X direction of the hexagonal unit cell ($t=0, V_d=0.1, k_d=0.01, k_f=10$).

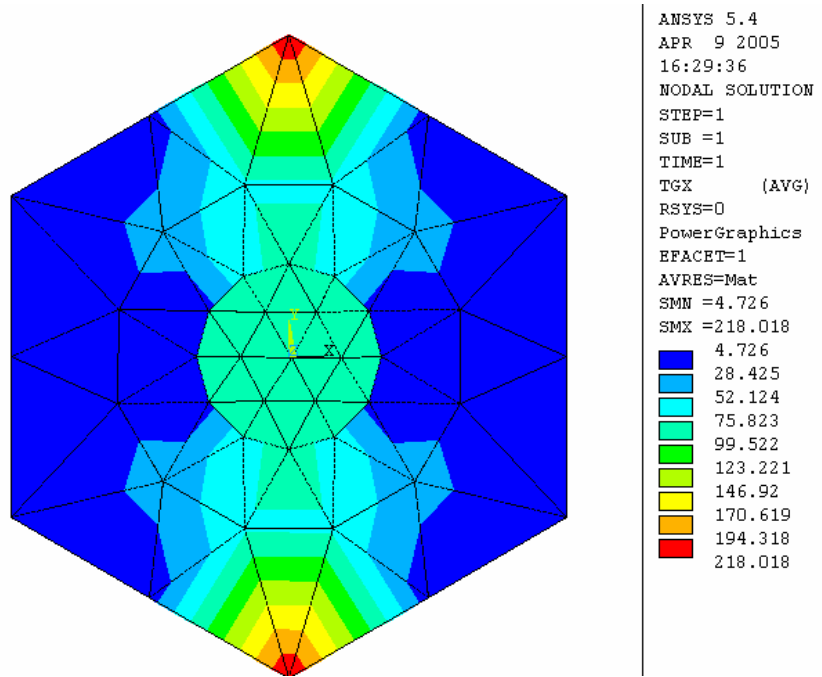


Figure 6.26. Thermal gradient in the X direction of the hexagonal unit cell ($t=0, V_d=0.1, k_d=0.01, k_f=10$).

Temperature difference is the result of the boundary conditions and the thermal conductivity of the filler fiber and the matrix. Since the boundary conditions were applied in only through the X direction, the heat flux variation in Y direction is found to be much smaller than the X direction. The vectors show the direction of the heat transfer inside the model. If it is negative, it means that the direction of the heat flow is not to the model direction. Also, it is important to note that since the model is 2-D, heat flux was not applied as boundary conditions.

Since the interface region is, under normal conditions, the result of improper parameters such as voids, cracks, and the like, the barrier layer is modeled to have small thickness value, i.e. $0.1 \times r_d$, $0.2 \times r_d$ and $0.3 \times r_d$ where r_d is the radius of the filler fiber. The reason why the thickness is to be taken bigger than the size which was taken for MATLAB is because of the sensitivity of the ANSYS. Since the main model is much bigger than the barrier region, the ANSYS results became closer to the case where there is no barrier layer. The analysis showed that, the thickness has to be considered at least bigger than $0.1 \times r_d$.

Figures 6.27-6.30 show the results obtained to determine the barrier effect on the dimensionless effective thermal conductivity. The thermal conductivity of the barrier is taken as the average of the filler fiber and matrix's thermal conductivity. Thermal conductivity of the matrix is taken constant as 10W/mK. When the volume fraction of the filler fiber is increased, its effects on the thermal conductivity are shown in Figure 6.31-6.33.

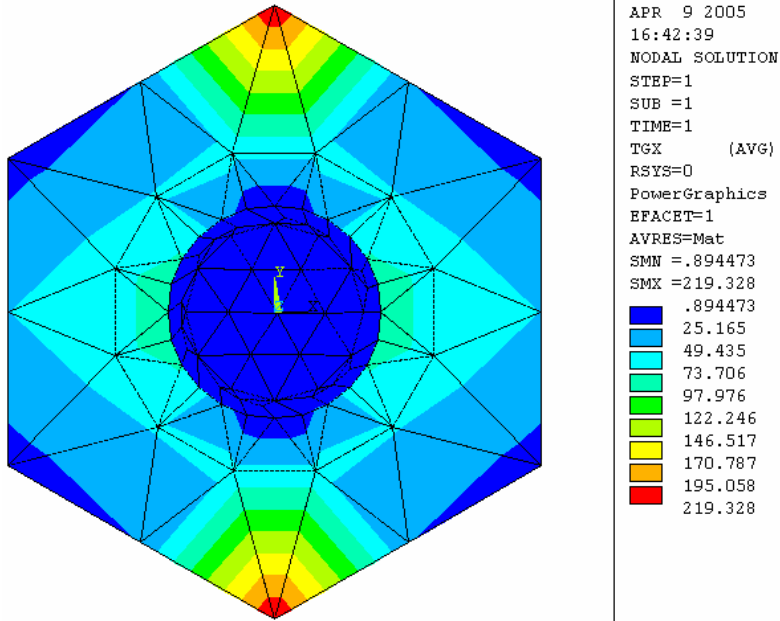


Figure 6.27. Thermal gradient in the X direction of the hexagonal unit cell ($t=0.1 \times r_d$ and $V_d=0.1$).

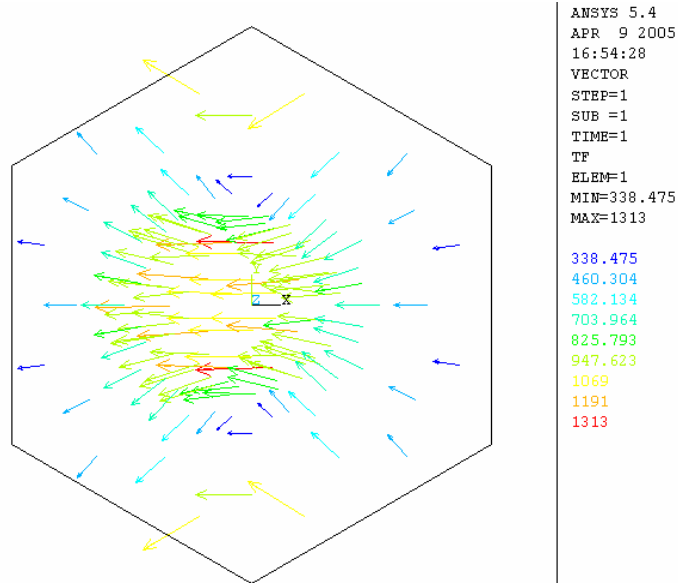


Figure 6.28. Thermal gradient vector in the X direction of the hexagonal unit cell ($t=0.1 \times r_d$ and $V_d=0.1$).

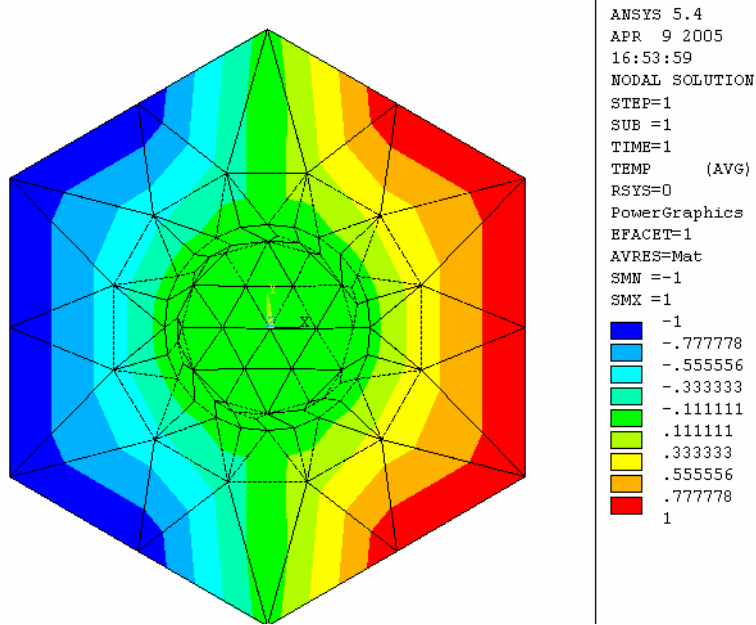


Figure 6.29. Thermal gradient in the X direction of the hexagonal unit cell ($t=0.2 \times r_d$ and $V_d=0.1$).

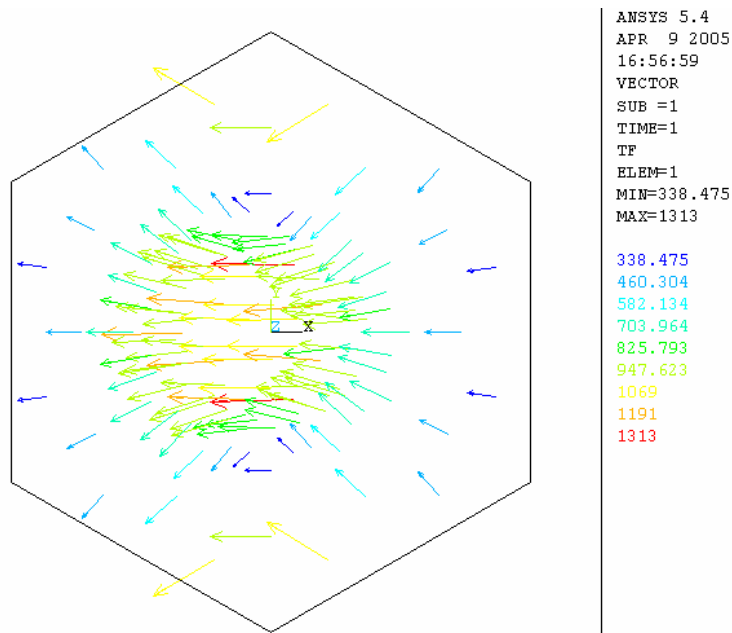


Figure 6.30. Thermal gradient in the X direction of the hexagonal unit cell ($t=0.1 \times r_d$ and $V_d=0.1$).

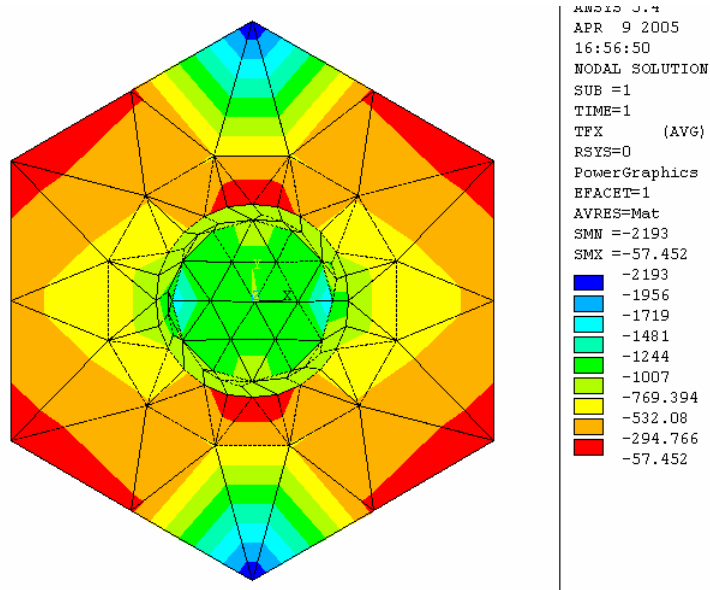


Figure 6.31. Heat flux in the X direction of the hexagonal unit cell ($t=0.2 \times r_d$ and $V_d=0.2$).

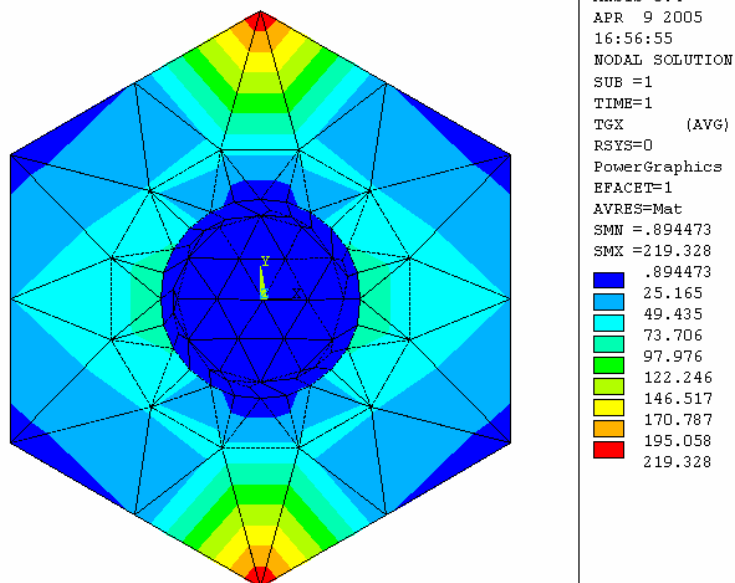


Figure 6.32. Temperature gradient in the X direction of the hexagonal unit cell ($t=0.2 \times r_d$ and $V_d=0.2$).

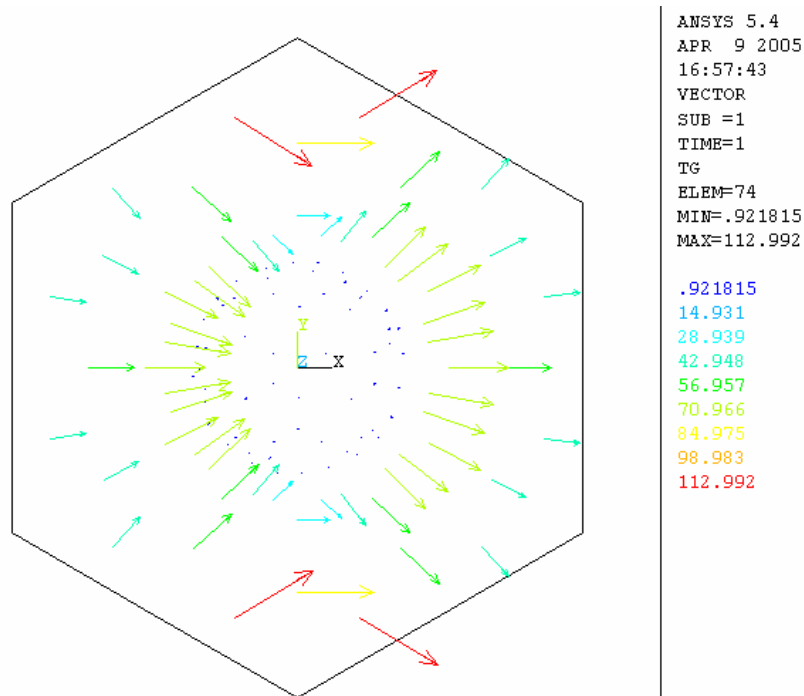


Figure 6.33. Temperature distribution in the X direction of the hexagonal unit cell ($t=0.2 \times r_d$ and $V_d=0.2$).

6.3. SEM Results

Scanning electron microscope (SEM) was used to determine the dimensions of the electrospun fibers. The SEM study was done after gold coating in the Biology Department.

First PVA solutions were prepared with 10, 12 and 15 wt% PVA. By using the electrospinning method, fiber web was manufactured. The effect of electrospinning time was also investigated (Figures 6.34-6.35). A continuous web form developed after 1-2 hours, which gave us enough area and thickness to pull the electrospun based fiber web from the collector.



Figure 6.34. Web formation after 1 second of spinning.



Figure 6.35. Web formation after 24 seconds of spinning.

The web was placed on a pan for coating. To save time, the stub was divided into four parts as shown in Figure 6.36. To avoid the melting problem that can be caused by SEM electron bombing, the coating time was increased to 4 minutes.

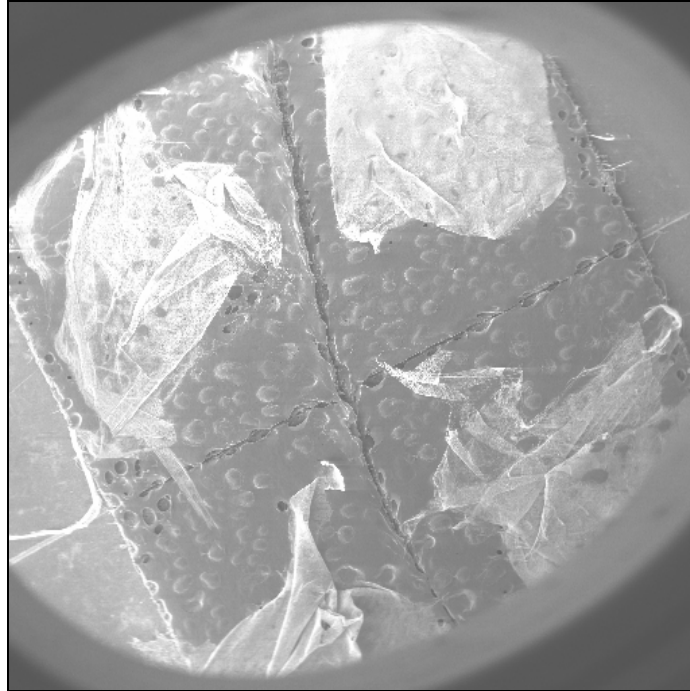


Figure 6.36. SEM pan

The effect of concentration on the fiber size can be seen in Table 6.2. When the concentration is increased, the fiber size also increases. 10, 12 and 15 wt % PVA concentrations were used to compare the fiber sizes. When the concentration is increased, it also affected the uniformity of the fiber. For 10 wt % PVA concentration, the fiber diameter was around 410 nm, for 12 wt % PVA concentration, it was around 425 nm and lastly for 15 wt % PVA, it was 563 nm.

Table 6.2. Fiber dimensions under SEM.

	Fiber Diameter (nm)			
	Section 1	Section 2	Section 3	Section 4
1st sample (10 wt %)	158	100	100	176
	280	158	194	210
	310	229	229	280
	350	280	270	310
	380	320	280	520
	494	370	282	810
	700	380	350	1376
	758	458	410	
	880	547	458	
Average	478.89	315.77	321.63	526
Total average	410.57			
2nd sample (12wt %)	Fiber Diameter(nm)			
	Section 1	Section 2	Section 3	Section 4
	490	280	490	560
	420	600	600	700
	280	450	420	200
	317	380	300	317
Average	376.75	427.5	452.5	444.25
Total average	425.25			
3rd sample (15wt %)	Fiber Diameter(nm)			
	Section 1	Section 2	Section 3	Section 4
	420	420	1830	940
	310	630	700	200
	520	280	280	
	350	247	560	
	280	560		
	560	400		
	490			
Average	418.57	422.83	842.5	570
Total average	563.47			

Figures 6.37-6.41 are from the SEM results. As seen from the figures, fibers are not aligned. When the magnification is increased, fiber bundles were observed which were originally thought as the bigger radius fibers with small magnification (Figure 6.38).

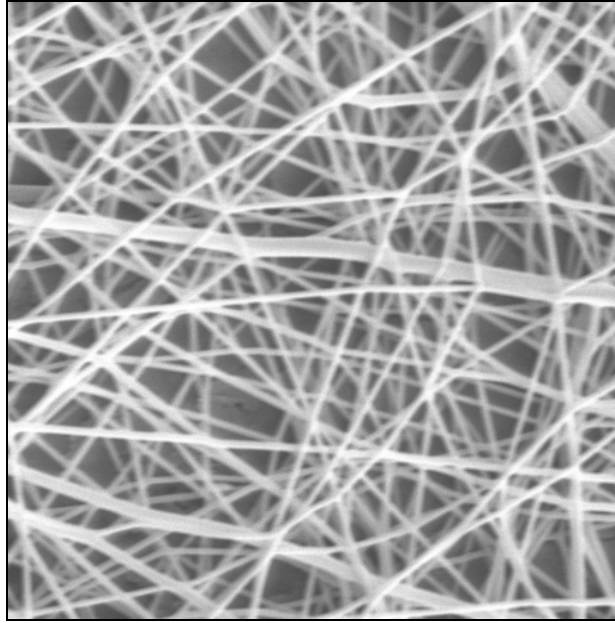


Figure 6.37. SEM image of nanofiber based web (10 wt. % PVA, 3000x).

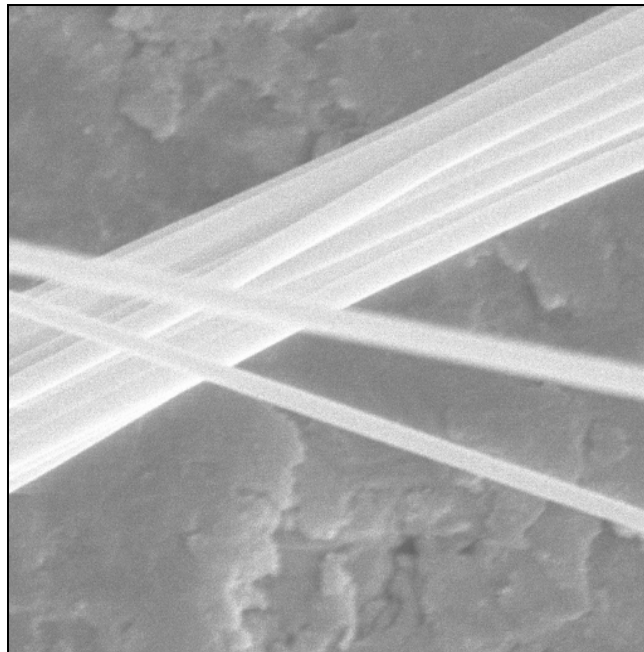


Figure 6.38. SEM image of nanofiber bundle (12 wt.% PVA, 10000x).

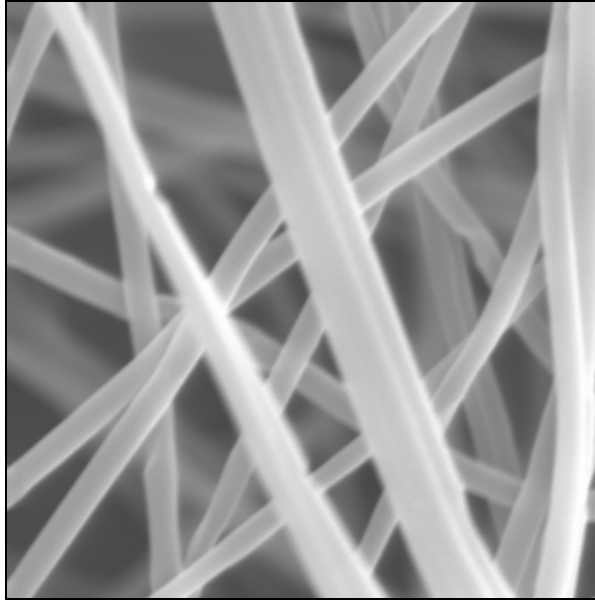


Figure 6.39. SEM image of nanofibers (12 wt. % PVA, 10000x).

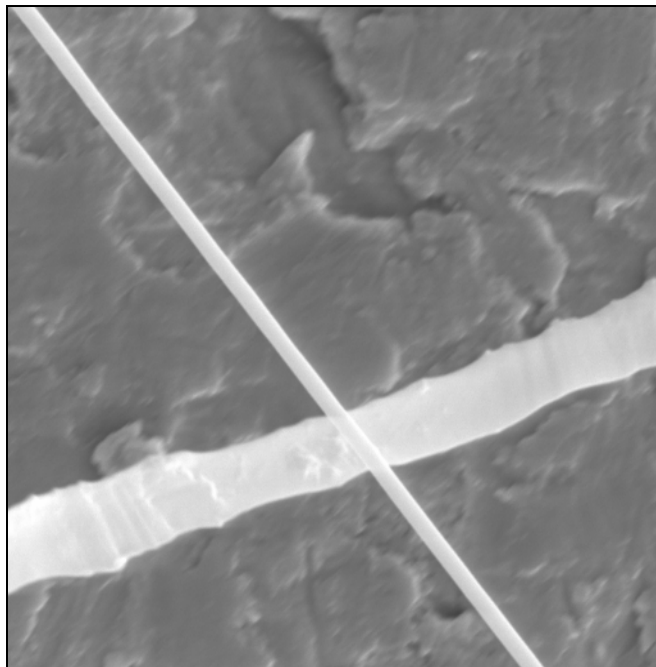


Figure 6.40. Variety of fiber size (15 wt. % PVA, 3000x).



Figure 6.41. Single fiber (12wt. % PVA, 10000x).

After manufacturing of pure PVA fibers, the Laponite® powder was added to the PVA solution. Figure 6.42 shows SEM result when the Laponite® and PVA are prepared together. When the Laponite® is added to the solution, it may cause a slub in the fiber, as shown in the figure.

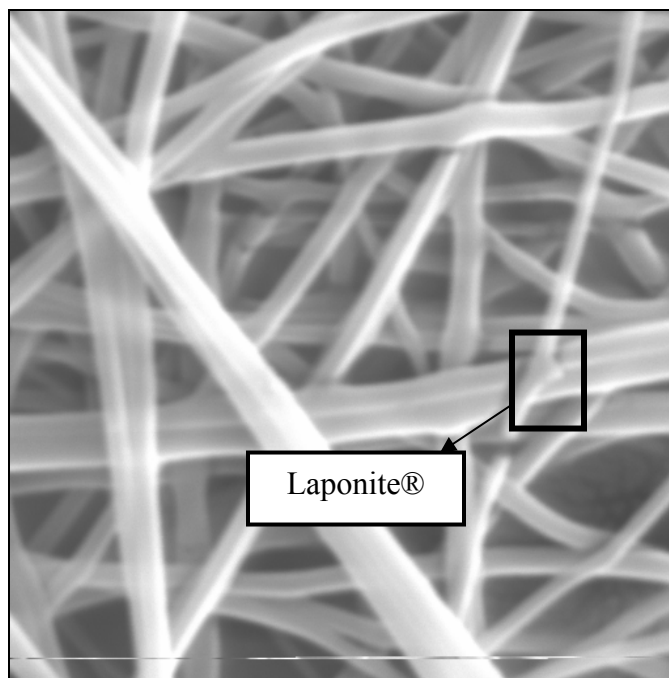


Figure 6.42. PVA and Laponite® under SEM (12 wt PVA + 5 wt % Laponite®, 10000x).

One of the problems to be mentioned in electrospinning is the beading problem (Figure 6.43). To obtain a uniform web, the beading needs to be reduced. After using different concentration values of PVA, the 12 wt % was decided to be used for the rest of the study, since it produced the least amount of beading. Beading can be affected from surface tension of the web form. When the viscosity increased, it causes less beading problem (Figure 6.44).

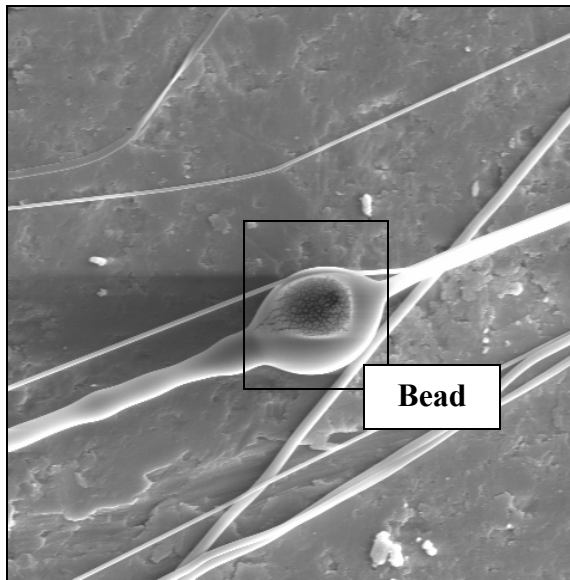


Figure 6.43. Bead problem in electrospinning (15 wt% PVA, 1000x).

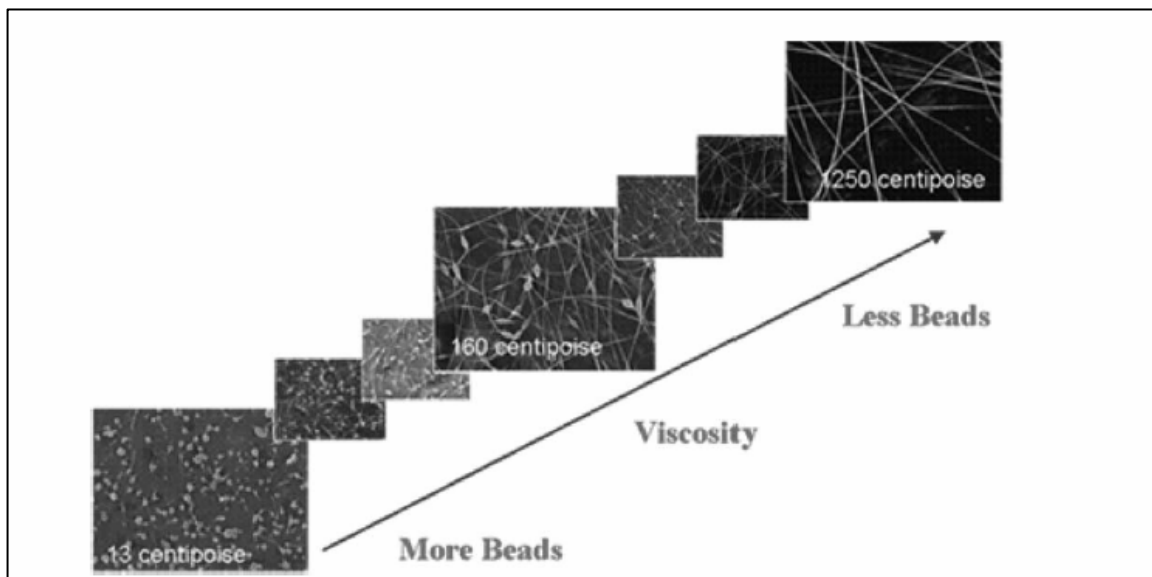


Figure 6.44. Bead formation [2].

6.4. Tensile Testing

Mechanical properties are important to measure in terms of stability. Water was used as a solvent which also acts as a plasticizer and causes humidity inside the material. This, in turn, causes the elongation and tear strength to increase. The more plasticizer used, the more elongation and tear strength expected. However, tensile strength is decreased with plasticizer.

Tensile strength testing was done to find out the strength of the manufactured yarns. 12 wt % PVA was used to manufacture fibers. Then a piece of yarn was produced by twisting ten different bundles of fibers. The yarn pieces were made from fibers with similar shape and dimensions. Using the Instron machine, the breaking tensile strength of the yarns was measured. Before measuring, the specimen was vertically aligned to avoid the side loading or bending moments.

For a representative yarn, the maximum load was 0.246 kgf and the displacement was around 12 mm (Figure 6.45).

The properties of the yarn:

Linear Density: 300.0 den

Spec gauge len: 15.0 mm

Ext. gauge len: 101.6 mm

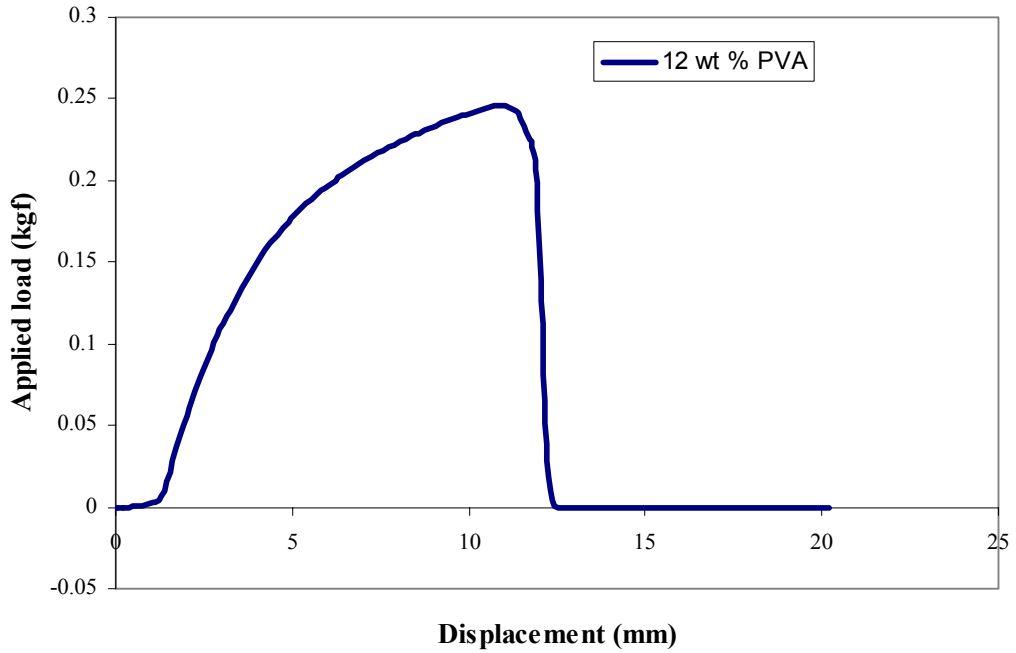


Figure 6.45. Load-elongation curve for nano-micro fiber based yarn.

Figure 6.46 shows the comparison of several yarns for tensile strength.

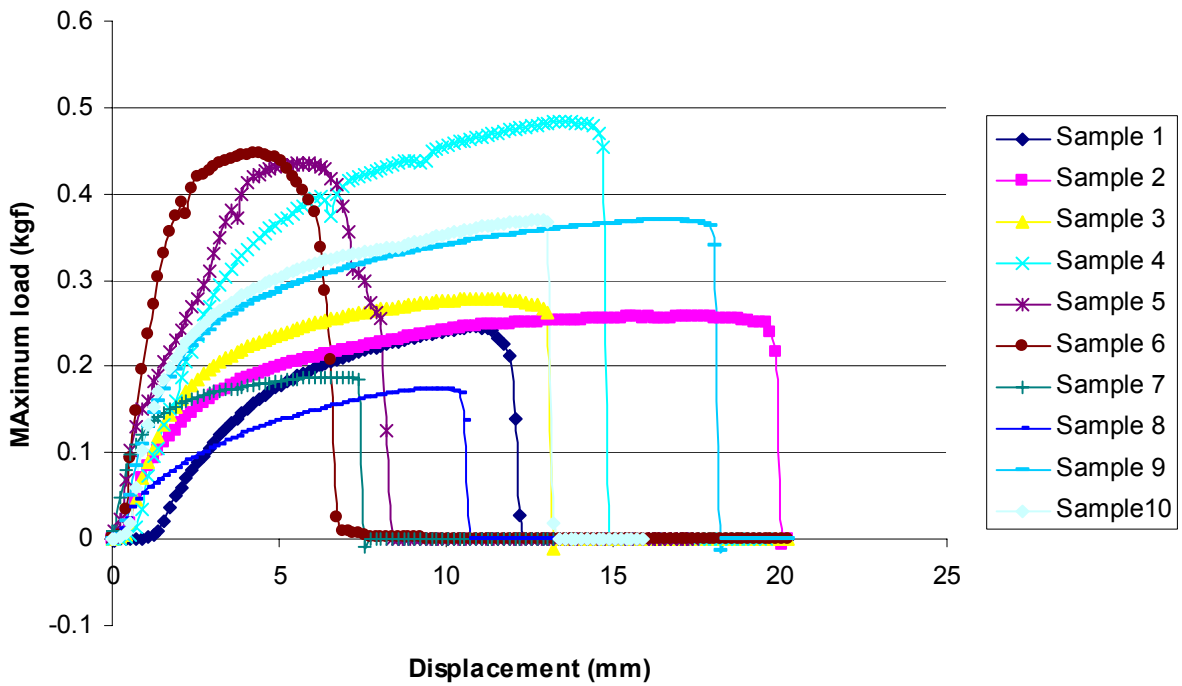


Figure 6.46. Comparison of load-elongation curves for nano-micro fiber based yarns

Even though the samples were prepared from the same solution, the maximum load showed some difference for 10 different samples. This shows that the weight and the fiber distribution were not uniform.

6.5. Air Permeability

Electrospun webs have less pores and high surface tension compared to the other nonwoven structures. Air permeability test was done to evaluate and compare different fabrics for breathability.

For 12 wt. % PVA based electrospun web, 4 different samples were tested to get an average air permeability value. The air permeability values for all the samples were consistent (Table 6.3).

Table 6.3. Air permeability of the samples

Sample	Fabric properties	Average Penetration time (sec)	Air Permeability (m ³ /min/m ²)	Average Thickness (mm)
1	Nanofiber web (sample 1)	46.4 (maximum thickness)	9.86*10 ⁻¹⁰	1.34
2	Nanofiber web (sample 2)	6.733	6.79*10 ⁻⁹	0.037
3	Nanofiber web (sample 3)	7.65	5.98*10 ⁻⁹	0.034286
4	Nanofiber web (sample 4)	6.27	7.29*10 ⁻⁹	0.0308

6.6. Surface Tension

Surface tension is important to avoid beading problem. The voltage effect also depends on surface tension. Surface tension depends on the polymerization of the solution. When the polymerization is low, the surface tension is also expected to be low.

When Laponite® clay is added into the PVA solution, surface tension increases from 63.07 mN/m to 69 mN/m as shown in Table 6.4. This increase is mostly the result of high surface area of the Laponite® particles. This is also proved by Zhang by comparing different polyvinyl alcohol concentrations [3].

Table 6.4. Surface tension of the solutions.

Material	Surface Tension (mN/m)						
Samples	1st measurement	2nd	3rd	4th	5th	6th	Average
PVA (12%)	67.47	52.48	63.85	67.10	64.97	62.60	~ 63.07
PVA + Laponite® (12%+5%)	70.72	64.91	72.25	71.17	68.20	--	~69.45

6.7. Differential Scanning Calorimetry (DSC)

DSC is a method to figure out the relationship between temperature and heat flow. It provides quantitative and qualitative data on endothermic and exothermic processes of materials which are the result of melting, oxidation, and other heat related changes.

In this study, pure PVA and Laponite® added solutions are investigated to understand the glass transition and melting point differences.

PVA has a glass transition and melting point that depend on if it is partially or fully hydrolyzed (Table 6.5.). It can be assumed that, the melting point changes between 180°-230° C. After adding Laponite® the melting point increased.

Table 6.5. PVA properties [4]

	Partially Hydrolyzed	Fully Hydrolyzed
Glass Transition Temperature (°C)	58	85
Melting point Temperature(°C)	180	230

The samples were prepared for measuring under modulated differential scanning calorimetry (MDSC). The weight was around 5-6 mg and encapsulated in the pan. Since a polymer is used for MDSC, the thickness is taken as small as possible to get more accurate results.

Figures 6.47-50 are the MDSC results, from which we may determine the crystalline temperatures, glass transition temperatures, melting points, etc. The effect of the Laponite® addition was shown by comparing the glass transition and melting point of different samples. The samples are 12 wt %PVA, 12 wt % PVA + 1% wt Laponite® , 12 wt % PVA + 2 wt % Laponite® and 12 wt % PVA + 3% wt Laponite®.

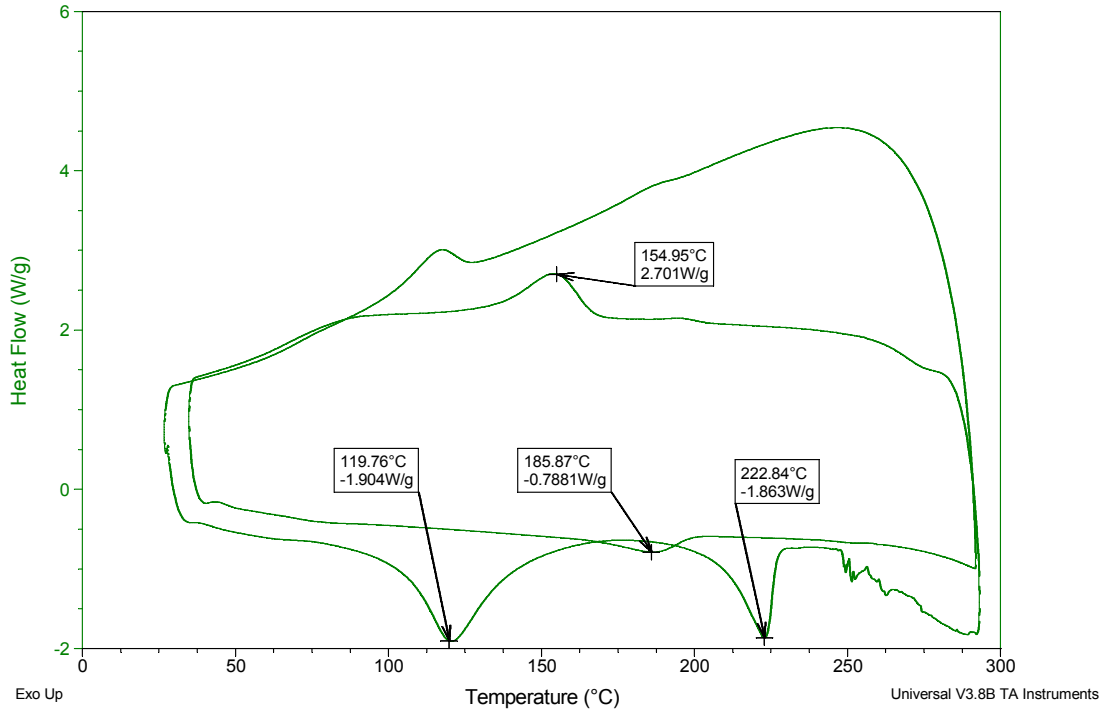


Figure 6.47. DSC results of 12 wt % PVA

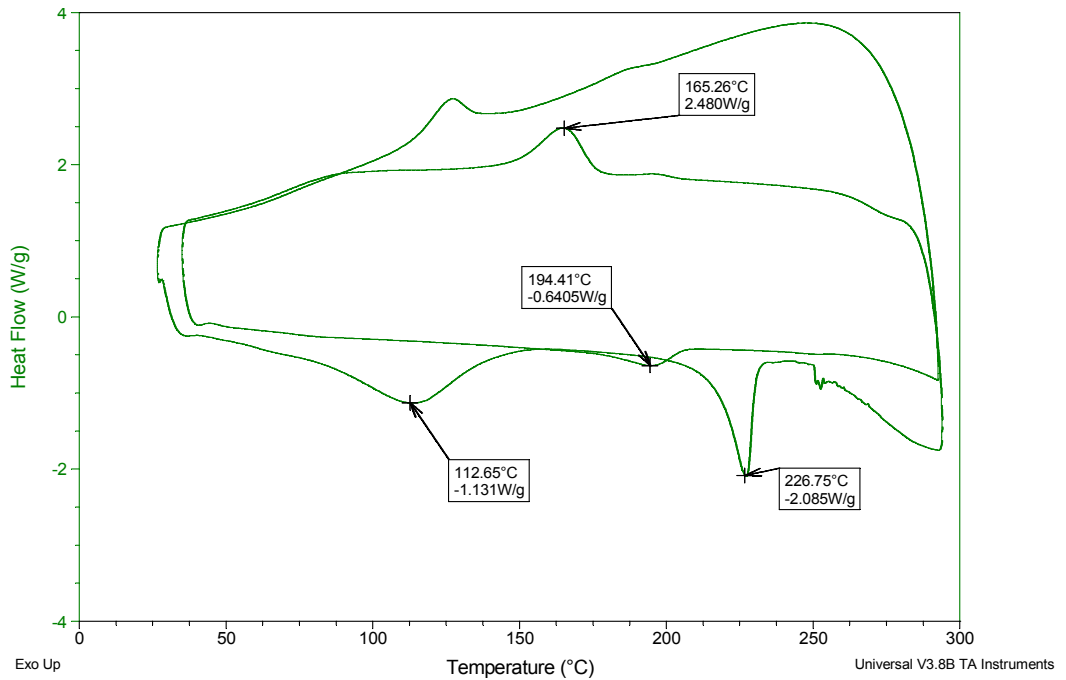


Figure 6.48. DSC results of 12 wt % PVA+ 1 wt % Laponite®

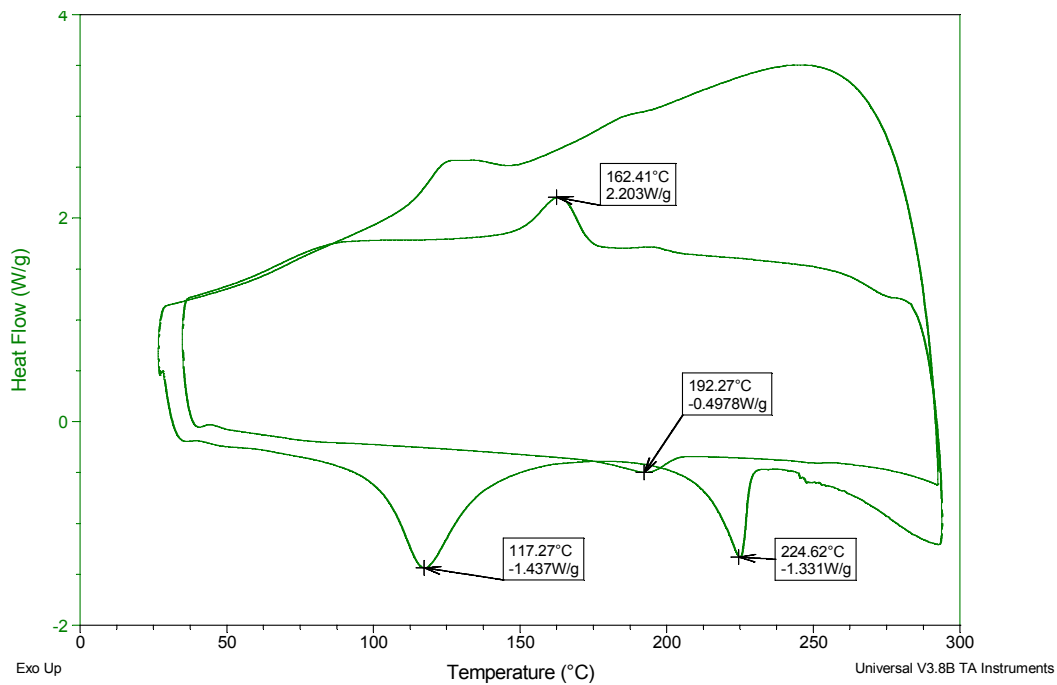


Figure 6.49. DSC results of 12 wt %PVA+ 2 wt % Laponite®

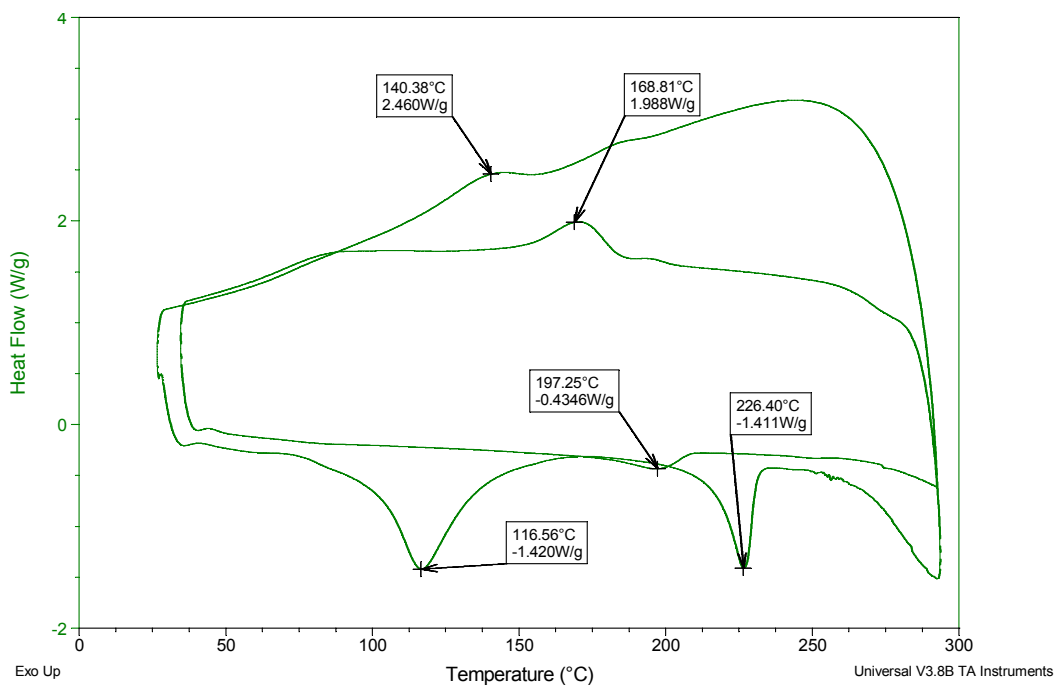


Figure 6.50. DSC results of 12 wt %PVA+ 3 wt % Laponite®

Glass Transition Temperature

The glass transition temperatures were found out different for pure PVA sample and PVA + Laponite® sample. The glass transition temperature indicates when the structure starts to have molecular mobility inside. At this time, enthalpic relaxation occurs and since this is a kinetic process, it is seen in nonreversing heat flow. As seen from the DSC results, the glass transition temperatures are always lower than the crystalline melting points. Intermolecular forces are important for the mobility of the molecules. When the PVA solution contains Laponite® inside, it becomes harder to have a molecular movement, thus the glass transition temperature increases when the solution has higher concentration of Laponite®. Amorphous structure and crystallization process can be seen in Figure 6.51.

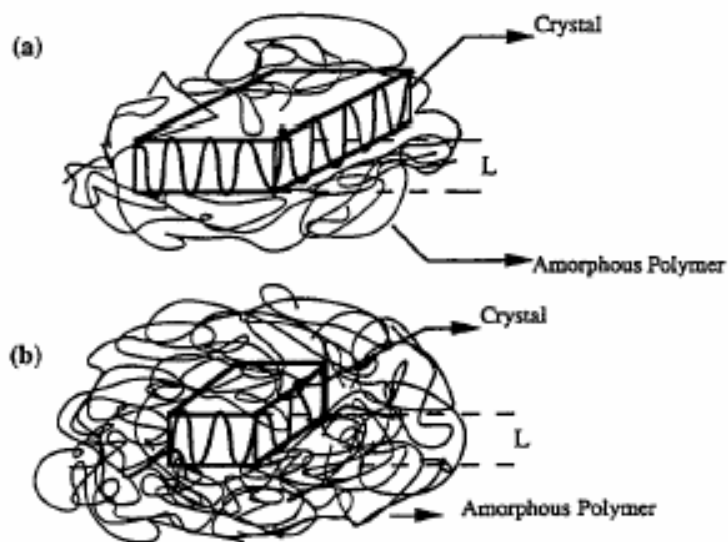


Figure 6.51. Schematic representation of unfolding of polymer chains a) Original polymer crystal, b) Crystal with a solvent [5].

Glass transition temperature was determined by averaging the first sudden heat flow peak value and the point when the flow starts to decrease. For the additional 1 wt % Laponite® into the solution, the glass transition temperature was obtained as;

$$\text{The glass transition temperature : } X = \frac{(X_1 + X_2)}{2} = \frac{92.66 + 107.74}{2} = 99.09 \text{ } ^\circ\text{C}$$

where X_1 :heat flow value when the flow starts to show a sudden decrease

X_2 : The first peak value

For the different Laponite® addition, the glass transition values are listed in Table 6.6.

Table 6.6. Comparison of glass transition temperatures

Solution	Glass Transition Temperature (°C)
Pure 12 wt %PVA	105.00
1 wt % Laponite® +12 wt % PVA	107.74
2 wt % Laponite®+12 wt %PVA	115.17
3 wt % Laponite® +12 wt %PVA	114.28

The results showed that, when the Laponite® is added in PVA solution, both the glass transition and the melting points increase. 3 wt% showed a little decrease compared to 2 wt % Laponite® addition for the glass transition temperatures; but the melting point showed an increase.

The glass transition values are given in Figures 6.52- 6.54.

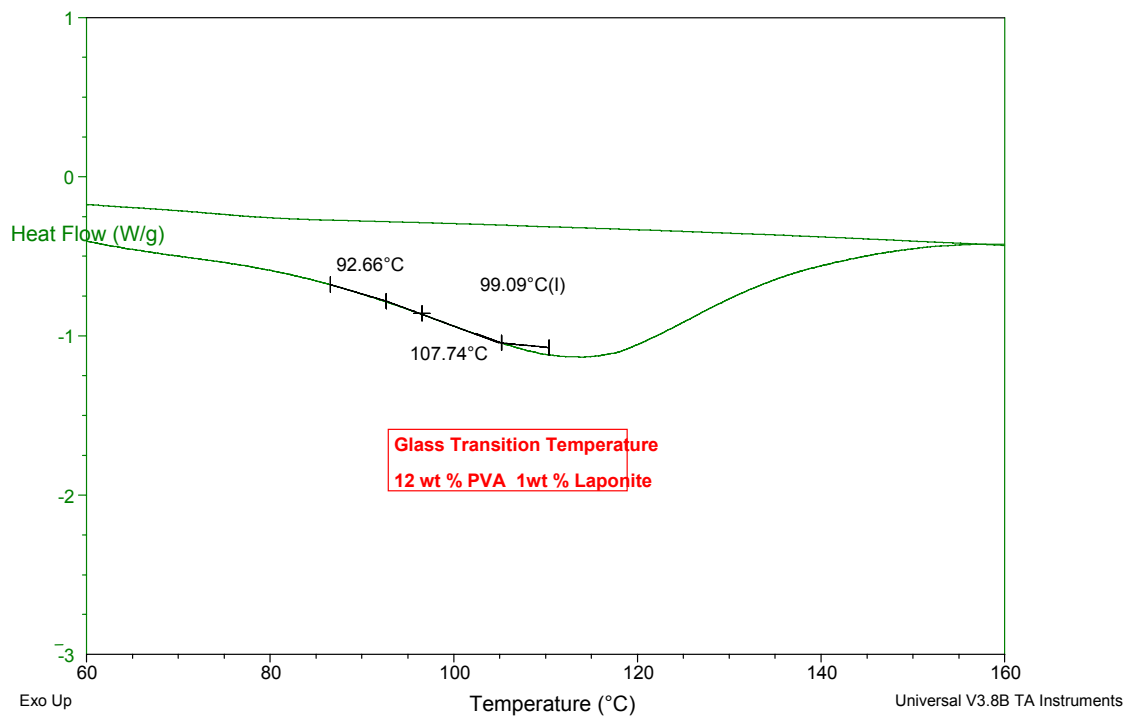


Figure 6.52. Glass transition temperature region for 12 wt % PVA + 1 wt % Laponite®.

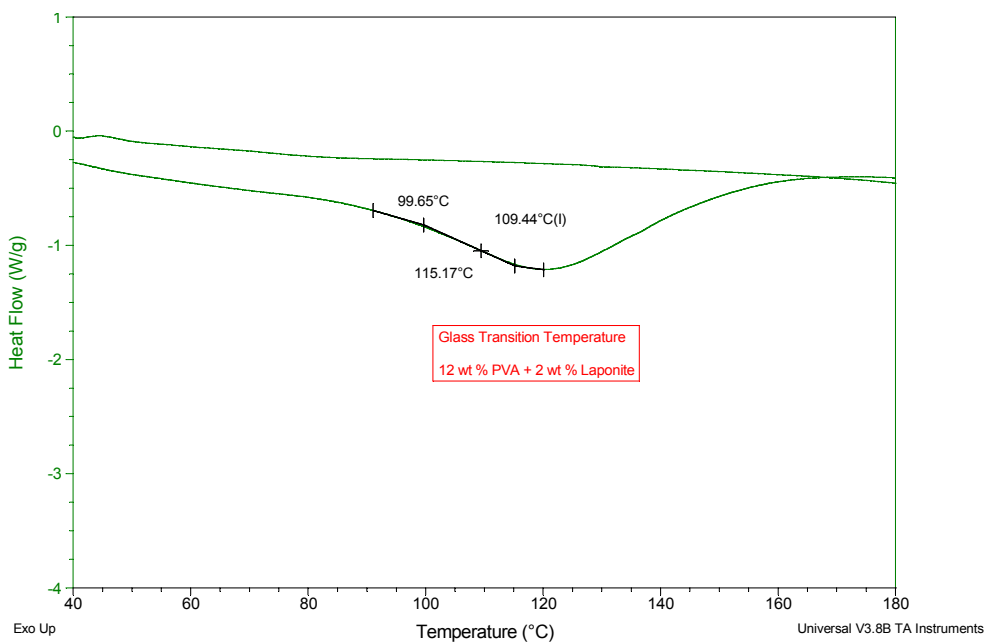


Figure 6.53. Glass transition temperature region for 12 wt % PVA and 2 wt % Laponite®.

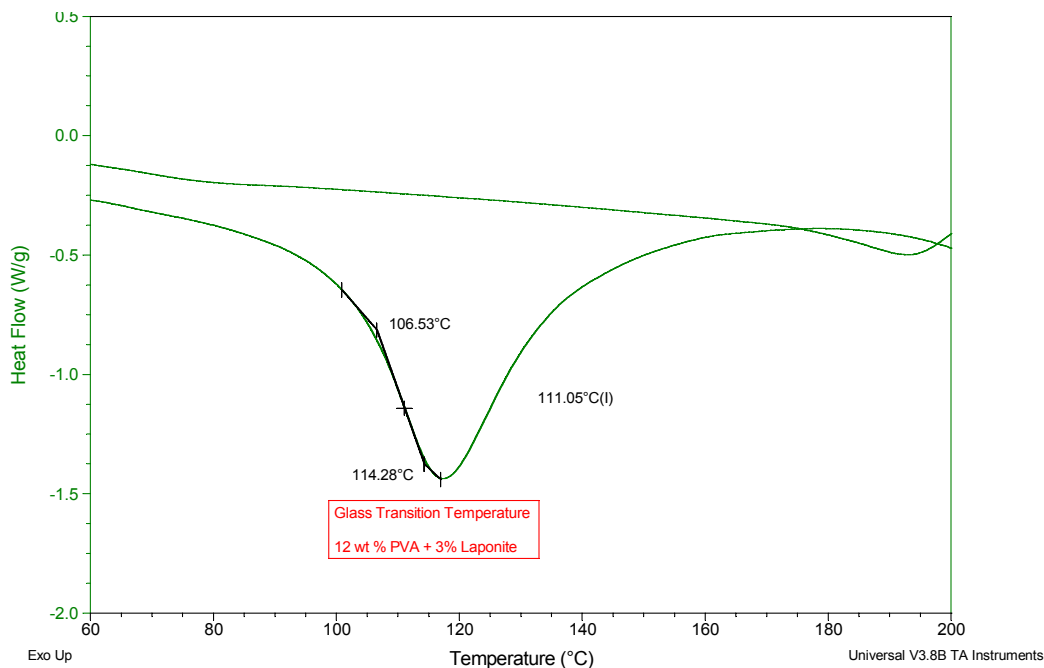


Figure 6.54. Glass transition temperature region for 12 wt % PVA and 3 wt % Laponite®.

Melting

Melting only occurs in the crystalline regions of the polymer which means there is enough energy for polymer's formation inside the crystalline regions. Normally, melting is affected by several factors: intermolecular forces, stiffness, symmetry and regularity of the polymer. It was observed that, by adding more Laponite® inside the PVA solution, the melting point showed a higher value as shown in Figure 6.55.

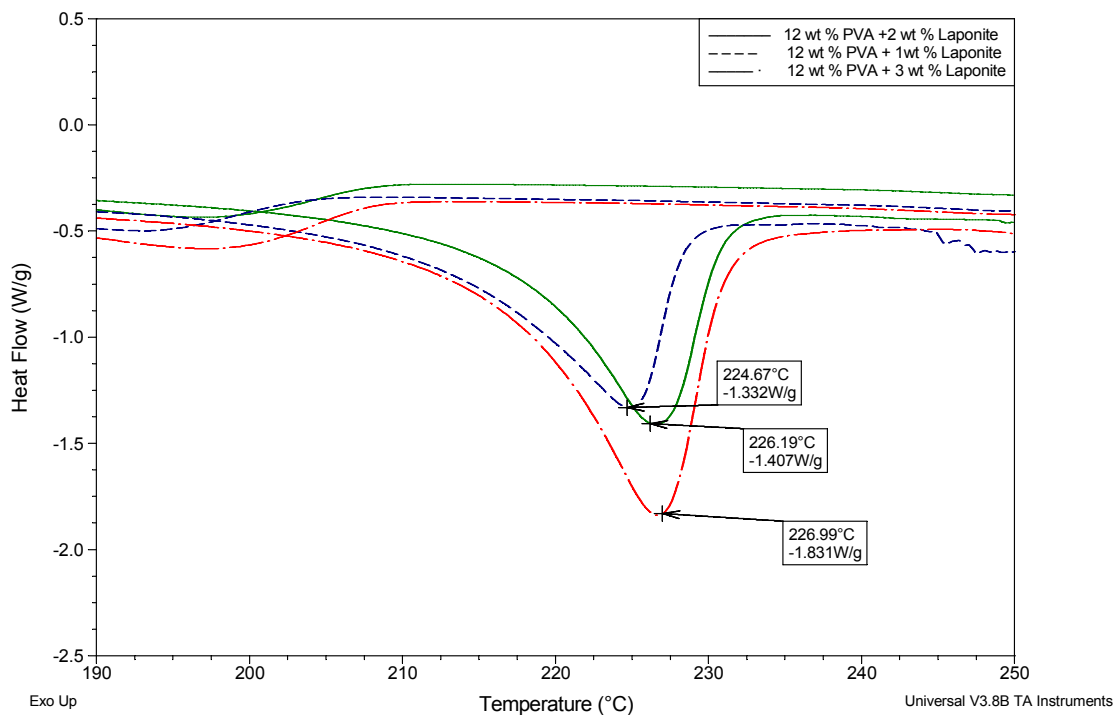


Figure 6.55. Melting point comparison among three samples: 12 wt % PVA + 1wt % Laponite®, 12 wt % PVA + 2wt % Laponite®, and 12 wt % PVA + 3wt % Laponite®

6.8. Thermogravimetric Analysis (TGA)

Thermogravimetric analysis measures the rate of weight change in a material with increasing temperature over time due to decomposition, oxidation, or dehydration.

In this study, TGA is used to understand how Laponite® affects the PVA fiber web in terms of weight loss. Figures 6.56 and 6.57 show that by adding Laponite® inside the PVA solution, the barrier properties and thermal stability were improved.

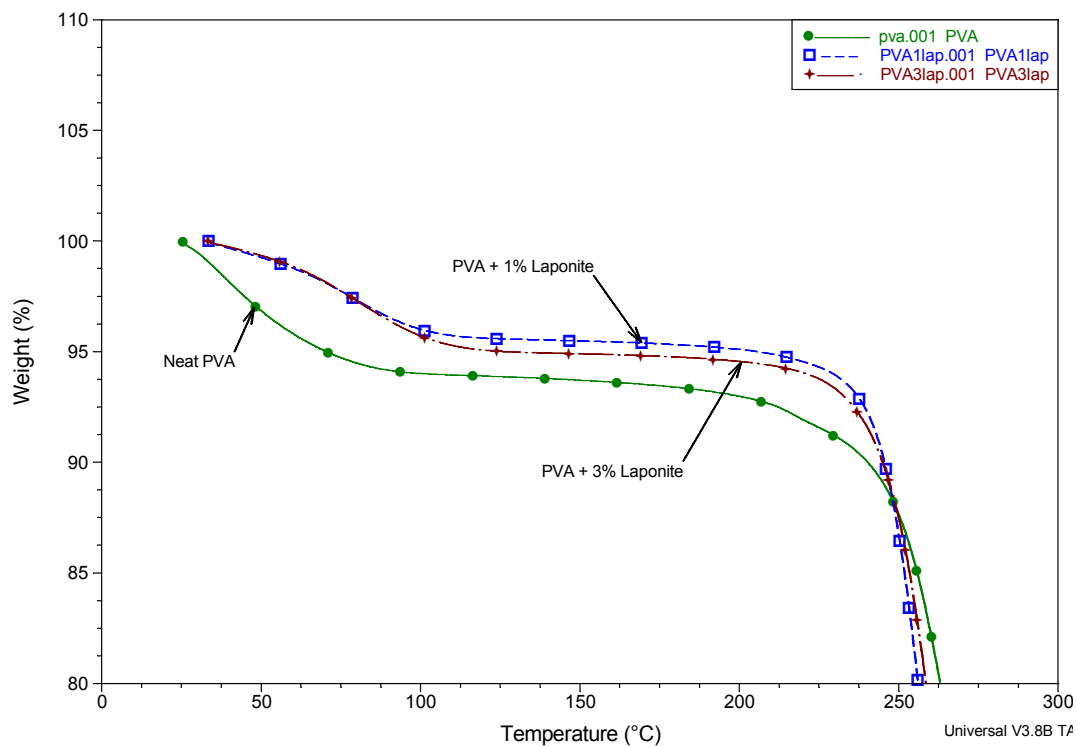


Figure 6.56. Weight loss comparison by TGA up to 300 °C among three samples: Pure 12 wt % PVA, 12 wt % PVA+ 1 wt % Laponite®, and 12 wt % PVA + 3 wt % Laponite®.

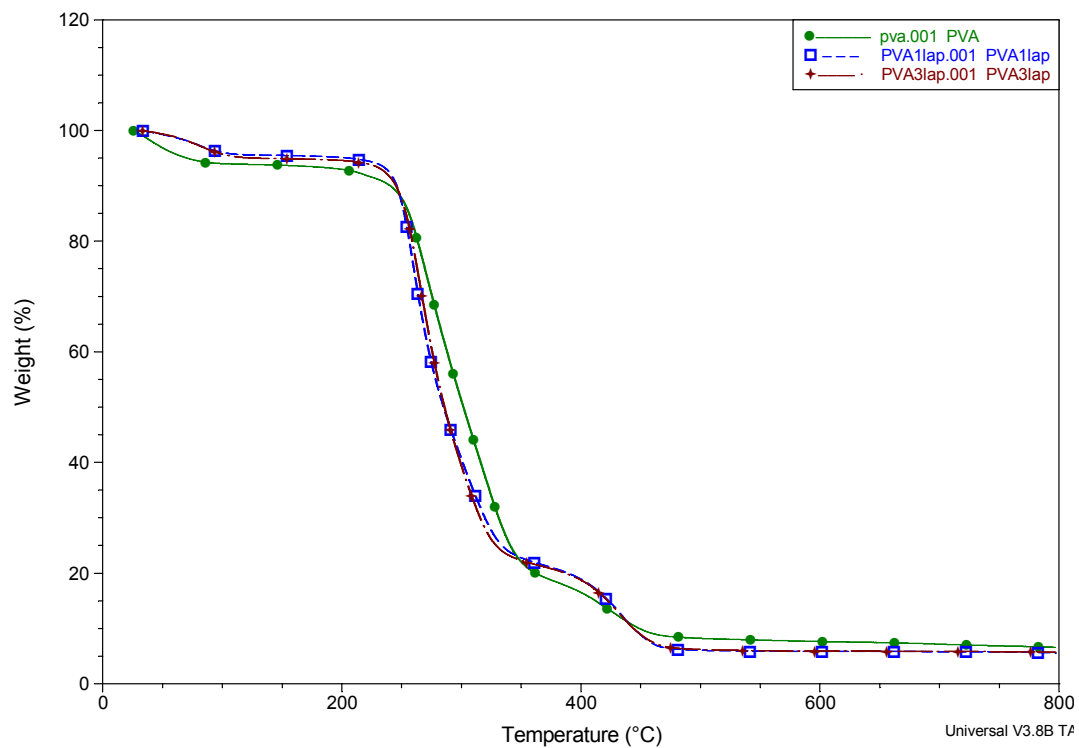


Figure 6.57. Weight loss comparison by TGA up to 800 °C among three samples: Pure 12 wt % PVA, 12 wt % PVA+ 1 wt % Laponite®, and 12 wt % PVA + 3 wt % Laponite®.

6.9. Continuous Yarn Manufacturing

Continuous yarn manufacturing is a challenge. There are many parameters that have to be taken into consideration before modeling the set-up.

There were two important parameters before designing the process: to get a linear voltage distribution and to get the fibers aligned in the electrospun web. The first concern was solved by placing the collector behind a nonwoven fabric. The second issue was solved by rotating the cylindrical collector and nonwoven fabric together. By rotating the nonwoven fabric, the pulling becomes much easier and thus continuous fiber bundle can be obtained. It is important to note that, when the nonwoven fabric is placed in a cylindrical shape pipe between the collector and the syringe, the spinning becomes inefficient. Another important factor is that the needle is placed at the back of a wooden piece which helps to contribute the linearity of the electrical forces. The picture and schematic of the collecting mechanism is shown in Figure 6.58.

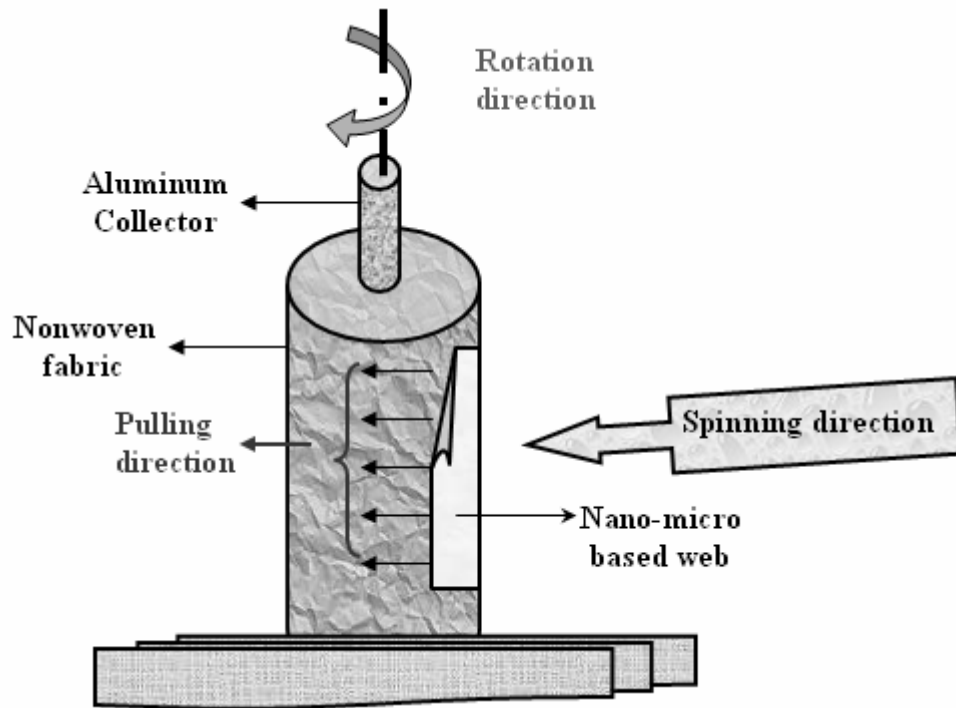
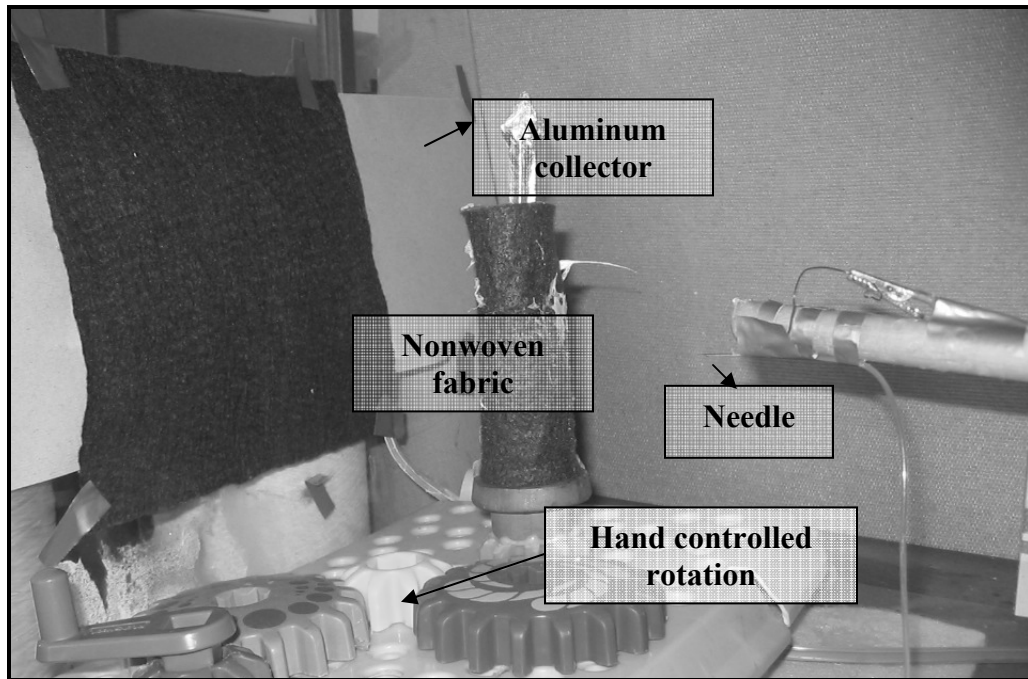


Figure 6.58. Picture and schematic of the collecting mechanism

Experimental Observations

- Circular piece of the collector is much useful for gathering the nanofibers together. It is also seen that, by the help of a magnet, the distribution of the fibers was towards the circular piece.
- When two needles were used instead of one, spinning efficiency could be increased.
- When nonwoven fabric is used as a collector, formation of film is avoided. Spinning time also has an effect on film forming.
- 12 wt % PVA gave the optimum spinning conditions with reduced beading.
- The space between the collector and needle was kept constant to have an effective spinning.
- At some point magnetic resonance was seen, which naturally created a spinning by the help of vibration and made it easy to have aligned fibers.
- When the area of the collector is increased, the spinning efficiency also increases. Therefore “aluminum pools” were manufactured to increase the collector’s area.

After creating these pools, we used them as a collector (Figure 6.59).

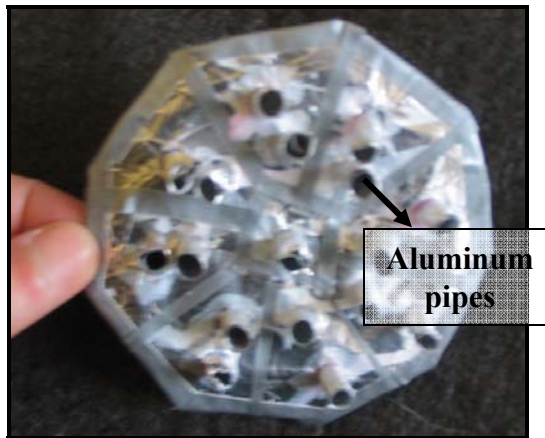
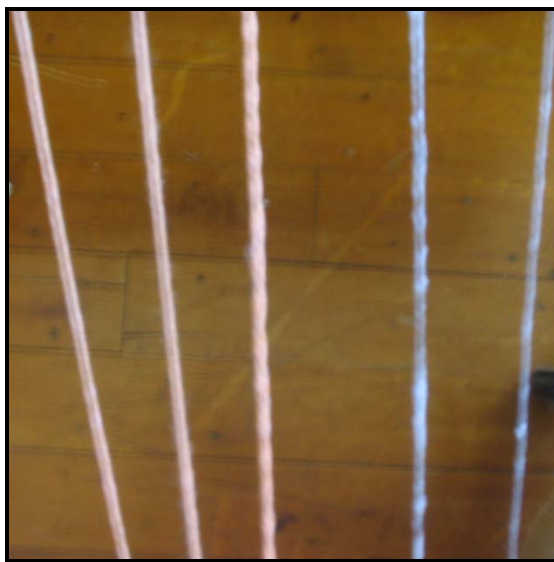


Figure 6.59. Aluminum pool.

- Yarn coating is done by using different yarns. It was seen that wetting the yarn before coating improves the coating. Figure 6.60 shows the yarns that are coated by electrospun PVA fibers. When the radius is decreased, the coating becomes much harder.



(a)



(b)

Figure 6.60. Coated yarns

6.10. References

1. Islam, Md. R., Pramila, A., “*Thermal Conductivities of Fiber Reinforced Composites by the FEM*”, Journal of Composites, **1998**, 33(18), 1699-1715.
2. Fong, H., and Reneker, D. H., “*Beaded Nanofibers Formed During Electrospinning*”, Polymer, **1990**, 40, 4585-4558.
3. Zhang, C., “*Study of Morphology of Electrospun Poly (vinyl alcohol) Mats*”, European Polymer Journal, **2005**, 41, 423-432.
4. <http://www.erkol.com/eng/Characteristics.htm> (accessed in Jan 2005).
5. Mallapragada S.,and Peppas, N. A., “*Dissolution Mechanism of Semicrystalline Poly(vinyl alcohol) in Water*”, Journal of Polymer Science: Part B: Polymer Physics, **1996**, 34, 1339-1346.

CHAPTER 7

CONCLUSIONS AND RECOMMENDATIONS

The following conclusions can be drawn from this research.

- The thermal behavior of nano-micro sized fiber composites has been analyzed and compared experimentally, analytically, and numerically. It was found that the analytical modeling in which the hexagonal unit cell is used showed much accurate results compared to the rectangle unit cell when the thermal conductivity of the filler fiber had higher value compared to the main fiber. By using the hexagonal cell, the model was restricted for the filler fibers' volume fraction which is changed between 10 and 30%.
- In numerical modeling, ANSYS 7.0 software was used to find the effective thermal conductivity of the nano-micro fiber composites by using the hexagonal unit cell. It was found that when the barrier thickness becomes larger, the effective thermal conductivity value increases.
- To manufacture a continuous nano and micro sized fibrous yarn, a system was designed and the optimum properties of the device were discussed. Two problems were solved by using this device; the first is the linear electrical force distribution

and the second is the aligning problem which is solved by rotating the nonwoven fabric covered cylinder.

- Electrospinning method was used to collect the fibers in the web form. Different kind of fabric surfaces were used to collect the fibers. The non-woven fabrics were found to be the best fabric to get the fibers in the web form.
- Electrospinning was monitored to discuss the voltage effect over polymer solution. It was found that, when the voltage is increased from 15 kV to 20 kV, the spinning starts earlier and the total electrical force increases.
- Scanning Electron Microscope was used to find the fiber size and alignment of the nano-micro web form. Beading effect, the optimum solution viscosity, optimum voltage effect were discussed. It was founded that, when the 10 wt. %PVA solution is used, the average fiber radius becomes around 450 nm and when the viscosity is increased to 15 wt %, the radius of the fibers increases to 500 nm.
- Air permeability and surface tension of the web form was measured and calculated to discuss the stability of the web form. It is found that by using the nano-micro fiber web form, very low air permeability can be obtained.
- Maximum elongation measurements were done to find out the continuity of the yarn which was formed by twisting the nano-micro fiber based web form. It was found that, the continuity was satisfied.
- Differential Scanning Microscope was used to discuss the heat behavior of the PVA and PVA+Laponite® solutions. The heat flow was found for different ratio of solutions and compared each other. The glass transition temperatures were

increased by adding the additional Laponite® inside the PVA solution. Compared to the melting temperature value, glass transition values showed more increase.

- Thermal Gravimetric Analysis was done to discuss the mass loss for the solutions. It was found that when the Laponite® was added into the PVA solutions, time for total mass loss increased.

The following is recommended for any future work on this subject:

- Automatic continuous manufacturing system need to be designed. Especially pulling mechanism needs to be designed with higher sensitivity.
- Although thermal measuring was done to get the mass loss and heat flow, thermal conductivity measurements need to be done experimentally.
- To compare the nano and micro effects in composites, apart from the micro sized modeling of composites, there is a need for nano scale modeling. This could be done by using either molecular or atomistic modeling methods.
- Different kinds of materials need to be used for verifying the correctness of both analytical and numerical models.
- Although transverse thermal conductivity has more importance and effect on defining the behavior of composite materials, longitudinal thermal conductivity needs to be discussed.
- Flame resistance behavior of the composites needs to be discussed and modeled experimentally, numerically and analytically.

APPENDIX

% FORTRAN PROGRAM for the Hexagonal Unit Cell

format long e

clear all

clc

% _____

% INPUT VALUES

% % _____

%Input Volume fraction of Fiber;

Radius of the disk; rd

rd=input('Radius of the disk; rd_');

Radius of the barrier; a

a=input('Radius of the barrier; a_');

% _____

% Length of the hexagonal side; L

% L=input('Length of the hexagonal side; L_');

L=30;

% Thickness

t=(a-rd);

% Dimensionless Thickness

tt=t/rd;

% Angles;

%Between barrier and fiber; Phi

%Phi=input('Between barrier and fiber; Phi_');

XXX= asin(rd/a);

```

% Thermal conductivities
%   % of the disk
%   kd=input(' ke of the disk_');
    kd=20000;
%   % of the barrier
%   kb=input('ke of the barrier_');
    kb=10000;
%   % of the fiber
%   kf=input('ke of the fiber_');
    kf=10;
    % Then calculate the areas and volume fractions;
% Area of ...
    % the disk; Ad
    Ad= pi*rd^2;

    % the barrier;Ab
    Ab=pi*(a^2-rd^2);

    % the fiber;Af
    Af=3*(sqrt(3)/2)*L^2;

% Volume fraction;
    % Disk volume fraction; Vd
    Vd= Ad/Af
    % Barrier volume fraction;Vb
    Vb= Ab/Af

% Dimensionless forms;
    % Dimensionless thermal conductivity

```

```

Alfa1= kb/kf;
% Beta=kd/kf; % It is given in the loop.

bb=sqrt(3)*L/(2*a);

% _____

Beta=0.01:0.01:100;
JJ=Beta;
% Alfa1=input('Alfa...');
Alfa=Alfa1.*ones(1,10000);
d=1./Beta-1./Alfa;
c=1./Alfa-1;
b=bb.*ones(1,10000);
t=tt.*ones(1,10000);
XX=XXX.*ones(1,10000);
% _____
% REGIONS
%The 1st region
% _____
S1=sqrt(3)/2-1./b+(1./c).*(pi/2-XX);
%The 2nd region
% _____
if b.^2>c.^2;
    P=sqrt(b.^2-c.^2);
% PP=atan(sqrt((b-c)/(b+c))-atan(sqrt((b-c)/(b+c)).*tan(XX/2)));
PP=atan(P./(b+c))-atan((P./(b+c)).*tan(XX/2));
S2=-((b)/(c.*P)).*PP;
display('_____')

```

```

elseif b.^2<c.^2
    Y=sqrt(c.^2-b.^2);
    YY=log2((c+Y).*(b+c.*cos(XX))./(b.*(b+c.*cos(XX)+Y.*sin(XX))));
    S2=-(b./(c.*Y)).*YY;
    display ('_____')
else
    display ('Equality..!')
end
% For 3rd region:
% Composite Simpson Method;
% _____

S30=1./(b+c+sqrt(1./(t+1).^2).*d);

S31=cos(XX/6)./(b+c.*cos(XX/6)+sqrt(1./(t+1).^2-sin(XX/6).^2).*d);
S32=cos(XX/3)./(b+c.*cos(XX/3)+sqrt(1./(t+1).^2-sin(XX/3).^2).*d);
S33=cos(XX/2)./(b+c.*cos(XX/2)+sqrt(1./(t+1).^2-sin(XX/2).^2).*d);
S34=cos(2*XX/3)./(b+c.*cos(2*XX/3)+sqrt(1./(t+1).^2-sin(2*XX/3).^2).*d);
S35=cos(5*XX/6)./(b+c.*cos(5*XX/6)+sqrt(1./(t+1).^2-sin(5*XX/6).^2).*d);
S36=cos(XX)./(b+c.*cos(XX)+sqrt(1./(t+1).^2-sin(XX).^2).*d);

S3=(XX/18).*(S30+4*S31+2*S32+4*S33+2*S34+4*S35+S36);

SS=(3*sqrt(3)/2)*(S1+S2+S3);

xlabel('\bfBeta')
ylabel('\bf Partial Effective Thermal Conductivity')
title('\bfFor integral form...')
axis ([0.01 100 0 0.001])
semilogx(JJ,SS)

```